Element 115

Forsberg, Ulrika

2016

Document Version:
Publisher's PDF, also known as Version of record

Element 115

Ulrika Forsberg

LUND
UNIVERSITY

Division of Nuclear Physics
Faculty of Science

Lund University 2016

ISBN-978-91-7623-812-7 (print)
ISBN-978-91-7623-813-4 (pdf)
LUNFD6 / (NFFR - 1037) / 1 - 143 (2016)
Printed in 2016 by Media-Tryck, Lunds universitet, Lund, Sweden.

Element 115

Ulrika Forsberg

Division of Nuclear Physics
Faculty of Science
Lund University, Sweden

Dissertation for the degree of
Doctor of Philosophy

Thesis Advisor:
Prof. Dirk Rudolph

Faculty Opponent:
Dr. Araceli Lopez-Martens

Academic dissertation which, by due permission of the Faculty of Science at Lund University, will be publicly defended on Friday, May 20th, 2016, at 13.15 in Rydbergssalen, Sölvegatan 14A, Lund, for the degree of Doctor of Philosophy.

Organization	Document name
LUND UNIVERSITY Department of Physics Division of Nuclear Physics Box 118, SE-22100 LUND, SWEDEN	DOCTORAL DISSERTATION
	Date of issue 2016-04-26
Author(s) Ulrika Forsberg	Sponsoring organization

Title and subtitle
Element 115

Abstract

This thesis is devoted to detailed studies of element 115 decay chains using the highly efficient multi-coincidence alpha, electron, gamma and X-ray detector setup TASISpec at the gas-filled separator TASCA at GSI, Darmstadt, Germany. In a three-week long experiment thirty new decay chains assumed to stem from element 115 isotopes were observed together with the very first detections of gamma rays and potential X-rays from these nuclei.

Paper I describes preparations in terms of optimisations of the magnetic fields in TASCA. Paper II presents data from 23 of the observed chains and the very first level schemes along element 115 decay chains, and discusses the first observation of potential X-rays. In Paper III aspects of the data analysis are described. Paper IV considers correlations along element 115 decay chains and a generalisation of a previously devised test for congruence of data sets. Paper V presents the remaining seven chains from our experiment and discusses possible isotopic origins of those chains as well as similar chains observed at the Joint Institute for Nuclear Reactions, Dubna, Russia and Lawrence Berkeley National Laboratory, Berkeley, USA. Paper VI is a popular science article about new chemical elements.

Key words
Superheavy elements, element 115, spectroscopy, alpha decay, X rays, gamma rays, spontaneous fission, nuclear structure

Classification system and/or index terms (if any)

Supplementary bibliographical information	Language English
ISSN and key title	ISBN 978-91-7623-812-7
Recipient´s notes	Number of pages 171 / Price
	Security classification

Distribution by Ulrika Forsberg, Division of Nuclear Physics, Lund University, Box 118, SE-22100 LUND

Summary of papers

Paper I

First Experiment at TASCA Towards X-ray Fingerprinting of Element 115 Decay Chains

U. Forsberg, P. Golubev, L.G. Sarmiento, J. Jeppsson, D. Rudolph, L.-L. Andersson, D. Ackermann, M. Asai, M. Block, Ch.E. Düllmann, J. Dvorak, K. Eberhardt, J. Even, J.M. Gates, K.E. Gregorich, R.-D. Herzberg, F.P. Hessberger, E. Jäger, J. Khuyagbaatar, I. Kojouharov, J.V. Kratz, J. Krier, N. Kurz, S. Lahiri, B. Lommel, M. Maiti, E. Merchán, J.P. Omtvedt, E. Parr, J. Runke, H. Schaffner, M. Schädel, and A. Yakushev

Acta Phys. Pol. B **43**, 305 (2012)

In this paper we describe how we investigated the transmission of fusion-evaporation products through TASCA to the implantation detector of TASISpec. TASISpec was initially designed to be coupled to TASCA in Small Image Mode (SIM). However, the excellent background suppression achieved in High Transmission Mode (HTM) proposed by J.M. Gates made this mode interesting also for TASISpec experiments. As a first step in investigating this possibility, simulations of the transmission through TASCA and the focal-plane image were performed. Using the results from these simulations a test-experiment was planned. We used the

reaction ^{48}Ca + ^{208}Pb to produce atoms of nobelium (No, Z = 102) with a relatively high cross section, and studied how varying magnet settings in TASCA affected the transmission and background conditions. We found that the magnet setting can be optimised such that is beneficial to use HTM also in the case of TASISpec measurements.

My contribution to the paper was to perform simulations of TASCA transmission using existing codes, calculate beam energies and magnetic rigidities for Nobelium, participate in preparing and planning the part of the experiment that aimed at determining the transmission properties, analyse the data during the experiment in order to decide on how to proceed, to analyse the data after the experiment, and to write and communicate the manuscript.

Paper II

Spectroscopy of Element 115 Decay Chains
D. Rudolph, **U. Forsberg**, P. Golubev, L.G. Sarmiento, A. Yakushev, L.-L. Andersson, A. Di Nitto, Ch.E. Düllmann, J.M. Gates, K.E. Gregorich, C.J. Gross, F.P. Heßberger, R.-D. Herzberg, J. Khuyagbaatar, J.V. Kratz, K. Rykaczewski, M. Schädel, S. Åberg, D. Ackermann, M. Block, H. Brand, B.G. Carlsson, D. Cox, X. Derkx, K. Eberhardt, J. Even, C. Fahlander, J. Gerl, E. Jäger, B. Kindler, J. Krier, I. Kojouharov, N. Kurz, B. Lommel, A. Mistry, C. Mokry, H. Nitsche, J.P. Omtvedt, P. Papadakis, I. Ragnarsson, J. Runke, H. Schaffner, B. Schausten, P. Thörle-Pospiech, T. Torres, T. Traut, N. Trautmann, A. Türler, A. Ward, D.E. Ward, and N. Wiehl
Phys. Rev. Lett. **111**, 112502 (2013)
Highlighted article, Editor's choice & Synopsis at
physics.aps.org/synopsis-for/10.1103/PhysRevLett.111.112502
Among APS Top Ten Physics Newsmakers 2013!

In this paper we communicate the first results from our element 115 decay chain experiment performed at TASCA at GSI. We present the key aspects of the experiment and reveal that our three-week experiment lead to the observation of 30 correlated α-decay chains. Of those, there were 23 chains "long" chains that were in agreement with previously published chains from the Dubna gas-filled separator assigned to the isotopes $^{288}115$ and $^{287}115$. The measured energies and times from these chains are reported. We also report on the first ever measurements of nuclear structure for elements with more than about 110 protons, and present potential X-ray candidates seen in conjunction with α decay from the isotope ^{276}Mt, which is part of the decay chain starting from $^{288}115$.

My contribution to this paper was to participate in preparations (upgrade TASISpec, calculate beam energies, TASCA settings, setting up parts of the electronics etc.) and performance (preliminary data analysis etc.) of the experiment, to convert recorded pulse shapes to energies and times, to reconstruct the α energies that were split between different detectors, and assisted in preparing the manuscript.

Paper III

Spectroscopic Tools Applied to Element Z = 115 Decay Chains

U. Forsberg, D. Rudolph, P. Golubev, L.G. Sarmiento, A. Yakushev, L.-L. Andersson, A. Di Nitto, Ch.E. Düllmann, J.M. Gates, K.E. Gregorich, C.J. Gross, F.P. Heßberger, R.-D. Herzberg, J. Khuyagbaatar, J.V. Kratz, K. Rykaczewski, M. Schädel, S. Åberg, D. Ackermann, M. Block, H. Brand, B.G. Carlsson, D. Cox, X. Derkx, K. Eberhardt, J. Even, C. Fahlander, J. Gerl, E. Jäger, B. Kindler, J. Krier, I. Kojouharov, N. Kurz, B. Lommel, A. Mistry, C. Mokry, H. Nitsche, J.P. Omtvedt, P. Papadakis, I. Ragnarsson, J. Runke, H. Schaffner, B. Schausten, P. Thörle-Pospiech, T. Torres, T. Traut, N. Trautmann, A. Türler, A. Ward, D.E. Ward, and N. Wiehl

EPJ Web of Conferences **66**, 02036 (2014)

In this paper some aspects of data analysis that lay the foundation for Paper II are discussed in some more detail: pulse-shape analysis, dead-layer determination for the TASISpec silicon detectors, and the method to reconstruct energy depositions that were split between two detectors.

My contribution to the paper was to participate in preparing and performing the experiment, to perform the customisation of the pulse-shape analysis, to determine the dead-layer thickness for each pixel, to implement an energy reconstruction routine, and to write and communicate the manuscript.

Paper IV

Superheavy-element Spectroscopy: Correlations Along Element 115 Decay Chains

D. Rudolph, **U. Forsberg**, L.G. Sarmiento, P. Golubev, and C. Fahlander

EPJ Web of Conferences, in press

In this paper, correlations in the complicated data on element 115 decay chains are investigated. We present correlations between times and energies along all published element 115 decay chains from TASCA, Dubna gas-filled separator, and Berkeley gas-filled separator. Differences and similarities between chains assigned to different isotopes are thereby highlighted. We also use a new statistical method to evaluate the congruence in sets of decay chains, finding that the previous grouping of chains is with a very large probability incorrect.

My contribution to this paper was to come up with the idea to generalise a test proposed by K.H. Schmidt to chains of decays rather than single decay steps, and to write parts of the manuscript.

Paper V

Recoil-α-α-fission and Recoil-α-fission Events Observed in the Reaction ^{48}Ca + ^{243}Am

U. Forsberg, D. Rudolph, L.-L. Andersson, A. Di Nitto, Ch.E. Düllmann, J.M. Gates, P. Golubev, K.E. Gregorich, C.J. Gross, R.-D. Herzberg, F.P. Heßberger, J. Khuyagbaatar, J.V. Kratz, K. Rykaczewski, L.G. Sarmiento, M. Schädel, A. Yakushev, S. Åberg, D. Ackermann, M. Block, H. Brand, B.G. Carlsson, D. Cox, X. Derkx, J. Dobaczewski, K. Eberhardt, J. Even, C. Fahlander, J. Gerl, E. Jäger, B. Kindler, J. Krier, I. Kojouharov, N. Kurz, B. Lommel, A. Mistry, C. Mokry, W. Nazarewicz, H. Nitsche, J.P. Omtvedt, P. Papadakis, I. Ragnarsson, J. Runke, H. Schaffner, B. Schausten, Yue Shi, P. Thörle-Pospiech, T. Torres, T. Traut, N. Trautmann, A. Türler, A. Ward, D.E. Ward, and N. Wiehl

Nuclear Physics A, in press

In this paper we present data on seven "short" α-decay chains observed in our experiment on element 115. We conduct an analysis on the world data set of this type of element 115 chains (seven from our experiment, four from experiments at Dubna gas-filled separator, and three from Berkeley gas-filled separator) and find that it is statistically highly unlikely that they originate from one and the same isotope. Instead, we suggest that some of them originate from the isotope $^{288}115$ and some from the isotope $^{289}115$. The statistical test proposed in the article has, to the knowledge of the authors, not been used before.

My main contribution to this paper was to calculate the probabilities for random coincidences, to develop the stringent statistical test, to write parts of the manuscript, and to take the main responsibility for communicating the manuscript.

Paper VI

Four new synthetic elements approved

Ulrika Forsberg, Claes Fahlander, Dirk Rudolph, and Lars Öhrström
Kemivärlden Biotech med Kemisk Tidskrift. No 1 February 2016. Translated to English by Gittan Cedervall.

This popular science article was written on the initiative of Prof. Lars Öhrström and in conjunction with the announcement by International Union for Pure and Applied Chemistry (IUPAC) that the four new elements with $Z = 113$, 115, 117, and 118 had been approved around New Year's Eve 2015. It gives a short overview over the research field, focusing on identification methods for new elements, chemical investigations, and historical context.

My contribution to this article was to write parts of the manuscript and to participate in improving the readability of the text for the general public.

Related articles

Nuclear Structure Notes on Element 115 Decay Chains
D. Rudolph, L.G. Sarmiento, and **U. Forsberg**
AIP Conf. Proc. **1681**, 030015 (2015)

Decay spectroscopy of element 115 daughters: $^{280}Rg \rightarrow {}^{276}Mt$ *and* $^{276}Mt \rightarrow {}^{272}Bh$
J.M. Gates, K.E. Gregorich, O.R. Gothe, E.C. Uribe, G.K. Pang, D.L. Bleuel, M. Block, R.M. Clark, C.M. Campbell, H.L. Crawford, M. Cromaz, A. Di Nitto, Ch. E. Düllmann, N.E. Esker, C. Fahlander, P. Fallon, R.M. Farjadi, **U. Forsberg**, J. Khuyagbaatar, W. Loveland, A.O. Macchiavelli, E.M. May, P.R. Mudder, D.T. Olive, A.C. Rice, J. Rissanen, D. Rudolph, L.G. Sarmiento, J.A. Shusterman, M.A. Stoyer, A. Wiens, A. Yakushev, and H. Nitsche
Phys. Rev. C **92**, 021301(R) (2015)

GEANT*4 Spectroscopy of Heavy and Superheavy Atomic Nuclei: Element 115*
L.G. Sarmiento, D. Rudolph, **U. Forsberg**, P. Golubev, L.-L. Andersson
Proceedings of Science, PoS(X LASNPA)057 (2014)

Alpha-Photon Coincidence Spectroscopy Along Element 115 Decay Chains
D. Rudolph, **U. Forsberg**, P. Golubev, L.G. Sarmiento, A. Yakushev, L.-L. Andersson, A. Di Nitto, Ch.E. Düllmann, J.M. Gates, K.E. Gregorich, C.J. Gross, F.P. Heßberger, R.-D. Herzberg, J. Khuyagbaatar, J.V. Kratz, K. Rykaczewski, M. Schädel, S. Åberg, D. Ackermann, M. Block, H. Brand, B.G. Carlsson, D. Cox, X. Derkx, K. Eberhardt, J. Even, C. Fahlander, J. Gerl, E. Jäger, B. Kindler, J. Krier, I. Kojouharov, N. Kurz, B. Lommel, A. Mistry, C. Mokry, H. Nitsche,

J.P. Omtvedt, P. Papadakis, I. Ragnarsson, J. Runke, H. Schaffner, B. Schausten, P. Thörle-Pospiech, T. Torres, T. Traut, N. Trautmann, A. Türler, A. Ward, D.E. Ward, and N. Wiehl
Acta Phys. Pol. B **45**, 263 (2014)

^{48}Ca + ^{249}Bk Fusion Reaction Leading to Element $Z = 117$: Long-lived α-Decaying ^{270}Db and Discovery of ^{266}Lr
J. Khuyagbaatar, A. Yakushev, Ch.E. Düllmann, D. Ackermann, L.-L. Andersson, M. Asai, M. Block, R.A. Boll, H. Brand, D.M. Cox, M. Dasgupta, X. Derkx, A. Di Nitto, K. Eberhardt, J. Even, M. Evers, C. Fahlander, **U. Forsberg**, J.M. Gates, N. Gharibyan, P. Golubev, K.E. Gregorich, J.H. Hamilton, W. Hartmann, R.-D. Herzberg, F.P. Heßberger, D.J. Hinde, J. Hoffmann, R. Hollinger, A. Hübner, E. Jäger, B. Kindler, J.V. Kratz, J. Krier, N. Kurz, M. Laatiaoui, S. Lahiri, R. Lang, B. Lommel, M. Maiti, K. Miernik, S. Minami, A. Mistry, C. Mokry, H. Nitsche, J.P. Omtvedt, G.K. Pang, P. Papadakis, D. Renisch, J. Roberto, D. Rudolph, J. Runke, K.P. Rykaczewski, L.G. Sarmiento, M. Schädel, B. Schausten, A. Semchenkov, D.A. Shaughnessy, P. Steinegger, J. Steiner, E.E. Tereshatov, P. Thörle-Pospiech, K. Tinschert, T. Torres De Heidenreich, N. Trautmann, A. Türler, J. Uusitalo, D.E. Ward, M. Wegrzecki, N. Wiehl, S.M. Van Cleve, and V. Yakusheva
Phys. Rev. Lett. **112**, 172501 (2014)

Superheavy Element 114 is a Volatile Metal
A. Yakushev, J.M. Gates, A. Türler, M. Schädel, Ch.E. Düllmann, D. Ackermann, L.-L. Andersson, M. Block, W. Brüchle, J. Dvorak, K. Eberhardt, H.G. Essel, J. Even, **U. Forsberg**, A. Gorshkov, R. Graeger, K.E. Gregorich, W. Hartmann, R.-D. Herzberg, F.P. Heßberger, D. Hild, A. Hübner, E. Jäger, J. Khuyagbaatar, B. Kindler, J.V. Kratz, J. Krier, N. Kurz, B. Lommel, L.J. Niewisch, H. Nitsche, J.P. Omtvedt, E. Parr, Z. Qin, D. Rudolph, J. Runke, B. Schausten, E. Schimpf, A. Semchenkov, J. Steiner, P. Thörle-Pospiech, J. Uusitalo, M. Wegrzecki, and N. Wiehl
Inorg. Chem. **53**, 1624 (2014)

Selected spectroscopic results on element 115 decay chains
D. Rudolph, **U. Forsberg**, P. Golubev, L.G. Sarmiento, A. Yakushev, L.-L. Andersson, A. Di Nitto, Ch.E. Düllmann, J.M. Gates, K.E. Gregorich, C.J. Gross, R.-D. Herzberg, F.P. Heßberger, J. Khuyagbaatar, J.V. Kratz, K. Rykaczewski, M. Schädel, S. Åberg, D. Ackermann, M. Block, H. Brand, B.G. Carlsson, D. Cox, X. Derkx, K. Eberhardt, J. Even, C. Fahlander, J. Gerl, E. Jäger, B. Kindler, J. Krier, I. Kojouharov, N. Kurz, B. Lommel, A. Mistry, C. Mokry, H. Nitsche, J.P. Omtvedt, P. Papadakis, I. Ragnarsson, J. Runke, H. Schaffner, B. Schausten, P. Thörle-Pospiech, T. Torres, T. Traut, N. Trautmann, A. Türler, A. Ward, D.E. Ward and N. Wiehl
J. Radioanal. Nucl. Chem. **203** 1185 (2014)

First Superheavy Element Experiments at the GSI Recoil Separator TASCA: The Production and Decay of Element 114 in the $^{244}Pu(^{48}Ca,3\text{-}4n)$ Reaction

J.M. Gates, Ch.E. Düllmann, M. Schädel, A. Yakushev, A. Türler, K. Eberhardt, J.V. Kratz, D. Ackermann, L.-L. Andersson, M. Block, W. Brüchle, J. Dvorak, H.G. Essel, P.A. Ellison, J. Even, **U. Forsberg**, J. Gellanki, A. Gorshkov, R. Graeger, K.E. Gregorich, W. Hartmann, R.-D. Herzberg, F.P. Heßberger, D. Hild, A. Hübner, E. Jäger, J. Khuyagbaatar, B. Kindler, J. Krier, N. Kurz, S. Lahiri, D. Liebe, B. Lommel, M. Maiti, H. Nitsche, J.P. Omtvedt, E. Parr, D. Rudolph, J. Runke, H. Schaffner, B. Schausten, E. Schimpf, A. Semchenkov, J. Steiner, P. Thörle-Pospiech, J. Uusitalo, M. Wegrzecki, and N. Wiehl

Phys. Rev. C **83**, 054618 (2011)

Conference contributions

TASCA Collaboration Meeting, Darmstadt, Germany, 22/10 2015
Contributed presentation on my developments of a statistical test for congruence of sets of decay chains.

Nordic Nuclear Physics Meeting, Saariselkä, Finland, 13-17/4 2015
Contributed presentation on element 115 recoil-α(-α)-SF chains observed at TASCA, and their potential assignment to different isotopes.

International Conference on Science and Technology for FAIR, Worms, Germany, 13-17/10 2014
Invited student presentation on element 115 decay chains studied at TASCA, and an outlook on future superheavy element experiments at GSI/FAIR.

Capture Gamma-ray Spectroscopy and Related Topics, Dresden, Germany, 25-29/8 2014
Invited presentation on spectroscopy of superheavy elements in general, and on element 115 decay chains in particular.

Swedish Nuclear Physics Meeting, Stockholm, Sweden, 5-6/11 2013
Invited student presentation on our element 115 experiment. Only one student is invited annually.

Nordic Physics Days, Lund, Sweden, 12-14/6 2013
Contributed presentation on our first results from our element 115 spectroscopy experiment.

International Nuclear Physics Conference,
Florence, Italy, 2-7/6 2013
Contributed presentation on our first results from our element 115 spectroscopy experiment. I was awarded one of two prestigious "Best Young Speaker Award".

Swedish Nuclear Physics meeting, Lund, Sweden, 9-11/11 2011
Contributed presentation on the results of our test-experiment on transmission through TASCA.

Mazurian Lakes Conference, Piaski, Poland, 11-18/9 2011
Contributed poster on our planned experiment on element 115 spectroscopy.

Popular science and other activities

Science Slam, Almedalen, Sweden, July 2014.
Arranged by Lund University. Six scientists had seven minutes each to present their research in an inspiring and engaging way, and an audience of about 200 people voted and graded the presentations. My contribution won.

NMT-dagarna, Lund University, March 2014 and 2015.
During the NMT-days, students from "gymnasium" (∼high-school) are invited to the university to listen to presentations and visit laboratories. I contributed with 45-minute sessions about superheavy elements. Each contained a short (∼20 min) lecture, followed by questions from the students.

62nd Lindau Nobel Laureate Meeting,
Lindau, Germany, 1-6/6, 2012
The conference was dedicated to physics, and 27 Nobel Laureates and 592 selected young researchers from all over the world met for discussions and exchange of ideas.

Institutet, Sveriges Radio, 5/12 2015.
Popular science radio interview about superheavy elements.
sverigesradio.se/sida/artikel.aspx?programid=4131&artikel=
6298898 (In Swedish)

Till min morfar
Arnold Meyer

Acknowledgements

Thank you

Dirk, for inspiration and motivation, for sharing this intriguing research project with me, and for trusting me.

Pavel, for careful explanations, for well-needed laughs, and for always making sure that our equipment works.

Claes, for providing a cheerful atmosphere, for invaluable support during the writing of this thesis, and for always asking the right questions.

Lise-Lotte, for the good cooperation when we prepared the big experiment.

Pico, for all kinds of discussions and for computer-related help.

Charlotta, for discussions and indispensable support.

Annelie, for always helping me out and for encouraging me.

Kristina, for your supportive leadership.

Robert, for good times in Germany as well as in Lund.

Nataša and Christian, for friendship and for shared oranges.

Jnaneswari, for giving me your valuable friendship.

Douglas, for being very sensible when I was worried and confused.

Maria, for sharing with me.

Maciek, for your thoughtfulness and for both serious and very non-serious discussions.

Julius, for caring for me.

Sandra and Nathaly, for being wonderful office mates.

Fellow members of the Nuclear Physics Division, for the great working

environment you create.
Sasha, Julia, Chris, Fritz, Antonio, Jörg, Nik, Henning, Egon, Ivan, Sven, Gillis, Ingemar, Daniel, and all other element 115 experimentalists and theorists for your efforts before, during, and after our experiments.
MAX-lab nuclear and accelerator physicists, for giving me the first insight into laboratory work.
Luke, for introducing me to science and Root.
Lotta, Susanna, Annika, Emelie, Åsa, Cecilia and Lars, for helping and promoting me in my outreach activities.
Royal Physiographical Society in Lund, for generous research and travel grants.

Tack
Malin för din värdefulla klarsyn.
Pauline för att det alltid känns som igår fastän det går alltför lång tid emellan.
Anna för allt roligt vi haft.
Desirée för att du alltid stöttar mig. Om jag av någon anledning skulle bli inbjuden till en Nobelfest och får ta med mig någon, så ska vi roa oss kungligt!
Nils för jag alltid känner mig välkommen hos dig och din familj.
Vänner i SSV för de fina upplevelser vi delat.
Per-Arne för din uppmuntran.
Britt-Marie, Reine och Tobias för allt intresse ni visat för min forskning.
Birgitta för den lugna atomfär som du magiskt skapar.
Sven för ditt lugn och din vänlighet.
Mamma och pappa för allt stöd, all hjälp och all kärlek.
Therese för att du lärt mig nästan allt jag kan.

Daniel. Det hade inte gått utan dig.

Populärvetenskaplig sammanfattning

Element 115 är arbetsnamnet för det grundämne som karaktäriseras av att atomer av ämnet har 115 protoner i sin atomkärna. Protoner är positivt laddade kärnpartiklar och är ansvariga för att atomkärnor omges av lika många negativt laddade elektroner för att bilda fullvärdiga neutrala atomer. Olika grundämnen – såsom guld, syre och tellur – kännetecknas av att atomerna har olika många protoner, och därmed också olika många elektroner. Elektronerna bestämmer ämnets kemiska egenskaper. De ämnen som finns naturligt på jorden i nämnbara mängder har mellan en och 92 protoner i sina kärnor. Men går det att göra atomer som har ännu fler protoner?

Krafterna inne i kärnan är komplicerade. Vi vet att trots att protonerna är positivt laddade och därmed stöter bort varandra, så håller "vanliga" atomkärnor ändå ihop. Det måste alltså finnas andra typer av krafter som motverkar den elektriska repulsionen. Dessa krafters natur är ännu inte helt kartlagd, men vi vet att om protoner är mycket nära varandra dras de faktiskt till varanda istället för att stöta bort varandra. Vi kallar den sammanhållande effekterna för "den starka kraften".

Atomkärnor består inte bara av protoner, utan också av neutroner. De har ingen laddning, men liksom protonerna påverkas de av den starka kraften. Den gör att de inte bara dras till varandra utan även till proton-

erna. Tillsammans bildar alltså protoner och neutroner de atomkärnor som utgör vår värld. Det finns också atomkärnor som inte är stabila utan sönderfaller och sänder ut radioaktiv strålning. Detta beror ofta på att balansen mellan protoner och neutroner inte är optimal eller att de repellerande krafterna mellan protonerna till slut vinner.

I de modeller som kärnfysikens pionjärer ställde upp för ca 80 år sedan finns det en övre gräns för hur många protoner som kan finnas i en kärna. Beroende på vilken modell som användes gick gränsen vid lite olika protontal, men som mest vid ungefär hundra protoner. Det man inte visste då var att det finns en inre struktur i kärnorna som gör att vissa speciella protontal och neutrontal blir mer stabila än andra. Förklaringen till varför just dessa antal ger ökad stabilitet uppdagades i slutet av 40-talet av bland andra Maria Goeppert-Mayer, som belönades med Nobelpriset i fysik år 1963.

Under 40-talet framställdes flera nya grundämnen artificiellt i laboratorium genom att lättare atomer fusionerades – alltså slogs samman med hjälp av acceleratorer – och forskarna närmade sig den förutsagda gränsen. Självklart lät sig inte experimentalisterna stoppas av en teoretisk gräns, men ett rejält uppsving för forskningsfältet kom när Lundafysikern Sven Gösta Nilsson teoretiskt förutsade att grundämnen med 110-120 protoner inte bara bör kunna finnas, utan även kan vara relativt stabila!

Under 80- och 90-talen var det tyska laboratoriet GSI i Darmstadt ledande inom konsten att framställa tyngre och tyngre grundämnen, vilket återspeglas t.ex. i namnet Darmstadtium för grundämnet med 110 protoner. Därefter leddes jakten främst av det ryska laboratoriet JINR i Dubna, Ryssland. Där har forskare under de senaste tjugo åren framställt atomer som tros ha 113-118 protoner. Dessa atomer skapas en och en i laboratoriet, och det är i dagsläget bara möjligt att producera som mest ett par stycken om dagen.

De atomer som producerats hittills har väldigt korta halveringstider på maximalt ett par sekunder, och alltså sönderfaller de mycket snart efter att de skapats. Den korta livslängden beror till stor del på obalans mellan antalet neutroner och protoner. Tyvärr är det än så länge inte möjligt att få in fler neutroner i kärnorna, och därför är vi ganska långt ifrån det område där det förutspåtts att det ska finnas relativt stabila, alltså långlivade, atomer.

Ett annat problem i forskningen är att det är svårt att slå fast hur många protoner som faktiskt finns i kärnorna. Forskarna i Ryssland har försökt bestämma protonantalet indirekt, och fastän nästan alla är övertygade om att bestämningen är korrekt tycker de flesta att det inte riktigt räcker. Det är här som min forskning kommer in i bilden. Jag har utfört ett experiment vars syfte är att verkligen ta reda på protonantalet i nya atomkärnor.

En metod för att göra en direkt och otvetydig mätning av protonantalet är att studera röntgenstrålning from atomerna. Om man mäter strålningens energi kan man räkna ut hur många protoner som finns i kärnan, och alltså vilket slags atomer som finns i provet. Svårigheten i en sådan mätning ligger bland annat i att få kärnan att sända ut röntgenstrålning. För större materialprover, såsom t.ex. en bit av en meteor, kan man provocera fram röntgenstrålning genom att bestråla provet på något vis. I fallet med de enstaka atomer som produceras i mina experiment är denna metod inte möjlig. Det vi istället sätter vårt hopp till är att när atomerna sönderfaller kommer de ibland att bilda en dotteratom som har överskottsenergi som den kan sända ut i form röntgenstrålning. Då kan vi identifiera dotteratomen, och eftersom vi vet hur det initiala sönderfallet skedde kan vi identifiera den ursprunliga atomen.

Det fina med metoden är att man dessutom får ut mycket mer information. Observationer kring hur ofta det sänds ut röntgenstrålning, huruvida annan strålning sänds ut och exakt hur och när sönderfallen sker

berättar om hur atomkärnorna ser ut i detalj. Det som förklarades av bland andra Maria Goeppert-Mayer är att protonerna och neutronerna som finns inne i kärnan arrangerar sig enligt vissa mönster. Liksom man tänker sig att elektronerna snurrar runt atomkärnorna i olika skal, snurrar protonerna och neutronerna i skal runt en punkt i mitten av atomkärnan. Genom att studera dessa skal noggrannare och noggrannare, får vi bättre och bättre ledtrådar om hur krafterna inne i kärnan verkligen fungerar. Ju mer vi lär oss om krafterna, ju bättre kan vi förstå och utveckla de goda tillämpningar av kärnfysik som finns idag och imorgon.

Under mina första år som doktorand var jag med och utvecklade utrustning för att kunna göra en detaljstudie av element 115 och dess sönderfallsprodukter. I slutet av år 2012 utförde vi vårt experiment, och sedan dess har vi grävt djupare och djupare i de data vi samlade in. Vi har kalibrerat vår utrustning, vi har rekonstruerat sönderfallen, vi har jämfört med simulerade sönderfall, vi har räknat på olika sannolikheter, och vi har försökt kommunicera våra upptäckter till omvärlden. Denna avhandling innehåller en översikt över experimentet och redogörelser för vad jag har gjort.

Acronyms

SHE SuperHeavy Element

GSI Gesellschaft für Schwerionenforschung

LINAC LINear ACcelarator

TASCA TransActinide Separator and Chemistry Apparatus

HTM High Transmission Mode

SIM Small Image Mode

TASISpec TASCA in Small Image mode Spectroscopy

DSSSD Double-Sided Silicon Strip Detector

SSSSD Single-Sided Silicon Strip Detector

TDC Time-to-Digital Converter

ADC Analog-to-Digital Converter

NIM Nuclear Instrument Module (electronics standard)

VME Versa Module Europa bus (electronics standard)

Contents

1

Introduction

"Element 115" is the placeholder name for the chemical element which consists of atoms with 115 protons in the atomic nucleus. Although there are long-standing wild speculations about its use as UFO fuel (see, e.g., Ref. [1]) and its ability to turn humans into zombies (see, e.g. Ref. [2]), the first scientific evidence for the existence of atoms of this kind came in the year 2004 [3]. Scientists working at the laboratory Joint Institute for Nuclear Research (JINR) in Dubna, Russia, reported that they had created element 115 atoms by gently colliding atoms of calcium and americium. They had observed series of radioactive decays from atoms formed in this reaction in a detector station placed after a gas-filled magnetic separator, and assigned them to stem from atoms of element 115. However, no direct result concerning the proton number was achieved. The nuclear structure group at Lund University – which I am part of – took up this quest. Our main aim was to make an unambiguous determination of the number of protons inside the atomic nuclei and by this verify that "element 115" indeed exists and has been produced and observed.

In 2010 our group sent in an experiment proposal to the Gesellschaft für Schwerionenforschung (GSI), Darmstadt, Germany. The time re-

quired at the accelerator laboratory to achieve our goals was estimated to be twelve weeks. Eight of those weeks were granted. In June 2011 we spent one week testing and preparing for the main experiment. In October 2012 a three-week experiment was scheduled to November 2012. Initially, the idea was to maximise the yield of the isotope $^{287}115$. In three weeks, we expected to produce and observe three or four atoms of this type. Calculations made by our colleagues at the Division of Mathematical Physics, Lund, estimated that for each observed atom of element 115 we would see one of the desired X rays that serve as proton-number indicators. As this would not be sufficient for an unambiguous determination of the proton number, we decided to instead take a chance on the isotope $^{288}115$. The production rate of this isotope is almost ten times higher than for the isotope $^{287}115$, but no estimation could be made for the number of expected X rays. After about two weeks of experiment, a few potential X rays and several γ ray events had been observed. It was decided to change the beam energy such that instead the expected yield of $^{289}115$ was maximised. Unfortunately, neither X rays nor γ rays were found in the seven chains that were tentatively assigned to $^{289}115$. Although no unambiguous proton number determination was achieved due to the low number of observed potential X rays, we proved that this type of measurement is indeed technically feasible within a relatively short period of beam time. In turn, the observed γ rays – that can be considered an extravagant bonus – provided the very first insights into the nuclear structure of the heaviest elements known.

In this thesis, I start with an overview of the exciting field of superheavy nuclei: What are they? How are they created, studied, and identified? What kind of equipment is used and where is the research being made? Then, I present an overview of the history of element 115 in particular. In the following chapter I describe the experimental setup that was used in our study of element 115. Next, I describe the prepara-

tions of and results from a test-experiment that we performed in order to make informed decisions for the main experiment. Then I describe the analysis procedure – some parts in more detail than others – and our statistical assessments of the data. I proceed by showing the results and interpretations of our data, and I end with a conclusion and an outlook.

2

Superheavy elements

The chemical elements are arranged in rows and columns in the Periodic Table of Elements by the number of protons in their atomic nuclei *and* similarities in their chemical properties. A Periodic Table of Elements is shown in Fig. 2.1. The number of protons, Z, determines the number of electrons, and these, in turn, determine the chemical properties of the atoms. It turns out that certain chemical properties are repeated after some time: For example, atoms in the rightmost column are inert noble gases, while the alkali metals in the leftmost column are very reactive.

The lightest element hydrogen, with one proton in the nucleus, is found in abundance in the Universe. Slightly heavier elements such as carbon and oxygen with six and eight protons, respectively, form a major part of living creatures. Silicon and iron, with fourteen and 26 protons, contribute to the crust and the core of the Earth [4]. The heavier elements gold and mercury, with 79 and 80 protons, are found in small amounts and are important in technical applications. Bismuth, with 83 protons, is the heaviest element which is generally considered stable – its half life is much longer than the age of the Universe [5]. Uranium with 92 protons is the heaviest element that is known to be primordial to Earth [6], i.e. it has existed on Earth since its creation.

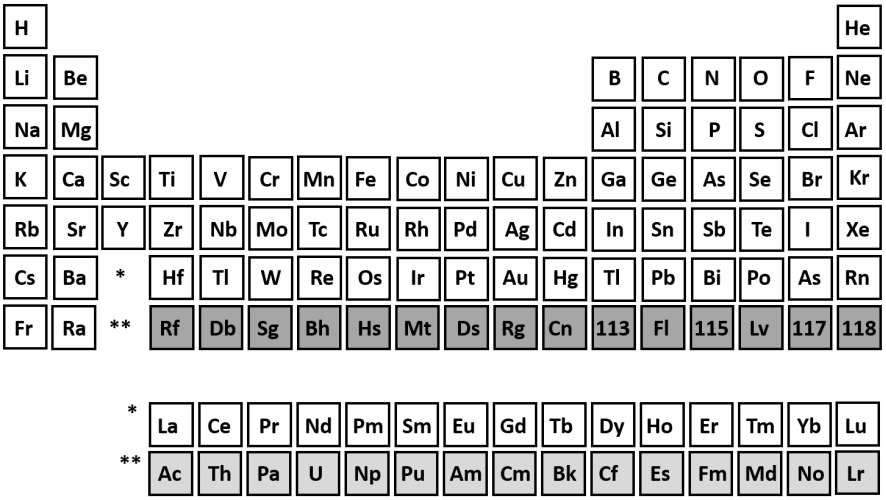

Figure 2.1: *Periodic Table of Elements. The actinides are shaded in light grey, and the transactinides – also called superheavy elements – are shaded in dark grey.*

Elements with 89 to 103 protons are called actinides and are found in the lower "extra" row in the Periodic Table of Elements, which represents those elements that should be placed between radium (Ra, $Z = 88$) and rutherfordium (Rf, $Z = 104$). Americium and californium with 95 and 98 protons are today created with relative ease in laboratories and used in, e.g., fire alarms and for searching for oil.

Elements with more than 103 protons are denoted SuperHeavy Elements (SHE) or transactinides. The fascination for these atoms lies to a large extent in the theoretically predicted increase in stability that might occur around element 114, as was thoroughly discussed by Sven Gösta Nilsson [7] at the end of the 60s. Atoms with up to 118 protons have been observed in laboratories, and the International Union of Pure and Applied Chemistry (IUPAC) has approved all of these claims [8, 9, 10]. Hence, the scope of chemistry covers – so far – a total of 118 types of atoms and their properties. Hunts for elements 119 and 120 are still un-

successful, but hopes are good that several new elements will be added to the Periodic Table of Elements within the coming decade.

From a nuclear physics perspective, the number of neutrons is just as important as the number of protons in the nuclei. Each of the chemical elements comes in several different isotopes, which are characterised by the number of neutrons. The known isotopes amount to about three thousand [11], and are arranged in the Chart of Nuclides (see Fig.2.2). Here, each isotope is drawn with one or more colours. Those that are black are stable, while the colours of the unstable isotopes indicate different kinds of radioactive decay. The radioactive, or unstable, nuclei have lifetimes which range from fractions of a second to billions of years.

The stable isotopes follow a curve that is bent downwards compared to the $N = Z$ line. This means that the more protons a nucleus contains, the more neutrons are required in order to form a stable nucleus. The isotopes of superheavy elements that have been produced so far are seen in the uppermost right corner. Compared to a continuation of the curve of stable nuclei, these isotopes suffer from a lack of neutrons. At first it could seem discouraging that the discovered atoms of superheavy elements around element 114 – where higher stability was predicted [7] – have half-lives of only seconds at best, but this is, arguably, mainly due to their neutron deficiency.

Exactly how long half lives we can hope for at the predicted "Island of Stability" is not known. Some calculations point towards half lives on the order of thousands of years, while other are more conservative. What all models agree on, though, is that it is internal nuclear structure effects that make it possible for nuclei of more than about one hundred protons to exist: Without these, the electrostatic Coulomb repulsion is expected to tear the nuclei apart, regardless of the number of neutrons.

The empirical fact that some nuclei are more bound than others, in the sense that the energy it takes to remove one proton or neutron is

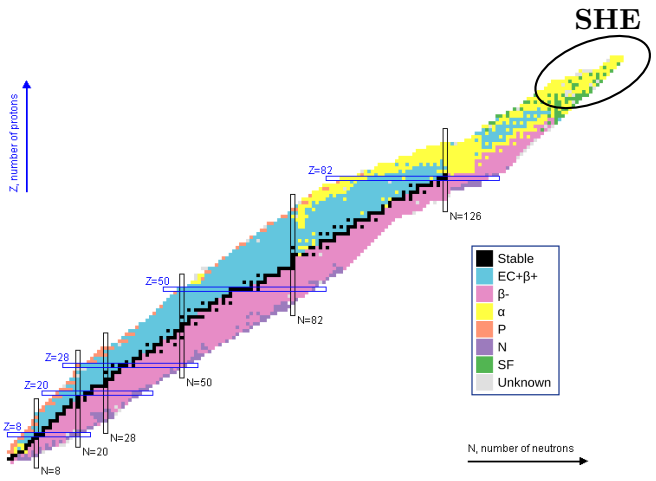

Figure 2.2: *Chart of Nuclides. Known isotopes are sorted according to proton and neutron numbers. The superheavy elements are located in the uppermost right corner. The picture is taken from Ref. [12] and is in the public domain.*

significantly larger for some proton and neutron numbers than others, is explained by the nuclear shell model. Just like electrons, the nucleons can be viewed as particles arranged in different shells. For spherical nuclei, the known "magic numbers" for protons are 2, 8, 20, 28, 50 and 82, and for neutrons they are 2, 8, 20, 28, 50, 82, and 126. These might be followed by a magic neutron number 184 and a magic proton number 114, 120 or 126, depending on the used model, leading to the prediction that the hypothetical nuclei $^{298}114$, $^{304}120$, or $^{310}126$ might be particularly stable, at least relative to how fragile the nuclei would be, had there been no shell structure. The theories further suggest that not only one particular nucleus will be particularly stable, but also nuclei in its vicinity. This motivates the name "Island of Stability".

The superheavy elements that we know of today have all been synthesised in laboratories. Whether they exist anywhere else in the Universe,

or not, is unclear. There have been searches for superheavy elements in terrestrial matter, but so far there has been no success [13]. Searches for signals from superheavy elements in space have led to the same discouraging result [14]. If superheavy elements are produced naturally, the currently most probable mechanism is the rapid neutron-capture process, assumed to take place when lighter nuclei are subject to extremely high fluxes of neutrons. Here, a nucleus picks up neutrons until an isotope with a very short half life is reached, and the nucleus transforms a neutron into a proton by undergoing β^--decay. Further neutrons are then picked up and the process continues. There is no known absolute limit to this process, and it could be that it creates superheavy elements [14]. Exactly where in our Universe this process would take place is still unknown, but the abundances of elements heavier than iron strongly support that this process indeed happens [15]. Possible places for occurrence involve violent stellar explosions, such as supernovae.

2.1 Creation of superheavy elements in laboratories

Superheavy elements have so far been created in fusion-evaporation reactions. A beam of ions is accelerated and impinges on a thin target foil. Very rarely, a beam nucleus merges with a target nucleus in the foil to form a compound nucleus in an highly excited state. The nucleus cools down by evaporation of nucleons and γ radiation, and a superheavy element is formed. Theoretical models of the reactions leading to superheavy elements have been developed by various groups (see, e.g., Refs. [16, 17, 18]). In general, the process is divided into three different steps as illustrated in Fig. 2.3.

Most often, two nuclei that come into contact with each other scatter elastically or inelastically, or exchange a few nucleons. These reactions

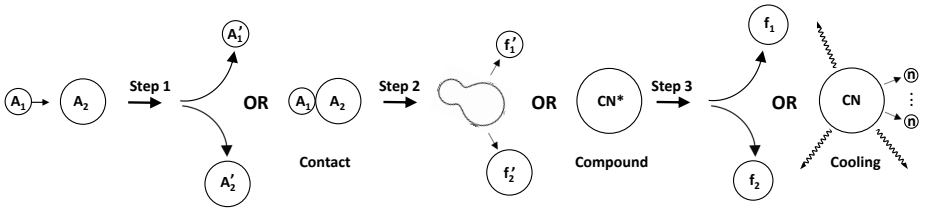

Figure 2.3: *Model for formation of superheavy elements in fusion-evaporation reactions. In step 1, the two nuclei may scatter or transfer nucleons, or come into contact configuration. In step 2, the nuclei may separate again, undergo quasi-fission or form an excited compound nucleus CN*. In step 3, the compound nucleus either fissions, or cools down by neutron and γ evaporation. Adapted from Fig. 1 in Ref. [16] and Fig. 1 in Ref. [17].*

lead to the formation of beam-like and target-like particles, denoted by A_1' and A_2' in Fig. 2.3. However, there is a probability that the projectile and the target nuclei overcome the Coulomb barrier and reach a contact configuration. The probability for this first step to happen is denoted $P_{contact}$, and depends strongly on the centrality in the collision. The two nuclei can separate again after exchange of a few nucleons or undergo quasi-fission. The fragments are denoted f_1' and f_2' in Fig. 2.3. The two nuclei can also fuse into an excited compound nucleus CN* and create a new element with probability $P_{compound}$. This compound nucleus might undergo fission and split into two fragments, denoted f_1 and f_2 in Fig. 2.3. The probability for this process increases with excitation energy. Alternatively, the compound nucleus cools down by emitting neutrons and γ rays, and reaches its ground state with a probability $P_{cooling}$. The final product is called an "evaporation residue". The number of evaporated neutrons depends on the excitation energy of the compound nucleus. A "hot" reaction is characterised by a compound nucleus with large amounts, around 40 MeV, of excitation energy, while a "cold" fusion reaction is characterised by a low, about 20 MeV, excitation energy [19]. Typically, only one neutron is evaporated from atoms created in "cold"

reactions, while two to four neutron evaporations follow upon "hot" reactions. The type of reaction is determined by the reaction kinematics and the Q-value of the reaction. The Q-value is the (positive or negative) energy that is released when the two nuclei fuse. If one of the nuclei is magic, or doubly magic, the Q-value is decreased and the reaction gets colder.

The probability for creating a superheavy element in a collision is the product of the probabilities for each of the steps: $P_{\text{contact}} \cdot P_{\text{compound}} \cdot P_{\text{cooling}}$. In general, it is beneficial to use cold reactions, both due to the higher P_{cooling} and due to the fact that less neutrons – that in general make the superheavy elements more stable – are lost from the compound nucleus. However, reaction kinematics, availability of projectile and target materials, and nuclear structure effects, can lead to high cross sections in hot fusion reactions.

The lightest of the superheavy elements were synthesised in hot fusion reactions with light beams (carbon, oxygen, etc.) on actinide targets. However, the cross sections for these reactions decrease strongly with Z. For elements heavier than seaborgium (Sg, $Z = 108$), the cross sections for these hot reactions are becoming too small. Instead, searches for new elements in cold fusion reactions took over. Already in the 1970s, rutherfordium was produced in a cold reaction between ^{50}Ti and the doubly magic ^{208}Pb at JINR, Dubna, Russia [20]. Continuing on this new method of using ^{208}Pb targets led to the discoveries of elements $Z =$ 107-112 at GSI, Darmstadt, Germany. Also for this type of reaction, the production cross sections decreased with Z (solid line in Fig. 2.4). The heaviest element that has been synthesised in this way is element 113, studied at RIKEN, Japan [21]. Only three atoms have been observed under an almost decade-long experimental campaign [22].

Around the turn of the millennium, the elements flerovium ($Z =$ 114) and livermorium ($Z = 116$) were claimed to be produced in "warm"

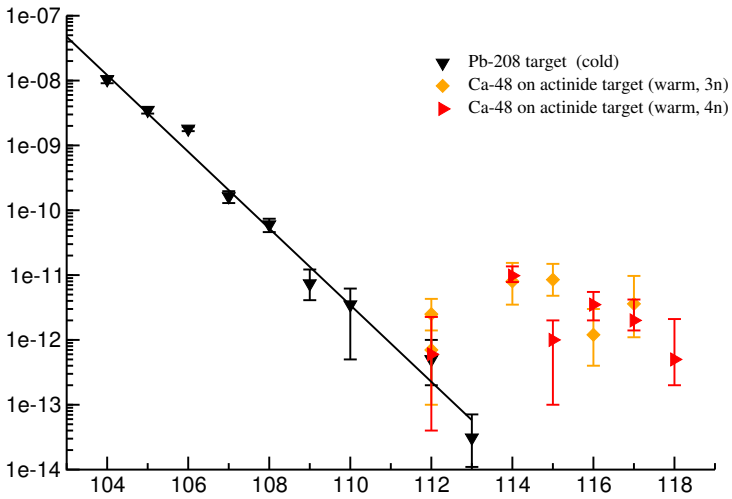

Figure 2.4: *The figure is constructed from a subset of the data presented in Fig. 2 in Ref. [19]. The main difference between the pictures are that two upper cross section limits have been excluded in this figure, elements below $Z = 104$ are not considered.*

reactions with the doubly magic projectile ^{48}Ca (calcium, $Z = 20$) on actinide targets [23]. This started a new era in the discovery of superheavy elements. Heavier elements than the newly approved element 118 are difficult to create in ^{48}Ca-induced reactions on actinide targets, mainly because it is very difficult to produce targets heavier than californium (Cf, $Z = 98$). The hitherto unsuccessful hunts for the elements 119 and 120 have been made using the projectiles titanium (Ti, $Z = 22$), chromium (Cr, $Z = 24$), iron (Fe, $Z = 26$) and nickel (Ni, $Z = 28$) on various actinide targets. However, neither of these beam species are doubly magic, which makes the reactions "hotter". The predicted cross sections decrease significantly as the projectile increases in Z, but it might well be possible to produce the elements up to $Z = 124$ by further increasing the proton number in the projectile [24].

2.2 Separation of superheavy elements

Superheavy nuclei created in fusion-evaporation reactions travel out of the target with essentially the same momentum as the beam. The desired events are rare, and the background consisting of other reaction products as well as the ions in the beam that did not react in the target is overwhelming. It is thus necessary to separate the different types of ions. Separation techniques that have proven useful are velocity filters, electrostatic deflectors, and gas-filled separators. In these, magnetic and/or electric dipole fields are applied to the flight path of the ions emerging from the target. The fields affect different types of ions differently, and deflect the unwanted ions into beam dumps. Separators are, in general, several meters long, and often contain extra multipole fields that focus the chosen ions into a small focal plane.

In a velocity filter the separation is made by applying both electric and magnetic fields. In the simplest setup, with perpendicular and crossing fields, only ions with the velocity $v = \frac{E}{B}$, where E is the electric and B is the magnetic field strength, pass through the filter. The unwanted ions have, in general, a higher velocity than the heavier fusion-evaporation products. The most prominent velocity filter used for superheavy element research is SHIP – Separator for Heavy Ion reaction Products (see, e.g., Ref. [25]) – at GSI. The elements Z = 107-112 were discovered by employing this separator.

In an electrostatic deflector, electric fields are used to separate ions. One such deflector is the VASSILISSA separator at JINR. It has been used for studying, e.g., the possibility to produce hassium (Hs, $Z = 108$) in the reaction ^{136}Xe+^{136}Xe [26]. Recently, VASSILISSA was upgraded and re-configured into a velocity filter [27].

In a gas-filled separator (for a review, see Ref. [28]), magnetic fields are used in order to separate ions according to their momentum-to-charge ratio. An ion acquires and loses electrons by interactions with the low-

pressure gas. The *average* charge is sensitive to the mass and velocity of the ion, and ions are separated roughly according to the ratio $A/Z^{1/3}$. The transmission through a gas-filled separator can be higher than in a velocity filter due to the generous charge and velocity acceptance, and the ease with which large geometrical acceptance can be constructed. The properties of gas-filled separators will be described in more detail in the next chapter.

The work presented in this thesis was performed at the gas-filled TransActinide Separator and Chemistry Apparatus (TASCA) at GSI, Darmstadt, Germany. The Dubna Gas-Filled Recoil Separator (DGFRS) at JINR, Dubna, Russia, was used in the experiments leading to the first observations of elements Z = 113-118 in ^{48}Ca-induced reactions. At RIKEN laboratory in Wako, Japan, the GARIS (GAs-filled Recoil Ion Separator) (see, e.g., Ref. [29]) has been used for studies of element Z = 113 in cold fusion reactions. Recently, the new separator GARIS-II was constructed in order to facilitate chemistry experiments on superheavy elements produced in hot fusion reactions [30]. The Berkeley Gas-filled Separator (BGS) at LBNL, Berkeley, USA, has been used in, e.g., decay studies of superheavy elements [31]. At the Jyväskylä Accelerator Center, Jyväskylä, Finland, the gas-filled separator RITU (Recoil Ion Transfer Unit) [32] has been used for studies of, e.g., isomeric states in nuclei around Z = 100 [33].

2.3 Detection of superheavy elements

The superheavy elements Z = 113 - 118 discovered so far are short-lived, with half-lives typically $T_{1/2} < 1$ s, and can only be studied via the detection of their decay products. They decay primarily by α emission, which transforms them into new nuclei with two protons and two neutrons less. These nuclei can, in turn, decay again by α emission. Eventually, the decay chain ends with spontaneous fission. The emitted α particles and

fission fragments can be straightforwardly detected in silicon semiconductor detectors. Observation of α-decay chains followed by fission in an otherwise relatively radiation-free environment is the most used method to detect superheavy elements to date.

The simplest detection setup is to place a silicon detector in the focal plane of a separator. The superheavy ions passing the separator would be implanted into the detector, and then undergo a series of decays that are subsequently measured in the detector. In reality, several optimisations are done. Firstly, since superheavy elements are created only very rarely – rates can be as low as one atom per day, week, or even month – the detection must be efficient. From a single detector, the probability that the α particle is emitted out from the implantation detector and escapes detection is 50%. To capture some of these escaping particles, silicon detectors can be placed upstream from the implantation detector to form the sides of a box. This usually increases the efficiency up to some 80%. Secondly, the background rate of radioactivity from unwanted nuclei is rather high in the focal plane detector due to imperfect separation. This calls for detectors that are position sensitive, such that one can search for series of decays in small separate areas of the implantation detector. By requiring that time-correlated events also are localised, they can be tied to the same implanted ion. The risks for random correlations of background events are reduced. Thirdly, the detectors should be able to measure the energy of the emitted particles accurately, and be able to detect small energy depositions.

In DGFRS in Dubna, a detector box consisting of several silicon segments that were read out using resistive charge division was used for the first observations of elements $Z = 114$-118, while an upgrade in 2012 has been made to increase the granularity [23]. In TASCA, a focal plane detector setup (see [34]) based on pixelised Double-Sided Silicon Strip Detectors (DSSSDs) has been used for element $Z = 117$ studies [34] and

searches for elements $Z = 119$ and $Z = 120$.

More elaborate detection setups contain also germanium (Ge) detectors capable of detecting electromagnetic radiation that might occur in conjunction with charged-particle decays. To obtain sufficient efficiency, these additional detectors must cover a large solid angle. Germanium detectors need to be cooled to liquid nitrogen temperature, and therefore tend to be bulky. Thus, special care must be taken when designing the full detector system.

At TASCA, the regular focal plane silicon box consisting of DSSSDs (see [34]) is situated inside a detector chamber. Easily available and relatively cheap germanium detectors have no chances of fitting inside that chamber, but, on the other hand, the solid angle would be too small if they were placed outside. Therefore, the alternative detector box TASISpec [35] was developed at Lund University. TASISpec is an array of five silicon strip detectors in the form of a small cubic box, which is mounted at the end of the TASCA chamber. Five large composite germanium detectors can be positioned closely around it – one behind each of the silicon detectors. This detector setup will be described in more detail later.

At the end of the Berkeley gas-filled separator, the C^3 detector [31] can be mounted. In C^3, atoms are implanted into one of three DSSSDs forming the corner of a cube, with one composite germanium detector placed behind each of the silicon detectors.

At the end of the VASSILISSA separator, the GABRIELA setup [36] has been tailored to measurements of both α, β and γ detection. The detectors in the silicon box are cooled in order to reduce noise, making it possible to use low detection thresholds, which enables detection of electrons that often have energies on the order of only hundreds of keV. The detectors also have very thin dead-layers. The box is surrounded by germanium detectors that are equipped with anti-Compton shields.

The GREAT spectrometer [37] is the detector array used at RITU. The box consists of two cooled and highly pixelised DSSSDs and an upstream array of PIN diodes. Planar double-sided germanium strip detectors are placed inside the detector chamber just behind the implantation detectors. Outside the chamber a regular composite Ge detector is placed.

2.4 Identification of superheavy elements

Just because correlated chains of α decays are observed in the focal plane of a separator in reactions with, e.g., ^{48}Ca on ^{243}Am, does not necessarily mean that element 115 has been produced. There is a certain probability that either a proton or an α particle is evaporated instead of just neutrons. Such reaction channels are seen in other fusion-evaporation reactions, but they are generally believed to be strongly suppressed in the production of superheavy elements [17, 38]. There is also a certain probability that background events mimic correlated chains, that the observed decays are from nuclei created in fusion reactions with impurities in the target material, or that the decay chains are not from superheavy elements but new isotopes of lighter elements. If the decay would proceed to known nuclei in the well-established part of the nuclear chart, the atomic number could be determined by identifying a decay daughter and add to this nucleus the measured decay products that have been emitted. Unfortunately, the so far observed α-decay chains from elements $Z > 113$ all end with fission before reaching previously known nuclei.

The Transfermium Working Group (TWG) – put together by the International Union for Pure and Applied Chemistry (IUPAC) and its physics counterpart IUPAP – defined in 1991 a set of guidelines for what is needed in order for a new element to be accepted and added to the Periodic Table of Elements [39]. They present a list of indicators for discovery of a new element. Among these one finds cross bombardment,

yield curves, chemical investigations and X-ray spectra.

Cross bombardment means that the same nuclide and its characteristic decay chain is observed in different reactions, e.g., when an isotope of element 115 is created both in the direct reaction ^{48}Ca + ^{243}Am and as the α-decay daughter of element 117 created in the reaction ^{48}Ca + ^{249}Bk. Cross bombardment was the prime argument when the elements 113-118 were approved [8, 9, 10].

A yield curve shows the cross section for observation of a decay chain as a function of the beam energy. These curves tend to have a typical shape if the decay chains indeed come from a fusion-evaporation reaction.

Chemical separation can be applied to long-lived atoms. Observation of radioactive decay from a purified sample can prove the presence of a certain element, which in turn might testify that indeed its ascendants must have been created.

The TWG writes in their report from 1991 [39] that "Very few properties indeed, of which perhaps the only uncontentious example is the characteristic X-ray spectrum, unambiguously determined, are sufficient of themselves to establish the existence of a new element." The energies of various X rays emitted from atoms are characteristic to the element, and can be accurately and precisely calculated together with their relative intensities. Therefore, a measured spectrum of electromagnetic radiation from a superheavy element showing the expected characteristics from X rays would be the ultimate argument for the identification of a new element. The first superheavy element rutherfordium (Rf, $Z = 104$) was successfully identified by this method in 1973 [40]. In coincidence with α decays from the presumed element $Z = 104$ into excited states in the daughter nobelium (No, $Z = 102$), an X-ray spectrum agreeing with predictions for $Z = 102$ emerged. The X rays are emitted when excited states in the daughter nucleus de-excite by internal conversion, leading to the emission of an electron from, preferentially, the K or the

L electron shell. Subsequently, the vacancy is filled by an outer electron and Auger electrons and/or the wanted X rays are emitted. Prior to the work presented in this thesis, no unambiguous X-ray spectrum has been acquired for any of the elements Z = 113-118.

3

Element 115 - a brief history

In total, 113 decay chains from the presumed element 115 have been observed in the reaction ^{48}Ca + ^{243}Am. Twenty spontaneous fission events in chemically purified samples have been assigned to element 115. On top of that, element 115 is assumed to have been produced also as the decay daughters of 22 atomic nuclei of element 117 produced in the reaction ^{48}Ca + ^{249}Bk. Figure 3.1 shows one view of how the observed decay chains can be interpreted. A time line showing the various experiments is found in Fig. 3.2.

Following successful experiments leading to the first reports on even-Z elements 114, 116 and 118, a months-long experiment on element 115 was performed at JINR, Dubna, in 2003. They used a beam of ^{48}Ca on a target of ^{243}Am and detected the products in a silicon box detector placed in the focal plane of DGFRS. The results were presented in Ref. [3] – the first publication on the production of element 115. Three of the observed α-decay chains were assigned to ^{288}115 and one to ^{287}115. The estimated cross sections were $\sim$ 4 pb and $\sim$ 1 pb, respectively. In a following publication [41], the experiment and the results were presented in

detail, together with details from a chemistry experiment first presented in two conference proceedings [42, 43]. These proceedings report on the observation of fifteen spontaneous fission events in chemically purified samples from a copper block placed behind the target. The observed fission events were proposed to signal that the five-α decay daughter of element 115, dubnium (Db, $Z = 105$), was present. The next report on element 115 is found in Ref. [44], where improved schemes for chemical separation of dubnium were applied during an experiment in late 2005. They led to the observation of five spontaneous fission events.

The next evidence for the existence of element 115 came with a report in 2010 [45] on the production of element 117 at JINR from an experiment running between summer 2009 to spring 2010. Six decay chains were observed in the reaction ^{48}Ca + ^{249}Bk. Five of them were assigned to the isotope ^{293}117 and one to the isotope ^{294}117. These nuclei decay to the element 115 isotopes ^{289}115 and ^{290}115, respectively. The chains were presented in detail in Ref. [46].

From November 2010 until March 2011 a second experiment on directly produced atoms of element 115 was performed. The results were mentioned in 2011 in conference proceedings [47] following the conference FUSION11 in early May 2011. The main results were communicated early 2012 in Ref. [48]. 21 atomic nuclei assigned to ^{288}115 were found. Additionally, one chain assigned to ^{289}115 was presented. This was different from all the other chains observed so far, since it consisted of only two α decays in contrast to the previously observed chains with five α decays. This single chain, suggested to start with ^{289}115, was considered very valuable as it seemingly provides a first cross bombardment connection between element 117 and 115 chains.

A third experiment using the reaction ^{48}Ca + ^{243}Am was undertaken from September 2011 until February 2012. One chain assigned to ^{287}115 was found, seven chains were assigned to ^{288}115 and three chains were at-

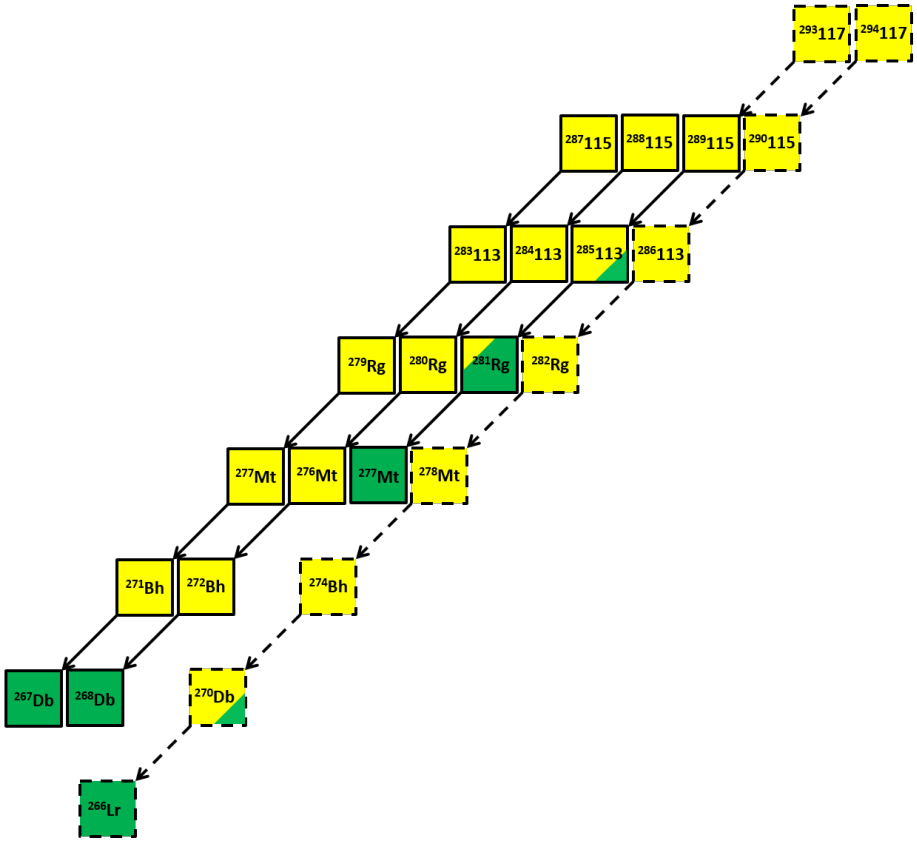

Figure 3.1: *Overview of element 115 decay chains. Dashed frames indicate decays which have been observed in the reaction* $^{48}Ca+^{249}Bk$*. Yellow boxes symbol* α *decaying nuclei, while green boxes symbol spontaneous fission. Boxes containing both yellow and green fractions have branching ratios corresponding roughly to the yellow and green areas. The figure presents* one *view of how the current world data set could be interpreted.*

tributed to ^{289}115. The combined results from all three campaigns were presented early 2013 [49], now comprising a total of two ^{287}115 chains, 31 ^{288}115 chains, and four chains assigned to the important isotope ^{289}115. However, this publication is not the first to present the results: On May 22, 2012, a JINR internal report was filed [50], in which the average times and energies of the chains starting with element 115 are presented together with the data from the first element 117 experiment. The cross bombardment case is highlighted. A conference proceeding [51] following the conference NN2012 (held 27 May to 1 June 2012) presents the four chains assigned to ^{289}115 and emphasises the cross bombardment. Similar material was presented in the conference proceeding [52] from the conference HITES2012 held 4-7 June 2012.

Next in time was a second experiment at JINR using ^{48}Ca + ^{249}Bk. While the experiment was still under way, seven of the chains observed in the first part of the experiment were published in Ref. [53]. Two were assigned to the isotope ^{294}117 and five to the isotope ^{293}117. These seven chains were mentioned in Ref. [49] (see previous paragraph), where they were used to reinforce the cross bombardment case presented in Refs. [50, 51, 52]. The continued experiment yielded one more chain assigned to ^{294}117 and six more assigned to ^{293}117. The chains were presented in May 2013 in Ref. [54] together with an overview of both ^{48}Ca + ^{249}Bk campaigns at JINR. At that time, the number of element 117 chains assigned to the isotopes ^{294}117 and ^{293}117 were four and sixteen, respectively.

In parallel with the element 117 campaign at JINR, a similar month-long experiment was performed at GSI. Reaction products from the reaction ^{48}Ca + ^{249}Bk were separated using TASCA and detected using a silicon box detector. Two chains similar to those previously assigned to ^{293}117 were published in 2014 [34].

Just after the experiment on element 117 at GSI, another three-week long GSI experiment on element 115 started. The experiment was led by the Lund nuclear structure group, and aimed at observing the decay of element 115 and to properly determine the atomic number by observation of characteristic X-rays. This experiment is the main focus of this thesis. The highly efficient TASISpec detector, capable of observing not only charged particles but also coincident electromagnetic radiation, was used with the TASCA separator. In the experiment, 30 α-decay chains were detected. One was assigned to ^{287}115 and 22 were assigned to ^{288}115. Seven short chains were similar to the majority of those previously assigned to ^{289}115. In general, the experiment confirmed the previous findings at JINR. X-ray candidates were observed in ^{272}Bh – a member in the decay chains starting from ^{288}115 – although not sufficiently many to unambiguously determine the proton number. Highlights from this experiment were presented first at the International Nuclear Physics Conference 2013 (INPC2013), and then in Ref. [55] (Paper II). The intent of performing this experiment was publicly presented first in Ref. [56] (Paper I) in 2012 where preparatory experiments were discussed. Various aspects of the analysis [57, 58] and the results [59, 60, 61, 62, 63, 64, 65] were presented at conferences, in conference proceedings, and in GSI Annual Reports. In these articles, some inconsistencies in the data on ^{289}115 are brought up. These questions are thoroughly discussed in Paper V [66].

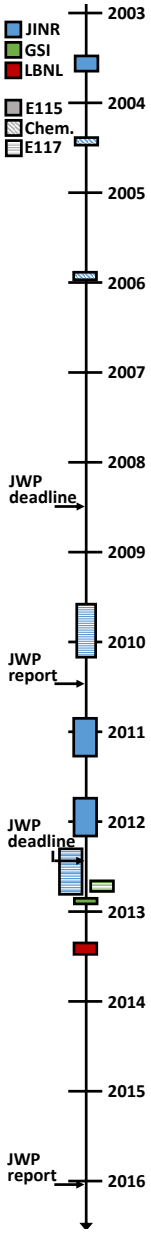

Figure 3.2: *Element 115 time line.*

During the spring and summer of 2013, another experiment on X rays and γ rays from element 115 decay chains was performed using the detector setup C^3 at BGS, Berkeley. The results were presented in Ref. [31] in 2015. No less than 46 decay chains were reported; 43 were assigned to start from $^{288}115$ and three were not assigned to a specific isotope since they were similar to the questioned short chains originally assigned to $^{289}115$.

Overviews of the experiments with ^{48}Ca beams at JINR have been made in 2007 [67], 2011 [68] and 2015 [23, 69]. There may also be conference articles that summarise experiments and results that I may have overlooked.

Alongside the experimental efforts runs another story. The IUPAC/IUPAP Joint Working Party (JWP) has been assigned the task to evaluate the claims of new elements with respect to the criteria set up by the TWG [39]. JWP decides when new elements should be added to the official IUPAC Periodic Table, write discovery profiles in which the different contributions to discoveries are evaluated, and invite one or more groups of scientists to propose a permanent name for the element. After a five-month long period when the public can have their say about a suggested name, IUPAC makes the decision. In 2011, JWP decided that sufficient proof for element 115 had not yet been gathered [8]. In particular for the odd-Z isotopes, a determination of the proton number, Z, was called for [8]. However, on the night before New Year's Eve 2015, IUPAC announced on their web page that JWP had proposed that element 115 should be added to the Periodic Table of Elements, and that the group of scientists performing the experiments at JINR are welcome to suggest a name. The IUPAC Technical report [9] made available later in mid January 2016 outlines the background to the decision: The claimed cross bombardments where the nucleus $^{289}115$ was created in the two different fusion-evaporation reactions ^{48}Ca + ^{243}Am and ^{48}Ca + ^{249}Bk.

4

Experimental setup

The experimental setup used in our studies of element 115 consists of many different parts. It is difficult for one researcher to know each and every aspect of the experiment in detail. Not even the combined knowledge of the 53 co-authors of our main publications [55, 56, 57, 59, 61, 66] is enough. Superheavy element research requires an accelerator laboratory with a staff that handles day and night operation, maintenance, and the problems that inevitably arise when machines are forced to perform at the very frontiers of their capabilities for weeks or months. It requires radiation safety officers, legal experts, and administration on many levels.

In this chapter, I will give an overview of the main technical aspects of the experimental setup. Those parts of the setup that I have been more involved in will be described in more detail. In Fig. 4.1, a schematic picture illustrates the main constituents – the UNILAC accelerator and the TASCA separator that are part of the GSI host laboratory, the TASISpec detector, which was built mainly in Lund, and the electronics, which are partly from Lund and partly from GSI. I will also describe two sets of simulation programs that have been used for preparation, determinations of experimental settings, and for evaluation of various interpretations of the experiments. To simulate transport of ions through TASCA, a set of

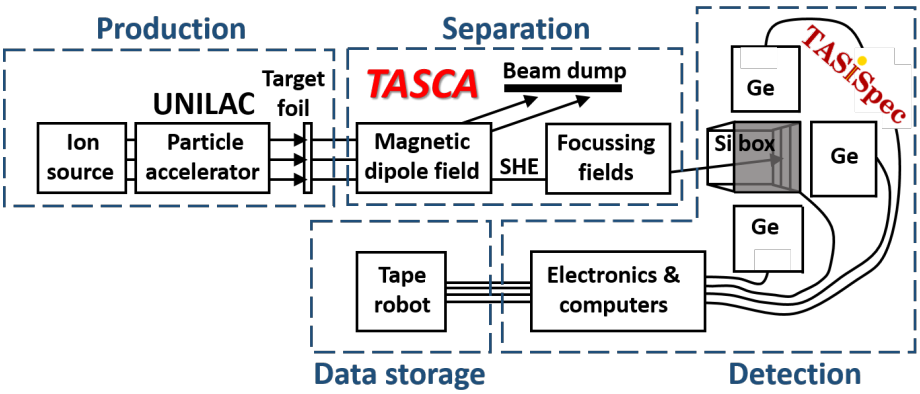

Figure 4.1: *Overview of experimental setup. To produce superheavy elements, a beam of calcium ions was accelerated by UNILAC and let to impinge on a target foil of actinides. The superheavy elements are separated from other ions in the TASCA magnetic gas-filled separator. The ions are directed towards TASISpec and are implanted into a silicon strip detector. The subsequent radioactive-decay products are recorded in these detectors and in surrounding germanium detectors. The signals are processed using electronics and computers, and finally stored on the GSI tape robot.*

C++ programs and `SRIM` [70] have been used. To simulate the response of TASISpec when nuclei with certain decay characteristics are implanted and subsequently decay, a virtual TASISpec in `Geant4` [71, 72] space has been used.

4.1 Particle beam

In our experiments, a beam of $^{48}Ca^{10+}$ ions is one of the key ingredients. Commercially available isotopically enriched calcium is ionised in the Electron Cyclotron Resonance (ECR) ion source ECRIS CAPRICE 1.0 T. The ions are subsequently accelerated in UNILAC (UNIversal Linear ACcelerator). UNILAC can accelerate ions up to energies of several MeV per nucleon. The beam is pulsed with a duty factor of 25%, such that

the beam is on for 5 ms and off for 15 ms. The beam energy can be determined with an uncertainty of about 1‰, and is checked at least once per day. The beam is directed to the experimental hall through a beam line. Several focussing quadrupole magnets are used along the way. The beam spread can be controlled, and measured using various wire grids that can be placed in the beam. The beam current is continuously monitored by induction coils at various positions along the beam line, whereof one is positioned as close as possible to the target. The current given by the induction coils is regularly related to measurements with a Faraday cup just before the target. The charge state of the ^{48}Ca ions is 10^+ and common beam intensities are about 1 particle-μA (actual current divided by the charge state of the ions, around $6{\cdot}10^{12}$ ions per second) when averaged over the beam structure. The pressure in the beam line leading to the experimental hall is about 10^{-6} Pa [73], while the pressure inside TASCA is on the order of one mbar. A differential pumping system is installed between TASCA and the beam line from the accelerator [73]. It consists of a series of small apertures followed by powerful vacuum pumps that gradually decrease the pressure.

4.2 Target

The target is a thin foil. To support the target material, it is deposited on a backing foil. In the experiment described in this thesis, two different target materials were used. In a preparatory experiment we used ^{208}Pb as target material and a ^{48}Ca beam to produce nobelium. The target was produced at GSI by the target laboratory. ^{208}PbS was thermally evaporated onto a thin carbon backing foil [74]. The target layer is covered by an additional carbon layer to prevent sputtering during the irradiation. For production of element 115 the target material was ^{243}Am, which in itself is radioactive with a half life of about 7000 years. It was produced by high-flux neutron irradiation at the Oak Ridge Na-

tional Laboratory and further processed at Mainz University. Titanium foil was selected as backing material because of its good mechanical and thermal stability [75]. Americium was dissolved in isobutanol and layers of several hundreds of μg/cm^2 of americium were deposited on $\sim$2.2 - 2.3 μm titanium backings by molecular plating (electrodeposition) [76]. Just after production, the targets are in the chemical form of americium oxide containing small amounts of solvent. While being irradiated by the beam the solvents trapped inside the target material are evaporated, and the previously amorphous structure is likely to approach a more ordered crystalline structure. The target does not necessarily take on a specific crystalline structure, neither is it necessarily chemically stable after reaching a crystalline state [77]. In the following, the structure Am_2O_3 with a density of 10.57 g/cm^3 will be assumed. The target thicknesses were measured by detection of radiation from the target material [76].

Eight arc-shaped target segments were produced and mounted on two rotating target wheels [73] (target wheel 1 and 2). The backings face the beam. Figure 4.2 shows the ^{243}Am target wheel that was used during our experiments. Each segment has an area of 5.93 cm^2. The beam can be de-focused such that it covers the entire target area. The target wheel rotates with 2250 revolutions per minute and is synchronised with the beam structure. The rotation of the wheel, as well as the de-focusing of the beam spot, prevents over-heating of the target. The temperature can be continuously monitored with a pyrometer.

The Am target characteristics are summarized in Table 4.1 and Table 4.2, where backing thicknesses, target thicknesses of ^{243}Am and the actual thickness when the oxide Am_2O_3 is assumed are given. Target wheel 1 was used during the experiment.

Figure 4.2: *Americium target wheel used for the experiment. The target wheel diameter is 10.0 cm. The radial width of the segments is about 8 mm.*

Table 4.1: *The thicknesses of the segments in target wheel 1, in both μm and mg/cm^2 for the Ti backing, and in mg/cm^2 for the target layer.*

Segment	Backing (μm)	Backing (mg/cm^2)	^{243}Am	Am_2O_3
1	2.2	0.99	0.714	0.785
2	2.2	0.99	0.791	0.869
3	2.2	0.99	0.782	0.859
4	2.2	0.99	0.726	0.798
Average	2.2	0.99	0.753	0.828

Table 4.2: *The thicknesses of target wheel 2 segments, in both μm and mg/cm^2 for the Ti backing, and in mg/cm^2 for the target layer.*

Segment	Backing (μm)	Backing (mg/cm^2)	^{243}Am	Am_2O_3
1	2.2	0.99	0.634	0.697
2	2.3	1.04	0.758	0.833
3	2.3	1.04	0.534	0.587
4	2.2	0.99	0.824	0.905
Average	2.25	1.015	0.688	0.755

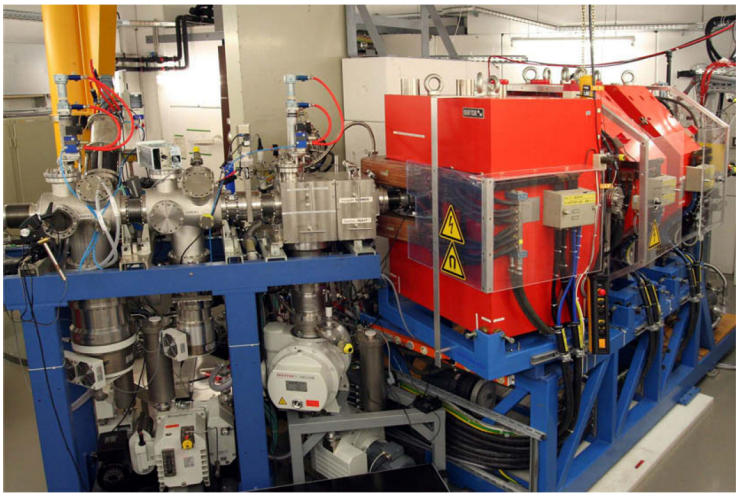

Figure 4.3: *The TASCA separator. The beam from UNILAC enters the experimental cave through the beam line seen in the left part of the figure.*

4.3 TASCA

Superheavy elements are not the only kind of nuclei that are produced in the nuclear reactions. The desired superheavy ions hence have to be separated from the background of other particles. The ions from the beam that pass through the target without any nuclear interactions (primary beam) need to be removed, as well as transfer reaction products, in which a few nucleons have been transferred from the projectile to the target, or vice versa. The superheavy ions produced in the target have almost the same momentum as the beam. This fact is used in the gas-filled separator TASCA (Transactinide Separator and Chemistry Apparatus) [78, 79]. TASCA is placed right after the target wheel. A photography of TASCA is shown in Fig. 4.3. TASCA separates particles and focuses superheavy elements towards two detector chambers in which a variety of detectors can be positioned.

Separation of superheavy elements from transfer products and pri-

mary beam in TASCA is achieved by a magnetic dipole field which separates the particles according to their *magnetic rigidities* $B\rho$ (momentum-to-charge ratios):

$$\frac{mv}{q} = B\rho \tag{4.1}$$

where m, v, and q are the mass, velocity and charge of the particles, respectively, B is the magnetic field and ρ is the bending radius. By varying the magnetic field, particles of different magnetic rigidities are selected, and particles that are of the wrong $B\rho$ are directed towards a water-cooled beam dump.

Since TASCA is a gas-filled separator, the charge of the travelling ions varies around an average charge state which depends on various factors, such as gas composition and pressure in the separator, and on the electronic structure of the ion itself. The estimation of the average charge state is very important for the calculation of the optimal magnet settings. It is also crucial to have an approximate understanding of the magnetic rigidity of the interfering products.

A first approach to finding the average charge state, suggested by Bohr already in 1940 [80], is to assume that all electrons having an orbital velocity greater than the velocity of the atom travelling in the gas will remain attached to the ion, whereas the rest will be stripped. According to Ref. [81], the number of electrons with a velocity less than the velocity v of the atom, and hence the average charge state $\bar{q}$, given in number of elementary charges, is

$$\bar{q} = \frac{v}{v_0} \cdot Z^{1/3} \quad \text{when} \quad 1 < \frac{v}{v_0} < Z^{2/3}, \tag{4.2}$$

where $v_0 = 2.19 \cdot 10^6$ m/s is the Bohr velocity. Rewriting the magnetic rigidity by insertion of $\bar{q} = q/e$ (where e is the elementary charge) and Eq. 4.2, and by approximating the mass by A atomic mass units, gives

an expression which depends only on the intrinsic properties A and Z of the atoms:

$$B\rho = \frac{mv}{q} = \frac{mv_0}{e}\frac{1}{Z^{1/3}} = 0.0227\frac{A}{Z^{1/3}}\mathrm{Tm} \tag{4.3}$$

For example, the reaction ^{48}Ca on ^{208}Pb produces target-like transfer reaction products like ^{211}Bi and ^{211}Po. For these, $\frac{A}{Z^{1/3}} \sim 48$, while $\frac{A}{Z^{1/3}} \sim 54$ for the fusion-evaporation residue ^{254}No, and $\frac{A}{Z^{1/3}} \sim 18$ for the primary beam. From these estimations, the primary beam is expected to be easily separated from the superheavy elements. However, the transfer reaction products may pose a problem since they only differ by about 10% in $B\rho$ from the wanted products.

Detailed studies of the average charge of ions traversing low-pressure gases have been performed at various laboratories (see, e.g., Refs. [82, 83, 84]). The general trend of $\bar{q}$ (Eq. 4.2) is confirmed by Ghiorso et al. [82], although with deviations. Part of these deviations can be assigned to effects from the atomic shell structure. To incorporate these deviations, Gregorich et al. [85] modified the function $\bar{q} \propto \frac{v}{v_0} \cdot Z^{1/3}$, mainly by adding a sinusoidal correction, and fitted the parameters to available data from heavy nuclei with proton numbers up to Z=111. The function derived for the average charge state is [85]

$$\bar{q} = 0.641x - 0.235 + 0.517 \cdot \sin\left(\frac{2\pi}{32}[Z - (0.641x - 0.235) - 74.647]\right) \tag{4.4}$$

where $x = \frac{v}{v_0} \cdot Z^{1/3}$.

For the superheavy elements with $Z > 111$, the predictions are less accurate. The first experiment on superheavy elements at TASCA showed that the predicted $B\rho$ for element 114 was lower compared to measurements, meaning that the average charge state is higher than expected from Eq. 4.4 [86]. A correction factor of a few percent needed to be applied to the formula. When element 117 was measured at TASCA [34],

a similar factor was needed. The exact factors depend on various estimated experimental details. Comparisons between my calculations and experimentally measured $B\rho$ lead to correction factors of 1.055 for both element 114 and 117. So far, this correction factor is added only in the very last step of the procedure to calculate the $B\rho$ for a truly superheavy element.

In TASCA, the magnetic dipole is followed by two quadrupole magnets, which focus the evaporation residues to the focal plane. Different transmission and focusing properties can be achieved by using different polarities of the two magnets. In High Transmission Mode (HTM), the dipole provides the separation while the quadrupoles focus the particles to the detectors. The dispersion in TASCA is about 0.9 cm/% $B\rho$ [78] in HTM, resulting in evaporation residues and transfer reaction products being spatially separated by around 9 cm at the TASCA focal plane. In the so-called Small Image Mode (SIM), the first quadrupole is part of the separation process since it narrows down the span of magnetic rigidities that particles reaching the focal plane of TASCA can have.

In SIM, the evaporation residues are focused into a small beam spot of about 3 cm in diameter, with a transmission of about 35-40% to the focal plane of TASCA for ^{48}Ca-induced reactions [87]. The small beam spot allows for a good transmission from the focal plane through the tube leading to the TASISpec setup. Simulated trajectories of evaporation residues through TASCA in SIM are shown in Fig. 4.4 (top row). The left panel is a top view and the right panel is a side view of TASCA. The outline of TASCA is only schematic, and some simplifications have been made. In SIM, the first quadrupole focuses in the vertical direction ($Q_1 = Q_v$), which causes a de-focusing in the horizontal plane. This causes an inevitable loss of particles in the walls of the TASCA quadrupoles, but allows for a strong overall focusing into the very small beam spot in the focal plane. The effect of the second quadrupole is the focusing in the

horizontal plane ($Q_2 = Q_h$) and the de-focusing of the previously narrow distribution in the vertical direction.

The HTM gives a transmission to the focal plane of the separator of about 60% for ^{48}Ca-induced reactions, but with a beam spot approximately 12 cm wide and 4 cm in height. The large beam spot causes particles to be lost in the TASISpec entrance tube with diameter 6.6 cm, giving an overall transmission to TASISpec considerably smaller than 60%. In HTM, the polarities of the quadrupoles are reversed as compared to SIM. Switching between the two modes is achieved by re-cabling the electromagnets. Examples of evaporation residue trajectories through TASCA are shown in Fig. 4.4 (bottom row). In this case, the first quadrupole focuses the particles in the horizontal direction, meaning that some of the particles which were deflected from the optimal path by the dipole magnet will be focused back again in the first quadrupole. This increases the transmission of evaporation residues, since only very few are lost in the walls of the quadrupole chambers. However, at the same time, the transmission of unwanted products to subsequent parts of TASCA increases. The second quadrupole focuses the beam in the vertical direction, and the overall effect of the quadrupoles produces a horizontally elongated beam spot at the focal plane of TASCA. The background in HTM was – until 2011 when significant improvements were made – larger than in SIM [86]. The good background suppression in SIM together with the small beam spot made SIM the obvious choice for the first experiments using the TASISpec setup.

4.4 TASISpec

Once the ions have been separated by TASCA, they are directed to the detector setup TASISpec. TASISpec is positioned at the very end of TASCA, as is shown in Fig. 4.4. The ions pass through a tube and are implanted into a Double-Sided Silicon Strip detector (DSSSD), which can

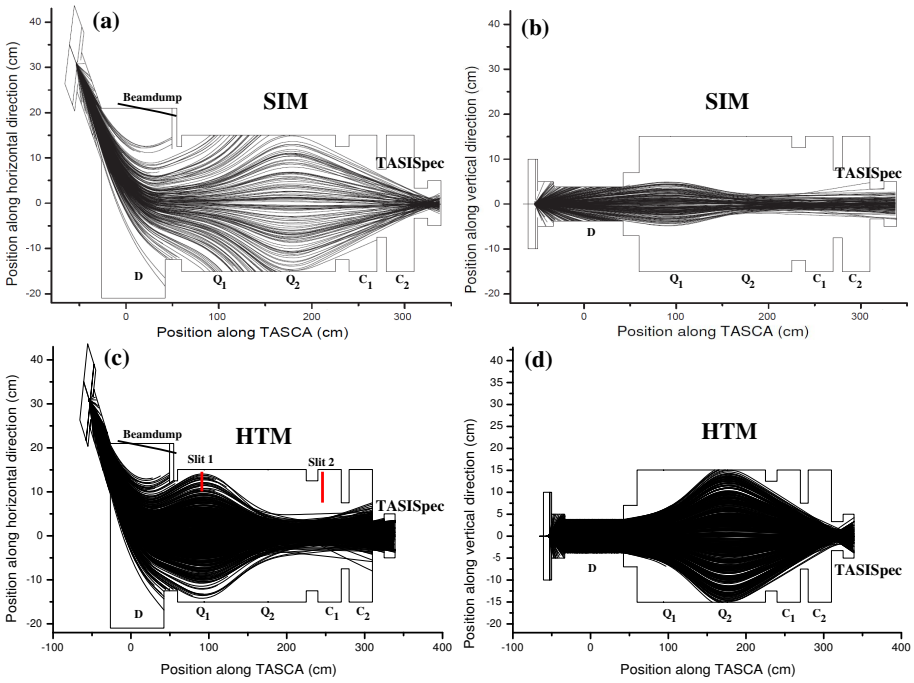

Figure 4.4: *Top and side views of simulated trajectories of evaporation residues in TASCA. The simulations are done for ^{254}No created in the reaction ^{48}Ca + ^{208}Pb. The particles enter TASCA through the pipe seen to the left in the figures. The dipole, two quadrupole chambers, two detector chambers and TASISpec follow. The outline of the dipole is strongly simplified – in reality, this magnet is rotated such that the ions enter it at a normal angle. (a) and (b) Trajectories in SIM. Simulation parameters have been optimised such that the best transmission to TASISpec is achieved. (c) and (d) Trajectories in HTM. Simulation parameters have been adjusted such that the simulation mimics the settings that proved to give the best experimental transmission to TASISpec.*

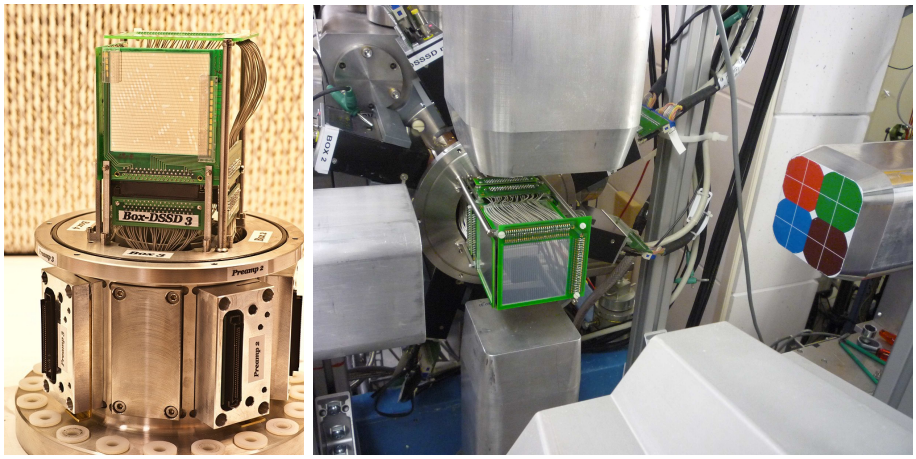

Figure 4.5: *(Left) The TASISpec silicon detector box. The entrance is directed downwards, where the ions enter through a tube. Preamplifiers are mounted around the lower part. The topmost detector is the implantation detector. Picture courtesy of Robert Hoischen. (Right) The TASISpec detector setup mounted at TASCA, seen from the opposite direction compared with the beam. The silicon detectors are seen in the middle of the figure, with the implantation detector towards the observer. In the lower part of the figure, closest to the observer, the CLUSTER detector is seen. The CLOVER detectors are on the four remaining sides of the silicon box. The picture was taken when the cap which usually covers the Si detectors was removed, and the Ge detectors were pulled back from their experiment positions.*

be seen in Fig. 4.5. The kinetic energy of superheavy elements is around 30 MeV which results in an implantation depth of about 7 μm. The charged decay products of the superheavy elements are detected in the implantation detector and in four additional silicon detectors (also called "box" detectors) positioned upstream of the implantation detector.

As part of my thesis work, the earlier version of TASISpec [35] was upgraded in two aspects during the spring of 2011. The tube through which the particles enter the detector array was widened from 5.0 cm to 6.6 cm in order to increase the transmission. Also, the upstream box detectors, which previously consisted of single-sided silicon strip detectors (SSSSDs), were replaced with DSSSDs. To incorporate these changes, also the holding structure was replaced.

The implantation DSSSD has 32 strips on the p-side and 32 strips on the n-side, an area of 6 $\times$ 6 cm^2 and a thickness of 0.52 mm. The four box detectors also have 32 p-side strips and 32 n-side strips but they are electrically connected such that they effectively act as 16 $\times$ 16 strip detectors. The thickness is 1.0 mm and the detector area is 6 $\times$ 6 cm^2. The p-sides of the detectors are directed towards the inside of the box. The p-side dead layers are equivalent to approximately 2.3 μm SiO_2. The n-side and p-side strips are perpendicular, creating a total of 1024 pixels for the implantation detector and 256 pixels for each of the box detectors. The total efficiency for α particles emitted from the implantation detector is 80(2)% [35].

To be able to study not only charged particles, but also γ and X rays, the TASISpec silicon detector array is surrounded by composite Ge detectors. A picture of the entire TASISpec setup is shown in the right part of Fig. 4.5. One CLUSTER Ge detector [88] positioned behind the implantation DSSSD and four CLOVER Ge detectors [89] positioned behind each box detector covers a very large solid angle. For the element 115 experiment, the setup was modified due to the lack of one CLOVER

detector. A second CLUSTER detector was used as a replacement.

The TASISpec photon detection efficiency has been established from measurements [35] and simulations [90]. The highest absolute efficiency of ∼40% is achieved at 100-150 keV, where K-X rays from superheavy elements are expected. The change in efficiency between the original Ge detector configuration and the one used for the element 115 experiment was small, but still incorporated into the simulations [90] used when interpreting the element 115 data.

For completeness, I would here like to mention also the possibility to use the TASCA Multi-Wire Proportional Counter (MWPC) [86] in conjunction with TASISpec. If the MWPC is used, the ions pass through two 0.25 μm-thick Mylar foils with isobuthane at a pressure of 4 mbar in between. Detection of a signal in the MWPC can be used to distinguish between decays from previously implanted atoms and new implantations. This considerably improves background conditions during beam-on periods. However, it was decided to not use the MWPC during the element 115 experiment, since in-beam tests (see Sec. 5.2) showed that it decreases the transmission to TASISpec by ∼40%.

4.5 Electronics

The TASISpec DSSSDs were connected to preamplifiers (for a detailed description, see Ref. [91]) mounted directly on the holding structure. Signals from the 96 n-side strips – 32 for the implantation detector and 16 for each of the four box detectors – were processed by analogue standard electronics [35] that record time and energy.

The 96 p-side strips were handled with digital electronics. This gives more information than just time and energy, and allows for, e.g., reconstruction of signals with pile-up. An almost dead-time free system, as well as superior noise reduction, can also be achieved thanks to digital electronics. A total of six digitising FEBEX modules [92], developed

at the Department of Experiment Electronics at GSI, were used. Each module has 16 channels. Incoming pulses were sampled at a rate of 60 MHz. The baseline was positioned in the middle of the accessible span of digitised values, and, hence, 11 of the 12 bits available for storing each digitised value set the limit for the precision. Each recorded pulse contained 4000 samples and covered $\sim$70 μs. Such recordings will be referred to as "traces". Since the entire pulse is stored in the trace, detailed information from the pulses can be carefully extracted offline. Examples of traces will be shown and further discussed in Sec. 6.

Signals from the 25 Ge crystals – four from each of the three CLOVER detectors, seven from the CLUSTER positioned behind the implantation DSSSD and six from the other CLUSTER which had one malfunctioning preamplifier – were processed by commercial 100 MHz 16-bit sampling ADCs SIS3302. Energy and timing information was extracted already in the modules. Also information on possible pile-up is included in the data stream.

The data was read out using the GSI Multi-Branch System (MBS). When data acquisition was triggered, data from all detectors (time, energy, pile-up information and traces) as well as information regarding beam status (on/off) and various detector rates were collected and stored as one event. Collection of all data in a single event makes offline data handling easier. Files containing the events were stored in the GSI archive storage system, which consists of a tape robot.

During experimental conditions the data acquisition was triggered by a coincident signal from a p-side and an n-side strip. For calibrations, other types of triggers were used as well.

To improve background conditions, a beam-shutoff function was implemented. When a potential α particle from element 115 ($\sim$10 MeV) was detected in the n-side of the implantation detector within a certain time after a possible implantation of an element 115 ion, a signal was sent

to the UNILAC beam control system and the beam was stopped within 20 μs. The beam was then off for a number of seconds. If a second potential α decay was detected within this period, the beam-off time was prolonged. During the experiment different beam-shutoff lengths were employed.

4.6 TASCA simulations

To simulate the trajectories of various particles inside TASCA, two C++ programs, `TRIMIN` and `TSIM` [93, 94], originally written for the Berkeley gas-filled separator but re-written for TASCA [86, 95], together with `SRIM2008` [70], were used. `TRIMIN` produces a file containing the characteristics of the produced superheavy elements, `SRIM` is used for propagating these in the target, and `TSIM` simulates the behaviour of the ions in TASCA.

`TRIMIN`

The first part of the simulation creates a distribution of evaporation residues. The energy and angle of every simulated beam particle is randomly chosen from Gaussian distributions based on experimental parameters for the beam. The energy loss in the target backing, and in the target itself, is calculated for each ion. Due to uncertainties in the thicknesses of the target and the backing, the thicknesses used for each ion are also chosen from Gaussian distributions. The stopping power $\frac{dE}{dx}$ in the backing and target materials needs to be estimated. Linear interpolations of $\frac{dE}{dx}(E)$ are made by estimating the energy E in the beginning and end of the backing and target, respectively. The respective $\frac{dE}{dx}(E)$ is obtained from `SRIM2008`. The excitation function (cross section as function of excitation energy), from either theoretical models or previous measurements, is approximated to be Gaussian. A random

excitation energy is selected for each ion. If the ion reaches a kinetic energy corresponding to this excitation energy at some point in the target, the position is recorded and a compound nucleus is assumed to be created at that point. The energy and angle of the evaporation residues is simulated, and a correction for isotropic evaporation of a variable number of neutrons with kinetic energies of 2 MeV is made. The procedure is repeated until the number of created evaporation residues reaches a pre-determined value.

`TRIMIN` outputs the energies, angles and target depths of the created evaporation residues. The total number of attempts to create evaporation residues can be used to estimate absolute efficiencies. In the cases where the target material is not available in `SRIM2008`, which handles elements up to uranium only, extrapolations from lighter hypothetical isobars, with the same density as the desired material, have to be made.

`SRIM`

Starting from the energies, angles and positions from `TRIMIN`, the evaporation residues are propagated through the remaining target material using SRIM [70]. In the cases when the target material or the produced evaporation residue is heavier than uranium (the heaviest element that can be used in SRIM) the uranium isobar of the heavy element was used instead. Since the thickness of the target varied with each ion, the positions of the evaporation residues are given as the distance to the end of the target. Any additional material that comes after the target, such as the thin layers of carbon that cover some of the targets, can be added in SRIM. After the simulation, SRIM outputs position, angle and energy of each of the evaporation residues after the target and any additional material. While the particles move through the target, the movement in the horizontal or vertical direction is most often of the order of only 1 μm.

TSIM

TSIM uses the distribution of evaporation residues after the target, and calculates their trajectories inside TASCA. Two types of interactions occur during their flight – interactions with the low-pressure gas such as scattering, charge exchange, and energy loss, and interactions with the magnetic fields. The magnetic field is included in the form of one field map for HTM and one for SIM [95]. The field maps were obtained using the simulation program KOMPOT [78, 96]. Values for $B\rho$ are tested until the evaporation residues are centred in the detector. The corresponding current to be used in the dipole is found by Eq. B.1. In the simulation, the effect of various quadrupole currents can be implemented by scaling factors defined in Appendix C.

In each step of the simulation, the length which the particle travels before it interacts with a particle in the gas is randomly chosen from certain distributions. These depend on properties of the particles, such as the current and average charge state, and the gas. Whichever of the charge exchange length and the scattering length is shorter is chosen, and the particle is propagated this far. In case of charge exchange, the charge of the ion is changed accordingly. In case of scattering, the angle and energy of the ion is changed. If both these lengths are more than 1 cm, the ion is simply propagated 1 cm. The average charge state is calculated from Eq. 4.4.

During the propagation, the magnetic forces are included. Finally, the energy loss, governed by the Bethe Bloch formula, during the motion is calculated and subtracted. Each particle is propagated in this way until it either collides with a wall or reaches the detector.

TSIM also includes the spatial distribution of the beam, which until now has been ignored. The incoming particles are assumed to be spread out evenly over a circle with 5 mm in diameter. The size was judged reasonable from looking at the beam profile on the beam-current grids

placed upstream of the target.

`TSIM` can simulate ion transport through TASCA in both HTM and SIM. Although the respective field map contains both the dipole and the two quadrupole fields, the three fields can be modified separately. Other adjustable parameters are the gas composition and pressure, and the detector geometry.

`TSIM` outputs the trajectory of each particle, along with a simplified outline of TASCA. Examples of simulated trajectories have already been shown in Fig. 4.4. `TSIM` also outputs the characteristics, such as position and energy, of each particle that reaches the detector.

4.7 TASISpec simulations

The TASISpec setup exists also in virtual `Geant4` space. `Geant4` [71, 72] is a diverse simulation toolkit in which, for instance, the interaction of particles with matter can be simulated. It can be used for various tasks, such as optimisation of detectors and for data analysis. We have used simulations to evaluate how TASISpec responds to the presence of particles with a given decay pattern. Level schemes for decaying nuclei constitute one of the input parameters, and can be varied until agreement with data occurs. The detailed geometry of TASISpec has been implemented by L. G. Sarmiento [90]. The constituents of the virtual TASISpec are shown in Fig. 4.6. `Geant4` does not yet support elements with $Z > 100$, but the techniques described in Ref. [58] made it possible to perform detailed and profound simulations also for implantation and decay of superheavy elements. A full implementation of elements with $Z > 100$ into `Geant4` is currently under way [97].

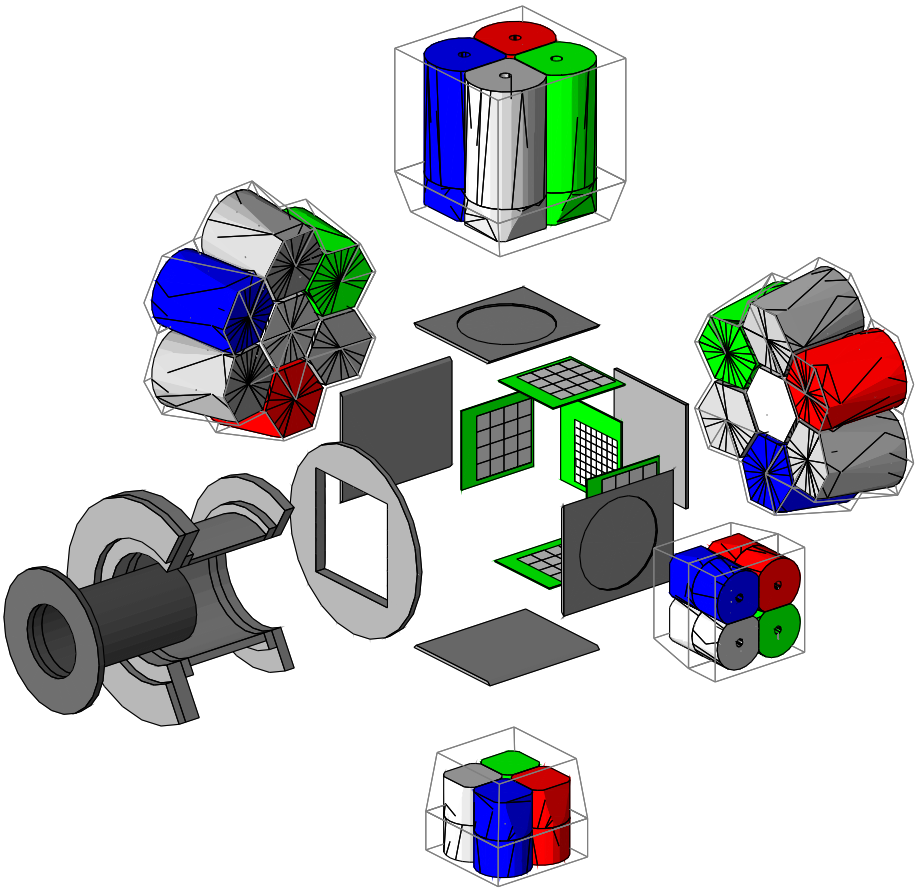

Figure 4.6: *TASISpec in* `Geant4` *space. The different parts of TASISpec are separated from each other. The figure shows the parts from the setup during the element 115 experiment, where one CLOVER detector was replaced by a CLUSTER detector. The pixelation of the DSSSDs was reduced by a factor of four for visualisation purposes. Courtesy of L.G. Sarmiento.*

5

Experimental settings

When performing an experiment using the setup described in the previous chapter, various settings have to be decided upon. Two of the most important ones concern the beam energy and the TASCA settings. In this chapter, I will describe how these choices were made for the element 115 experiment using the data available at that time.

5.1 Beam energy

Choosing a suitable beam energy requires knowledge of the energy loss in the target and the variation with energy of the cross section for the reaction. The beam particles lose energy continuously as they traverse the backing and the target layer. The energy loss in the target is several MeV. Therefore, the beam energy is often chosen such that the optimal energy of the beam particles occurs in the centre of the target layer. The situation and the notation is illustrated in Fig. 5.1. Sometimes, the excitation energy, E^*, of the compound nucleus is given instead of the beam energy. To transform between them, the formulas in Appendix A can be used.

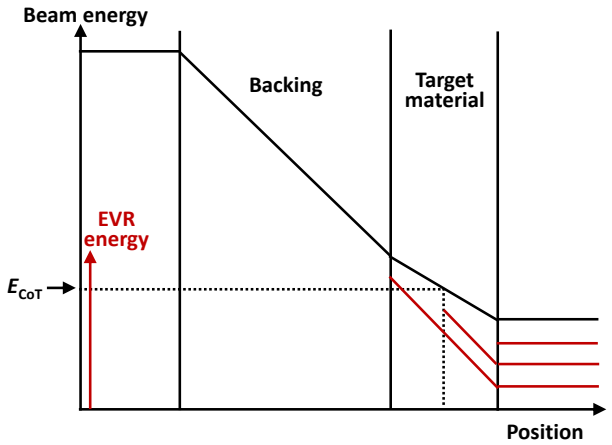

Figure 5.1: *Schematic illustration of the backing and target layer. The decrease of the beam energy is indicated in black. In red, the kinetic energy of evaporation residues (EVRs) created in the beginning, centre, and end, of the target are sketched. The energies are not to scale, neither absolutely nor relatively.*

The optimal beam energy is either known from previous experiments, or it has to be predicted with the help of theoretical models. One related difficulty is the calculation of the Q-value (energy release) for the nuclear reaction between beam and target nuclei, since the mass for $^{291}115$ is simply not experimentally known. Hence, theoretical predictions – or extrapolations – have to be used. Often, the tabulated masses are given as "mass excesses", i.e. the energy discrepancy compared to A atomic mass units. The mass excesses are -44.214 MeV for ^{48}Ca, 57.176 MeV for ^{243}Am and, for example, 181.070 MeV or 180.02 MeV for $^{291}115$. The first three numbers originate from Ref. [98] and the last value is from Ref. [99]. These values yield, by using Eq. A.3, $Q = -168.108$ MeV and $Q = -167.058$ MeV for the fusion reaction between ^{48}Ca and ^{243}Am, respectively. Allegedly, the mass table used to transform between beam energy and excitation energy in Refs. [16, 48] is the one from Myers-Swiatecki [99].

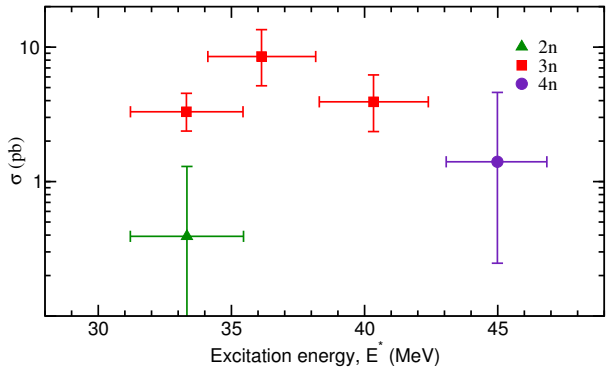

Figure 5.2: *Measured cross sections for chains assigned to the isotopes $^{287,288,289}115$ created in the reaction ^{48}Ca on ^{243}Am as a function of excitation energy of the compound nucleus. Data points are taken from Ref. [48]. See text for more details.*

To select a suitable excitation energy, we used the published data available at the time, consisting of theoretical calculations [16] and decay chains measured at JINR, Dubna, Russia [3, 48]. According to the calculations by Zagrebaev [16], the cross section for the $3n$ fusion-evaporation reaction (when three neutrons are evaporated from the compound nucleus) peaks at 40 MeV excitation energy, and the $4n$ channel peaks at 41.7 MeV, i.e. 1.7 MeV above. Experimental results published in 2004 [3], determined the cross section at 40 MeV excitation energy (using the mass table from Ref. [99]) to be around 3 pb for the $3n$ channel, and around 1 pb for the $4n$ channel at 44 MeV. A subsequent experiment, in which many more element 115 atoms were produced, provided a more thorough investigation of the cross section for the $3n$ reaction [48]. The highest cross section for the $3n$ channel was measured to be 9 pb at the excitation energy 36.2 MeV, see Fig. 5.2. Assuming that this is the maximal cross section, the measured excitation function for the $3n$ channel seems to peak at approximately $\sim$ 4 MeV below the original predictions by Zagrebaev [16].

Originally, we were mainly interested in the odd-even nucleus $^{287}115$, produced in the $4n$ reaction. A plausible guess for the energy of the cross section maximum can be made by assuming that the relative peak positions from Zagrebaev's calculations are correct, but with the absolute position being shifted downwards such that the $3n$ channel prediction coincides with measurements. This implies that our best chances to produce $^{287}115$ should be at an excitation energy of 36.2 MeV+1.7 MeV = 37.9 MeV. Transforming this to a beam energy using Eq. A.2 and $Q = -167.1$ MeV yields the centre of target energy $E_{CoT} = 245.4$ MeV.

To maximize the production of the selected isotope throughout the target, the beam particles should reach the optimal energy in the centre of the target. As an example on how to find the beam energy, we start with the $E_{CoT} = 245.4$ MeV that maximises the $4n$ channel. First, we calculate how much energy is lost in the target layer. This is complicated by the fact that the stopping power for ^{48}Ca in Am_2O_3 is unknown. We make a first estimate by assuming it to be constant over target, and the same as for 10.57 g/cm^3 $^{243}U_2O_3$ ($dE/dx \sim 8$ MeV/(mg/cm^2) at $E_{CoT} =$ 245.4 MeV). The energy in the beginning (end) of a 0.75 mg/cm^2 target is then approximately 248.4 (242.4) MeV. For comparison, the stopping powers at these energies were calculated for oxides of lighter elements using `SRIM`, all at a density of 10.57 g/cm^3 and the mass number 243. The results are shown in Table 5.1. As the trend in the data is not obvious, values slightly above the ones for $^{243}U_2O_3$ were selected for $^{243}Am_2O_3$. We use the average of the end-point values, yielding 8.03 MeV/(mg/cm^2).

Focussing on target wheel 1 (~ 0.83 mg/cm^2 on average) the calculation can be slightly refined. Assuming a constant stopping power of 8.03 MeV/(mg/cm^2) the beam energy range in the target is 248.7-242.1 MeV. The energy loss in the backing material can now be calculated. The stopping power for ^{48}Ca in Ti is 13.77 MeV/(mg/cm^2) at 248.7 MeV, which

Table 5.1: *The stopping power, dE/dx, in MeV/(mg/cm^2) for various oxides at two different energies, and the extrapolation to $^{243}Am_2O_3$.*

Material	$\frac{dE}{dx}$ at 248.4 MeV	$\frac{dE}{dx}$ at 242.4 MeV
$^{243}Hg_2O_3$	7.13	7.19
$^{243}Bi_2O_3$	7.29	7.35
$^{243}Po_2O_3$	7.36	7.42
$^{243}At_2O_3$	7.78	7.83
$^{243}Rn_2O_3$	7.74	7.79
$^{243}Fr_2O_3$	7.73	7.79
$^{243}Ra_2O_3$	7.67	7.73
$^{243}Ac_2O_3$	7.75	7.81
$^{243}Th_2O_3$	7.80	7.86
$^{243}Pa_2O_3$	7.79	7.85
$^{243}U_2O_3$	7.95	8.01
$^{243}Am_2O_3$, extrapolated	8.00	8.06

by calculating backwards implies the beam energy to be approximately 262.3 MeV at the beginning of the backing. At this energy, the stopping power is 13.49 MeV/(mg/cm^2), i.e. slightly lower than at the end of the backing. By using an average of the stopping power in the beginning and end of the target, the optimized beam energy is E = 262.2 MeV. Since the mass of ^{48}Ca is 47.953 u, this translates into a beam energy of 5.468 MeV/u.

During the element 115 experiment, we decided to use a beam energy that, in the centre of target, was between the peak for the $3n$ and the $4n$ reaction channel. Our main aim was to maximise the production of the $3n$ channel, but the relatively thick targets could cover both the maximum of the $4n$ and the $3n$ channels, giving us possibilities of observing both. It was decided to use a beam energy such that E_{CoT} = 245.0 MeV (E = 5.462 MeV/u). The energy of the beam in the target was E_t = 248.3-241.7 MeV. This leads to excitation energies E^*= 34.8-40.3 MeV, using Eq. A.2 and the mass table in Ref. [99]. For the second part of

the experiment, the beam energy was decreased to 5.400 MeV/u, i.e. E_{CoT} = 242.1 MeV and excitation energies in the interval E^*= 32.4-37.9 MeV. The intention was to increase the probabilities for producing the isotope $^{289}115$ created in the $2n$ channel.

5.2 Selection of TASCA mode – SIM or HTM?

The two TASCA focussing modes, Small Image Mode (SIM) and High Transmission Mode (HTM), have different advantages. For a large implantation detector positioned in the focal plane, the transmission in HTM can be up to 60%. SIM gives a more focussed beam spot but a lower transmission to the focal plane of about 35-40%. The small TASISpec implantation detector of 6 × 6 cm^2, together with the positioning after the focal plane, made SIM the obvious choice. Due to the small beam spot in SIM, the transmission to the TASISpec implantation detector can be the same as to the focal plane detector. Also, the background reduction is SIM was better than in HTM. During TASISpec commissioning [35] SIM was used successfully.

During 2010 and 2011, simulations and experiments [100] showed that background reduction in HTM could be improved significantly by inserting "slits" (plates thick enough to stop beam particles) inside TASCA at strategic positions. This suggested, contrary to previous experience, that HTM could perform even better than SIM in terms of background suppression, implying that HTM can be beneficial for TASISpec measurements. The transmission would have to be optimised, however, since the large beam spot in HTM causes large losses around the TASISpec entrance tube.

In June 2011 we performed transmission tests in both SIM and HTM using the well-known reaction ^{208}Pb(^{48}Ca,$2n$)^{254}No which has a maximal cross section of around 1 μb. Simulations using `TRIMIN`, `SRIM2008` and `TSIM` were made to guide the search for the optimal quadrupole settings,

and to understand the experimental transmissions. For HTM, the idea was to decrease the "standard" focusing such that the focal plane is moved closer to TASISpec. Ideally, the beam spot should be as small as possible while traversing the TASISpec entrance tube.

The tests were performed with a target of 0.760 mg/cm^2 ^{208}PbS and a beam of ^{48}Ca at 220.1 MeV. The target had been evaporated onto a carbon backing with a thickness of on average 41 μg/cm^2, with the backing facing the beam. To decrease sputtering losses, a thin layer of carbon ($\sim$10 μg/cm^2) was evaporated onto the target layer. A carbon stripper foil (55 μg/cm^2) was positioned upstream of the target to increase the charge state and thus increase the deflection of the primary beam in the TASCA dipole.

In the simulations, the carbon stripper foil was included in `TRIMIN` by increasing the thickness of the backing to 95 μg/cm^2. This ignores the spatial spread which occurs between the stripper foil and the target backing. dE/dx for the beam ions in the beginning and end of the backing and target, respectively, were evaluated using SRIM. The `TRIMIN` parameters are given in Table 5.2.

The parameters used in the next step of the calculation, using `SRIM2008`, are given in Table 5.3. Since ^{254}No is heavier than uranium, the corresponding isobar ^{254}U is used instead. The error made in this approximation was investigated by making the `SRIM2008` calculation with various ions; ^{254}Pb, ^{254}Po, ^{254}Rn, ^{254}Ra, ^{254}Th, ^{254}U, all with the density 7.6 g/cm^2. The difference in the ion energy after the target was negligible.

The results of the `TSIM` simulations were first used to estimate the optimal $B\rho$ that focuses the evaporation residues towards the centre of the implantation detector. For simulations in Small Image Mode (SIM), TASCA was filled with 0.3 mbar He, and in High Transmission Mode (HTM) with 0.8 mbar He. It was found that the created ^{254}No ions

Table 5.2: *Parameters used in* `TRIMIN` *to simulate the experiment done in June 2011. The cross section parameters are from Ref. [86].*

Parameter	Value
Beam energy σ	0.440 MeV (up to 2σ considered)
Beam angular σ	0.90° (up to 4σ considered)
Backing σ	10% (up to 2σ considered)
Target σ	10% (up to 2σ considered)
Backing material	^{12}C
Target material	^{208}PbS
Stripper+backing thickness	0.095 mg/cm^2
Target thickness	0.760 mg/cm^2
Beam energy	220.1 MeV
Beam ion	^{48}Ca
Density, stripper + backing	2.253 g/cm^3
Density, target	7.6 g/cm^3
$\frac{dE}{dx}$, ^{nat}C at 219.6 MeV	20.25 MeV/(mg/cm^2)
$\frac{dE}{dx}$, ^{nat}C at 217.6 MeV	20.33 MeV/(mg/cm^2)
$\frac{dE}{dx}$, ^{208}PbS at 217.6 MeV	8.76 MeV/(mg/cm^2)
$\frac{dE}{dx}$, ^{208}PbS at 214.0 MeV	8.80 MeV/(mg/cm^2)
Beam energy at max. cross sec.	216.2 MeV
σ of cross section distribution	2.9 MeV (up to 4σ considered)
Number of evaporated neutrons	2

Table 5.3: *Parameters used in SRIM.*

Parameter	Value
Incoming particle	^{254}U
Layer 1, material	^{208}PbS
Layer 1, thickness	12001 Å
Layer 1, density	7.6 g/cm^3
Layer 2, material	^{nat}C
Layer 2, thickness	444 Å
Layer 2, density	2.253 g/cm^3

should have an average $B\rho$ = 2.10 Tm. Then, the magnetic fields in the quadrupole magnets were optimised with respect to the transmission to TASISpec. The optimisations were guided by the transmission itself, the trajectories inside TASCA, and the spatial distribution over the implantation detector. Also previously tested experimental settings were simulated. After the experiments, the experimentally best settings were simulated as well, to assess the quality of the simulations. The simulated magnetic fields can be translated into the currents I_D, I_{Q_1} and I_{Q_2} through the dipole magnet (D) and the two quadrupole magnets (Q_1 and Q_2) using the equations in Appendix C.

5.2.1 Small Image Mode (SIM)

Experiments performed in the spring of 2010 showed that the optimal SIM setting for the reaction ^{206,207}Pb(^{48}Ca,$2n$)^{252,253}No were I_D = 610 A, I_{Q_1} = 395 A, and I_{Q_2} = 480 A, for a target thickness of ∼0.4 mg/cm^2 PbS and a beam energy of E_{CoT} = 215.8 MeV. The same SIM settings were assumed to be optimal also for the currently described experiment, since the two experiments where similar.

These previous best settings were confirmed, as no other settings were statistically significantly better. The transmission was deduced from the number of α particles in the energy region 8.05-8.15 MeV in the summed energy spectrum from all 32 p-side strips of the implantation detector during beam-off periods. Such an energy spectrum is shown in Fig. 5.3 (a). Figure 5.3 (b) shows the beam-on data. The number of α-particles, N_α, was normalized to the beam integral, measured by an induction coil in a non-destructive way [86]. N_α for the tested settings are shown in Table 5.4. Two different measurements were done at the previously optimized settings, and they are displayed both separately in the table and as the sum “14+21”.

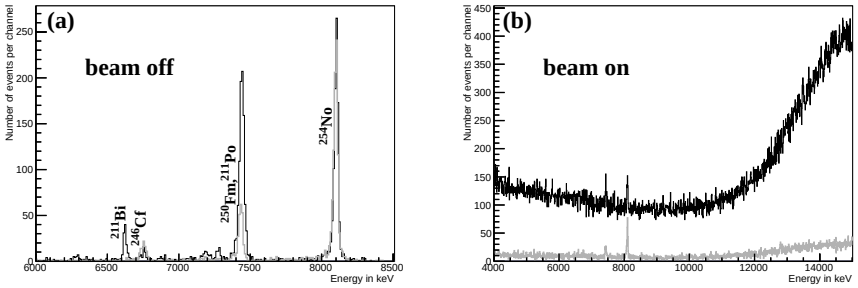

Figure 5.3: *Summed energy spectra from the p-side strips from SIM (black) and HTM (grey). (a) beam-off spectra. (b) beam-on spectra. The data is normalized to the number of counts in the peak from ^{254}No in the beam-off spectra. The largest peak in the beam-off spectra is from the α decay of ^{254}No, while the others are from the daughter ^{250}Fm and grand daughter ^{246}Cf, and the transfer reaction products ^{211}Bi and ^{211}Po.*

Table 5.4: *Relative transmission for all the measurements performed with TASISpec and TASCA in SIM. All measurements were performed at a gas pressure of 0.3 mbar He. Simulations marked with K relate to work done by J. Khuyagbaatar, and those marked with F relate to work done by me. "Online" refers to that the analysis during the spring 2010 experiment suggested that this was the optimal settings, while a more careful "offline" analysis revealed a slight preference for another setting. Currents in A.*

File	I_D	I_{Q_1}	I_{Q_2}	N_α	Description
14	610	395	480	427 ± 10	Previous best setting (online)
17	610	443	512	390 ± 9	Suggested by simulations (K)
18	594	443	512	389 ± 9	Suggested by simulations (K)
19	610	463	506	367 ± 9	Suggested by simulations (F)
20	610	400	470	442 ± 15	Previous best setting (offline)
21	610	395	480	432 ± 14	Previous best setting (online)
14+21	610	395	480	428 ± 8	Previous best setting (online)
22	610	395	480	254 ± 8	With MWPC mounted

To simulate the trajectories for the experimentally best magnet settings, the `TSIM` scaling factors were calculated according to Eq. C.1. Figure 5.4(b) shows the simulated hitpattern on the TASISpec implantation detector. Figure 5.4(a) shows the experimental hitpattern, gated on energies corresponding to the α decay of ^{254}No. The large discrepancies imply that the simulations in SIM are not accurate.

Simulations by both J. Khuyagbaatar and me suggested that the two quadrupole fields should be both stronger and more similar to minimise the losses above and below the TASISpec entrance tube. Trajectories from the best simulations are shown in the upper part of Fig. 4.4, and the distribution over the implantation detector is shown in Fig. 5.4(c). Although the measured transmission to TASISpec was poor for the settings suggested by simulations, it is interesting to note that the hitpatterns in Figs. 5.4(a) and (c) are very similar – simulations and experiment agree on the optimal shape of the beam spot even if they do not agree on what magnet settings will produce it.

Figure 5.4(d) shows the experimental hitpattern from the last measurement presented in Table 5.4. During this measurement, the MWPC, which is often used in conjunction with measurements with the TASCA focal-plane detector to discriminate incoming particles from implanted radioactivity, was inserted. The detector was placed as close as possible to the TASISpec entrance tube. As seen in the hitpattern, the MWPC causes scattering of the otherwise very focused beam spot. This reduced the transmission to the detector by ∼40%. Even if the MWPC could be used to better access data from beam-on periods (as is usually not possible in SIM), this 33% increase of data would not compensate for the loss of particles. Hence, the MWPC was deemed unsuitable for use in conjunction with TASISpec and TASCA in SIM.

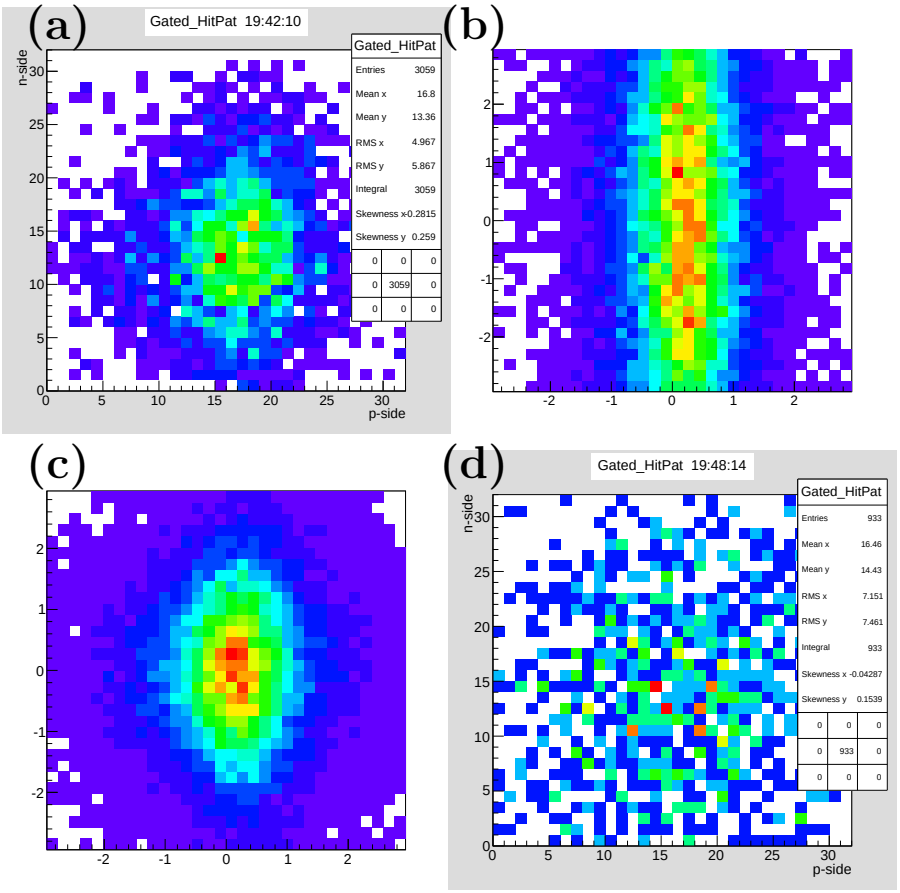

Figure 5.4: *The beam spot on the TASISpec implantation detector as seen with the beam direction. (a) the experimental distribution from the settings which proved to have optimal transmission, (b) the simulated distribution of these settings, (c) the distribution arising from the magnet settings that gave the best transmission according to the simulation, (d) the experimental distribution from the experimentally verified best settings but with the MWPC installed. For the experimental hitpatterns, the axes represent the p-side and n-side strips. For the simulated hitpatterns, the axes represent the distance from the centre in cm.*

5.2.2 High Transmission Mode (HTM)

To investigate the possibilities of using TASISpec in conjunction with HTM, a set of measurements aiming to examining the background reduction was done [100]. The TASCA focal-plane detector was used. Two slits were inserted into TASCA as described in Ref. [100]. The tests showed a strong background suppression already when the first slit (in the first quadrupole, see Fig. 4.4), was inserted. By adding another slit just after the second quadrupole, the background was reduced even further.

Next, the transmission into TASISpec was investigated. When measurements are made with the large and rectangular focal-plane detector, the currents in the two quadrupoles are the same. This gives a beam spot that is elongated in the horizontal direction. For focussing to the smaller and symmetric TASISpec implantation detector setup, a relatively stronger focussing in the horizontal direction seems favourable. Simulations made by both J. Khuyagbaatar and me suggested such adjustments of the magnet settings. In Fig. 4.4 (bottom) simulated trajectories are shown. The simulation is made for the experimentally established best settings, but these are very similar to the ones suggested by the simulations. Some particles are lost on the right and left hand side of the TASISpec entrance tube, but these losses are reduced by the relatively stronger horizontal focussing.

Table 5.5 shows the experimental transmission for various settings. The magnet settings given in the second and third entry were suggested by simulations. Guided by the implantation detector hitpatterns from the three first measurements, a somewhat better setting was found by varying the quadrupole currents slightly, to $I_{Q_1} = 525$ A, and $I_{Q_2} = 510$ A. These settings were within the range originally suggested by my simulations. This confirms that the simulation programs can be used to describe trajectories in HTM. Other variations of magnet settings did not improve the transmission further.

Table 5.5: *Relative transmission to TASISpec for all the measurements performed with TASCA in HTM. Simulations marked with K relate to work done by J. Khuyagbaatar, and those marked with F relate to work done by me. Currents in A.*

File	I_D	I_{Q_1}	I_{Q_2}	N_α	Description
39	603	543	543	295 ± 9	Same as in FPD slit test
40	603	550	530	280 ± 9	Suggested by simulations (K)
41	603	515	494	325 ± 9	Suggested by simulations (F)
46	603	525	510	339 ± 12	Variation 1
47	603	515	485	303 ± 12	Variation 2
48	603	525	502	323 ± 12	Variation 3
49	603	535	510	313 ± 11	Variation 4
50	603	515	510	277 ± 16	Variation 5
51	603	505	484	291 ± 13	Variation 6
54	603	525	510	208 ± 10	MWPC mounted

The very last entry in Table 5.5 shows the effect of inserting the MWPC into TASCA. As in the SIM case, the transmission was reduced by ∼40%, which is not compensated for by the possibility to better access the beam-on data. Therefore, the MWPC was deemed unsuitable for use together with TASISpec in HTM as well.

However, with the improved background reduction in HTM, it is possible to access the beam-on data even without using the MWPC. The better background reduction in HTM compared to the one obtained in SIM is seen in Fig. 5.3. During the beam-on periods (right panel), the total amount of impinging particles is much smaller in HTM than in SIM. The peaks from ^{254}No and its daughter and grand daughter are clearly visible on top of only a small background. During beam-off periods the effect can be seen as well, especially in the peak at ∼7.4 MeV. In the clean HTM spectrum, this peak consists almost exclusively of α decays of ^{250}Fm (7.43 MeV), while in the SIM spectrum, the peak is significantly larger due to a contribution from the contaminating transfer

reaction product ^{211}Po (7.45 MeV). There are also other peaks from transfer reaction products present in the SIM spectrum but absent in the HTM spectrum.

The transmission to TASISpec in HTM is ∼80% of the one in SIM (see Table 5.4 and Table 5.5). Access to beam-on periods increases the data with 33%. The overall change in available data when HTM is used is therefore $1.33 \cdot 0.8 \gtrsim 1.0$, i.e. comparable to the one in SIM. However, the superior background suppression in HTM improves the beam-off data. Additionally, the use of beam-on periods allows for spectroscopy of short-lived isotopes and isomers. Therefore, HTM is the revised preferred TASCA mode for TASISpec measurements.

5.3 Magnet settings for element 115 experiment

In the first section in this chapter, suitable beam energies for production of the isotopes ^{287,288,289}115 were determined. Now, the question is which $B\rho$ TASCA should be tuned to. One way to determine the $B\rho$ is to use Eq. 4.4 and Eq. 4.1, and another way is to use the set of simulation programs. In either case, the correction factor of 1.055 needs to be added. The advantage of using the simulation programs is that more details, such as the energy loss in the gas and the different thicknesses for different target segments, are taken into account. The main uncertainties in either method are unknown stopping powers in the target, unknown excitation functions, and uncertainties in the target segment thicknesses.

An approximation of the $B\rho$ for the originally planned 262.2 MeV beam energy using Eq. 4.4 and Eq. 4.1 will be presented first. The kinetic energies of the produced compound nuclei are, according to Eq. A.1, 41.0 MeV and 39.9 MeV when they are produced in the beginning and end of the target layer, respectively. For now, the evaporation of neutrons is ignored. The compound nuclei created in the beginning of the target lose several MeV before emerging. To approximate the stopping power

Table 5.6: *The stopping power in MeV/(mg/cm^2) of various projectiles with $A = 287$ in $^{243}U_2O_3$.*

Projectile	$\frac{dE}{dx}$ at 41.0 MeV	$\frac{dE}{dx}$ at 32.3 MeV
Fr	10.56	9.28
Ra	10.80	9.48
Ac	10.56	9.26
Th	10.55	9.25
Pa	10.83	9.54
U	10.39	9.32
"115"	10.50	9.20

of element 115 in $^{243}Am_2O_3$, an "extrapolation" from isobars available in SRIM traversing $^{243}U_2O_3$ is made, see Table 5.6. The stopping power for $^{287}115$ at 41.0 MeV was taken to be 10.5 MeV/(mg/cm^2). Assuming a constant stopping power, the energy after the target is 32.3 MeV. Checking the stopping power at this energy and taking the average between the beginning and end of the target, the energy was refined to 32.8 MeV. Hence, the kinetic energy of the compound nuclei at the end of the target is 32.8 - 39.9 MeV, depending on where they were created. Now, the evaporation of neutrons is considered. Assuming four neutrons being evaporated isotropically from the compound nucleus, the energies of evaporation residues are spread out considerably. However, the distribution should still be centred around the average 36.5 MeV. The velocity of ions at this energy is around $4.9{\cdot}10^6$ m/s, and the average charge is $\bar{q} = 6.9$ according to Eq. 4.4. This gives the prediction $B\rho = 2.11$ Tm. Adding the final correction yields $2.11\ \text{Tm} \cdot 1.055 = 2.23$ Tm.

The reaction was also simulated. The parameters used in `TRIMIN` and in SRIM are presented in Tables 5.7 and 5.8, respectively. The use of target wheel 1 was assumed. In `TSIM`, the use of HTM, scaling factors from the experimentally optimised quadrupole currents, and a gas pressure of 0.8 mbar He were assumed. The best transmission was

achieved for $B\rho = 2.115$ Tm. Applying the final correction leads to $B\rho = 2.23$ Tm. The corresponding dipole and quadrupole currents I_D, I_{Q_1}, and I_{Q_2} are obtained using Appendix B.

Simulations for target wheel 2 showed only a minimal difference (245.4 MeV vs 245.3 MeV) of the average centre-of-target energy when the same beam energy was used. This implies that there is no need to consider a change of beam energy or of magnet settings if the target would have to be exchanged during the experiment. In case the experiment should be optimized for production of $^{288}115$ instead, the beam energy should be adjusted to 260.6 (260.3) MeV for target wheel 1 (target wheel 2), while the magnet settings stay the same. For the beam energies used during the experiment (261.9 MeV and 259.0 MeV), the predicted differences in velocities of element 115 atoms are very small, and there is no reason to expect that the magnet settings should be changed due to changes in $B\rho$. When the experiment was started, $B\rho = 2.23$ Tm was used. As the position of the detected element 115 atoms seemed slightly displaced, we also tried 2.19 Tm and finally settled for 2.21 Tm. Corresponding changes in the quadrupole currents were made.

Table 5.7: *Summary of parameters used in* `TRIMIN` *when simulating the element 115 experiment.*

Parameter	Value
Beam energy σ	0.52 MeV (up to 2σ considered)
Beam angular σ	0.90° (up to 4σ considered)
Backing σ	10% (up to 2σ considered)
Target σ	10% (up to 2σ considered)
Backing material	^{nat}Ti
Target material	^{243}Am
Backing segment thicknesses	see Table 4.1
Target segment thicknesses	see Table 4.2
Beam energy	262.2 MeV
Beam ion	^{48}Ca
Density, backing	4.519 g/cm^3
Density, target	10.57 g/cm^3
$\frac{dE}{dx}$, ^{nat}Ti at 262.3 MeV	13.77 MeV/(mg/cm^2)
$\frac{dE}{dx}$, ^{nat}Ti at 248.7 MeV	13.49 MeV/(mg/cm^2)
$\frac{dE}{dx}$, ^{243}Am at 248.4 MeV	8.00 MeV/(mg/cm^2)
$\frac{dE}{dx}$, ^{243}Am at 242.4 MeV	8.06 MeV/(mg/cm^2)
Beam energy at max. cross section	245.4 MeV
σ of cross section distribution	3 MeV (up to 4σ considered)
Number of evaporated neutrons	4

Table 5.8: *Parameters used in SRIM when simulating the element 115 experiment.*

Parameter	Value
Incoming particle	^{287}U
Target, material	$^{243}U_2O_3$
Target, thickness	9868 Å
Target, density	10.57 g/cm^3

6

Data analysis

The data from the element 115 experiment was analysed offline using the GO4 data analysis framework [101] and codes written in C. While the analog data from the n-sides of the DSSSDs consisted of energies and timing information, the digitised data from the p-sides consisted of pulse shapes. The analysis was done in two steps. First, information from the digital traces was extracted and written to files in ASCII format. These files were read by a C program, in which the main part of the analysis – summing of energies in neighbouring strips, calibrations, recalibrations, and correlation analysis – was done. To be able to perform reconstructions of particles that escape the implantation detector, a careful determination of the detector dead layer thicknesses was made using `SRIM` [70], `ROOT` [102], and `Geant4` [71, 72] simulations using the virtually constructed TASISpec [58, 90].

6.1 Data from traces

The p-side strips in the TASISpec silicon detectors were read out using FEBEX modules [92] using 12-bit sampling at a rate of 60 MHz, i.e. $\sim$ 17 ns per channel. The recorded pulses – "traces" – were analysed

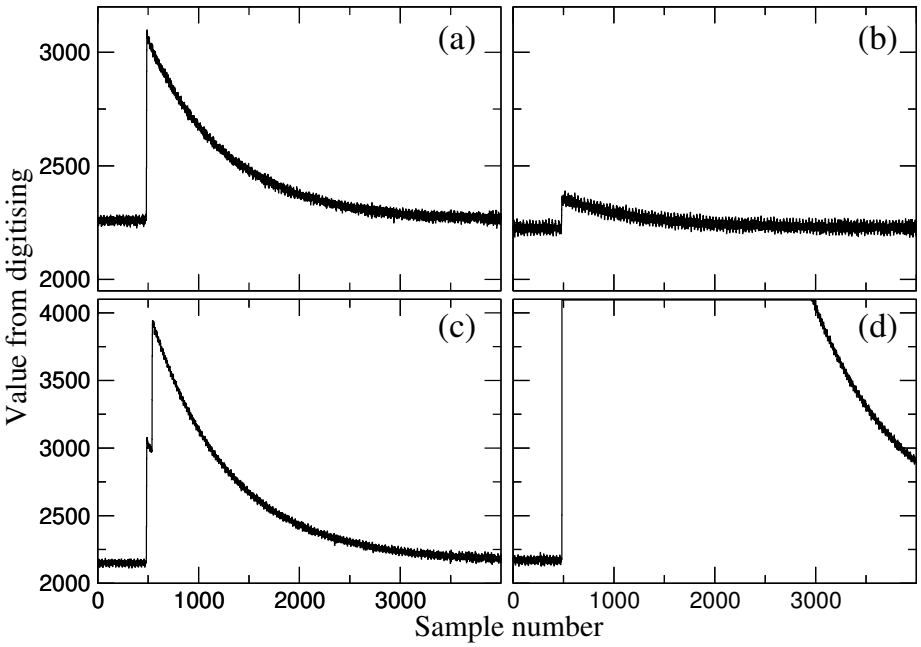

Figure 6.1: *Examples of different types of traces from FEBEX modules [92]. See text for more details.*

offline. Examples of traces are shown in Fig. 6.1. Each trace consists of 4000 samples and covers $\frac{4000}{60\ \mathrm{MHz}} \sim 70\ \mu$s. Figure 6.1(a) shows a trace from a detected α particle of several MeV while (b) has a much smaller amplitude and thus most likely shows the trace from an α particle escaping from the detector, or an electron. The positions of the rises of the pulses indicate that the respective particle triggered the system. The finite rise time of around 70 ns represents the charge collection time. The pulse height corresponds to the integrated current, which, in turn, is proportional to the deposited particle energy. The exponential tail is the discharge of the preamplifier. The decay time for each preamplifier channel is $\tau \sim 13\ \mu$s, and should be determined individually for each channel to optimise the energy resolution.

Figure 6.1(c) shows the trace from two α decays occurring rapidly in succession – most likely originating from a transfer reaction product. Figure 6.1(d) shows the trace from a high-energy particle, either from the primary beam or a fission event, whose energy saturates the trace. Using analog electronics, types (c) and (d) would have been difficult to extract any reliable information from. Using digital electronics, though, offline analysis of the traces can classify the events and provide useful energy and time measurements (see below).

In the ideal case, the traces should be smooth. In reality, the signals have some superimposed noise, coming from, for example, pickup noise from the detector-preamplifier connections, thermal noise, and digital noise. It was noted that a large part of the noise was periodic, with a periodicity of 32 samples, for the element 115 experiment. Thus, the parameters in the filters applied to our data were set to multiples of 32.

A trapezoidal filter was used for extraction of time information. The algorithm takes a trace as input and outputs an averaged derivative. For each sample, the difference between two non-adjacent portions of data is calculated. Each portion consists of 32 samples. The separation between them is 10 samples, chosen such that the separation covers the full rise time. The derivative assigned to each point is the difference between the average of the previous 32 samples minus the average of the portion of 32 samples that ends 42 samples before the point. This results in an arbitrary time shift in the derivative. The maximum of this derivative will occur when the first portion is just before the rise and the second portion is right after the rise. The time is extracted as the position of the maximum of the derivative. Three traces are shown in Fig. 6.2 together with the results of the trapezoidal filter.

Figures 6.1(c) and 6.2(b) show traces with two α particles occurring closely after each other and within the same event – i.e., the events are subject to so-called pile-up. Using digital electronics, the different energy

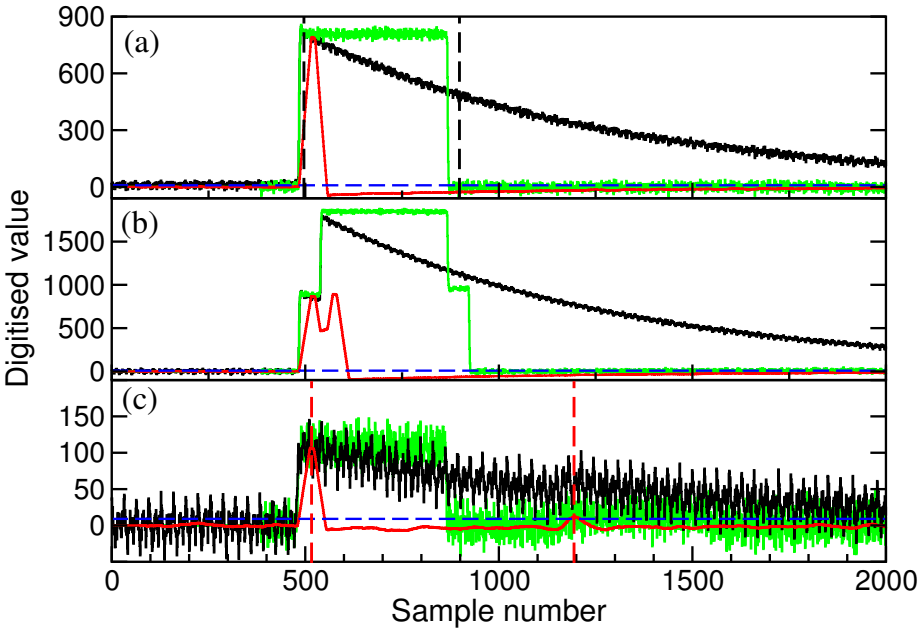

Figure 6.2: *Baseline restored trace (black) and the results after application of a short trapezoidal filter (red) and a MWD algorithm (green). The height where the width of the peaks in the trapezoidal filter is measured (to determine if the trace contains pile-up) is indicated in blue. (a) Single α. The vertical lines mark the region which was used for fitting of the τ. (b) Two subsequent α decays. (c) A trace from either an escaping α particle or an electron, followed by a small energy deposition from conversion electrons or Auger electrons.*

depositions can be resolved. In principle, the energy and timing data for the separate α particles can be extracted. For our element 115 search, however, where much longer lifetimes are expected, it was enough to check *if* an event is subject to pile-up or not. The applied method is based on the same trapezoidal filter used for the timing. Single pulses result in similar peak widths for the derivative. Traces containing more than one pulse will have either two such peaks *or*, if the two pulses are very close in time, one wider peak. The peak width of the derivative therefore indicates if the pulse contains pile-up or not. It was decided to measure the peak width by counting how many samples in the filtered data that have values ten or higher, and consider the pulse to be double if this number is larger than 90 samples. The traces shown in Fig. 6.2(b,c) were both found by using this routine. The height where the width is measured is indicated in the figures.

The maximum value of the trapezoidal filter corresponds roughly to the pulse height, and could hence also be used to extract the energy. It has the advantage of not requiring any detailed information about the pulse shape. However, to improve the resolution, a Moving Window Deconvolution (MWD) [103, 104] was used. The algorithm has two purposes. One is to linearise the exponential decay to make it easier to perform averages. The other is to introduce a cut-off in the exponential decay. Figure 6.2 shows the results of the MWD algorithm applied to three traces. For traces containing a single energy deposition, the energy is extracted as the difference between an average taken over a portion of the flat top and a portion of the baseline. Traces containing more than one energy deposition were treated in the same way, but do not necessarily give a proper energy measurement for any of the measured particles. In case the trace is saturated [see 6.1(d)], the peak height can still be extrapolated from knowing the saturation time and the preamplifier decay constant.

The decay constant was determined for each preamplifier channel. Deviations from an exponential behaviour were noted in the beginning of the slope and also at samples above around channel 1000. Therefore, an exponential curve was fitted to the region between samples 500 and 900 [see Fig. 6.2(a)]. Since some variation in the decay constant between different traces from the same preamplifier channel was observed, the fitting was made after summing hundreds of traces from each channel. The traces were taken from the α calibration, and only those events were used that were self-triggered, had energies in the expected region for α particles from the calibration source, and were not marked as pile-up events.

The described methods to extract energies, times and information about pile-up were applied to all traces. Times, energies, and a marker that indicates if the traces contain a pile-up or not, were written in ASCII format to a file, together with information from the n-side of the silicon detectors, the Ge detectors, and global event information such as real time, beam on/off status, target segment, etc. These files were used in further processing of the data.

6.2 Calibration of DSSSDs

Extensive detector calibrations using radioactive sources were done in the beginning and end of the experiment. Measurements were done with several different sources: a 4-line α source (^{148}Gd, ^{239}Pu, ^{241}Am, ^{244}Cm) and open sources of ^{133}Ba and ^{207}Bi emitting electrons, γ rays, and X rays. Also, a calibration with a pulser was made to check the response of preamplifiers and read-out electronics for very high energies. Since element 115 α decays are expected at $\sim$10 MeV, an accurate calibration in this energy region is crucial. Preferentially, the calibration should be done with α particles for which the detector response is as similar as possible.

However, our detectors have dead layers that are ~ 2 μm thick, and hence the α particles lose energy on their way to the active detector volume. The composition of the dead layer is a mixture of silicon, silicon oxides as well as aluminium which is added to serve as an electrical contact. For simplicity, the dead layer was assumed to be SiO_2 (2.32 g/cm^2). Unfortunately, we found that the dead layer was not uniform. This makes it more difficult to calibrate using external α-particle sources.

As the stopping power ($\frac{dE}{dx}$) of electrons is much smaller than the stopping power of α particles, they can be used for an almost dead-layer independent calibration. The disadvantages are that electrons from radioactive sources have lower energies, and that the detector response could be slightly different for α particles and electrons.

Yet another dead-layer independent technique is to calibrate using decays of implanted atoms. Here, particles with relatively high production cross sections and well-known α-decay energies, such as ^{254}No (see Fig. 5.3), are produced and implanted. For the element 115 experiment no in-beam calibration could be made. However, "unwanted" implanted ions from transfer reactions could serve as a replacement.

The strips in the implantation detector were first calibrated using two peaks from conversion electrons from ^{207}Bi at 482.7 and 975.7 keV, corrected by an average energy loss of $\sim$1 keV in the dead layer. From the low-energy ^{207}Bi calibration, a few peaks from α decaying implanted transfer reaction products could be identified and thus be used to refine the calibration at higher energies. One problem with using implanted nuclei is that not only the α particle but also the recoiling daughter nucleus deposit energy. Some of the energy deposited by the heavy daughter nucleus is lost due to plasma effects in the detector. From comparisons with tabulated α energies, it was found that if 1/2 of the recoil energy is assumed to be detected, all identified electron and in-beam α peaks agree with tabulated values within $<$10 keV. A rather strong α-line from

^{211}Po at 7.45 MeV was then used together with one line from the ^{207}Bi source for a new calibration of the implantation detector. Recalibrations were done for subsets of the data from the element 115 experiment using the ^{211}Po peak with $E_\alpha = 7.45$ MeV and the ^{212}Po peak with $E_\alpha = 11.66$ MeV, i.e. one peak just below and one peak just above the expected region for element 115 α decays (see Fig. 6.9). The box detectors were calibrated using only the two peaks from ^{207}Bi source measurements.

6.3 Dead layer determination

Detailed knowledge about the detector dead layers is important for reconstructing the energies of α particles that escape the implantation detector and are stopped in one of the box detectors. The energy loss in the dead layers can amount to several hundreds of keV, which must be added to the sum of the implantation detector and box detector energies to achieve spectroscopic quality for such events. The situation is illustrated in Fig. 6.3. The dead layer was determined for each pixel in the DSSSDs by comparing calibrated data from a long measurement with the 4-line α source with simulated data assuming various dead layer thicknesses, as will be described in this section.

Energy spectra for each of the 2048 individual *pixels* were obtained from the α source measurement. For two of the peaks – ^{148}Gd at 3.18 MeV and ^{244}Cm at around 5.8 MeV – the peak positions for both p- and n-side were extracted by calculating the centre of mass of the peak. A typical p-side energy spectrum from the 4-line α source for one pixel in the implantation detector is shown in Fig. 6.4(a). Figure 6.4(c) shows a typical energy spectrum from an entire strip in the implantation detector. The peak widths are slightly larger for the entire strip than for individual pixels. Figure 6.4(b) shows the ^{148}Gd α peak for three pixels along the same p-side implantation strip. The peak position clearly depends on

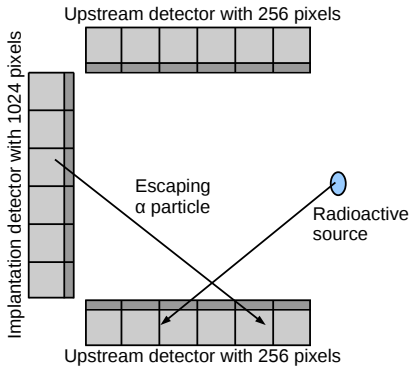

Figure 6.3: *Schematic illustration of TASISpec silicon detectors and the position of radioactive sources used for calibration. Light grey denotes the active detector areas, while dark grey denotes the p-side dead layers. Particles that are emitted from the radioactive source pass through one detector dead layer before reaching the active volumes. Particles that are emitted from the implantation detector into a box detector pass through the dead layers of both detectors. The traversed dead layer depends on the thickness and the angle of incidence.*

the chosen pixel, although the calibration coefficients for all pixels in one strip are necessarily the same.

The effect is more enhanced for the p-side strips in the box detectors, as shown in Fig. 6.4(d). As the p-side strips are oriented from the implantation detector towards the α source, the differences in the angle of incidence lead to very different effective dead layer thicknesses traversed by the α particles. The traversed length is related to the dead layer thickness by a "geometrical factor". This factor depends on the relative position of the α source and the detectors, and can calculated for every pixel.

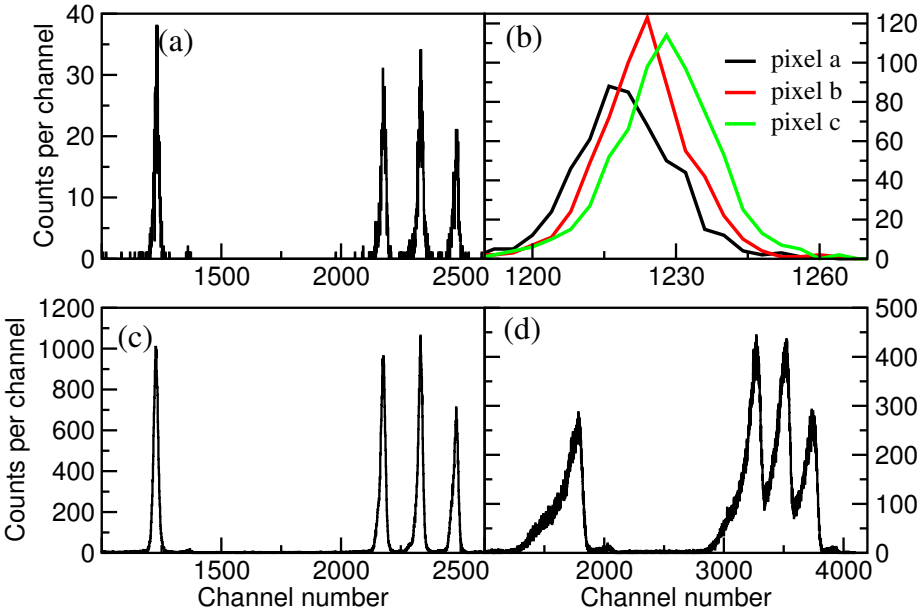

Figure 6.4: *(a) p-side energy spectrum from one pixel in the implantation detector from the long measurement with the 4-line α source. (b) Peaks from ^{148}Gd for three different pixels along one p-side implantation strip. (c) Energy spectrum from one implantation detector p-side strip. (d) Energy spectrum from one p-side strip in a box detector.*

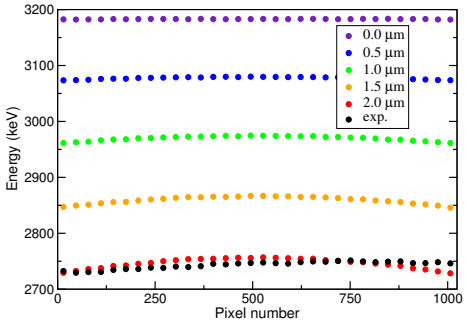

Figure 6.5: *^{148}Gd peak positions for all 32 pixels along one central p-side strip in the implantation detector. The experimental peak positions are shown in black. Simulated peak positions relate to constant dead layers of 0.0-2.0 µm.*

Implantation detector

In the virtual TASISpec in `Geant4` space, the dead layer of each pixel can be adjusted. As a first attempt, constant dead layers were simulated and compared with calibrated data from the α source measurement. Results for one p-side strip in the implantation detector are shown in Fig. 6.5. The simulated peak positions follow the expected trend with symmetrically falling values when going from the centre towards the peripheral parts of the detector. It is clear that the dead layer thickness is around 2 μm. It is also clear that the dead layer thickness is not uniform.

The individual dead layer thicknesses were adjusted by adding linear and quadratic terms with respect to the distance to the centre of the detector. The coefficients were varied until the simulations reproduced the measured peak positions in all pixels within 10 keV. The final dead layers were generated from a function containing a constant term, different linear terms in the x and y directions, and quadratic terms in the x and y directions with different coefficients in the different quadrants.

"Box" detectors

Since it has been established that a smooth dead layer with a quadratic form is needed to describe the implantation detector, the same procedure could be applied to the box detectors. However, the trial and error method can be automatised. To find the dead layer in a more systematical way, the difference in energy between the experimental and simulated peak positions for each pixel was calculated assuming a constant dead layer. The energy difference for each pixel is translated into a dead layer thickness. In turn, this thickness is corrected by the geometrical factor. The process can be iterated until satisfactory agreement occurs. The process is illustrated and further explained in Fig. 6.6.

The translation from an energy difference to a dead layer thickness is complicated by the fact that the energy loss is not linear. The energy loss

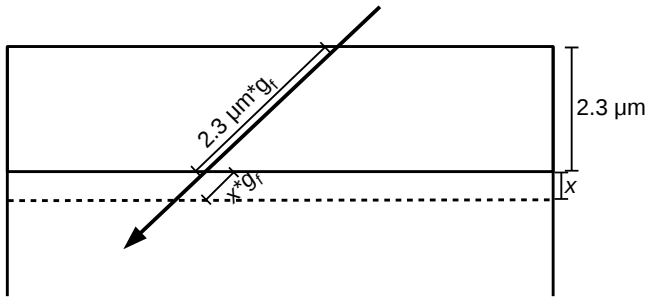

Figure 6.6: *An illustration of the method used to estimate how much the dead layer x for a certain pixel deviates from the assumed 2.3 μm dead layer. The total traversed extra dead layer thickness is $X = xg_f$, where g_f is the geometrical factor. The extra thickness x was obtained as follows: i) The extra energy loss is defined as the difference between calibrated data and simulation data for 2.3 μm thickness. ii) This energy loss is transformed to a dead layer thickness using $\frac{dE}{dx}(X)$ for SiO_2, approximated at a dead layer of 2.3 $\mu m * g_f$.*

as a function of how far an α particle with initial energy of 3.182 MeV (^{148}Gd) has travelled in SiO_2 was constructed. The energy loss per μm when the particle is at X μm was estimated as the difference between the total energy after passing (X+0.5) μm of dead layer and after passing through (X-0.5) μm. A second order polynomial was fitted to the function. The result is shown in Fig. 6.7.

The experimental peaks from ^{148}Gd from each pixel in box detectors 1, 3, and 4, were compared with data from simulated constant dead layers of 2.3 μm. The energy difference ΔE was transformed into a length difference ΔX in dead layer traversed by the particle by dividing it by the energy loss $\frac{dE}{dx}$ after the length 2.3 $\mu\cdot$ g_f. This length is then divided by the geometrical factor to obtain the correction to the constant dead layer. For box detector 2 the simulated constant dead layer was 2.5 μm. Iterating the procedure gave negligible improvement. The resulting value for each pixel is shown in Fig. 6.8.

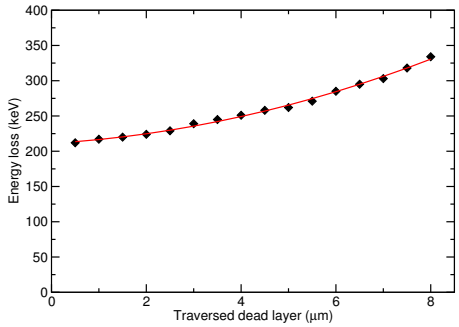

Figure 6.7: *Energy loss for an α particle of initial energy 3.182 MeV as a function of how much 2.32 g/cm^3 SiO_2 the particle has already passed; $\frac{dE}{dx}(X) = 1.355X^2 + 4.0851X + 211.15$ keV.*

The surfaces are mostly smooth and seem to be similar to the one for the implantation detector. Since it is not realistic with dead layers that vary in discrete jumps from pixel to pixel, functions with the same degrees of freedom as was used for the implantation detector were fitted to the surfaces. The final dead layer thicknesses of the box detectors were obtained by adding the constant dead layer thickness.

6.4 Reconstruction of energies

The knowledge of the dead layer of each pixel was used to reconstruct the energies of the particles that escape from the implantation detector and enter a box detector. Knowing what implantation detector pixel the particle comes from and what box detector pixel it goes to, the total amount of dead layer the particle has traversed can be obtained. The geometrical factors were calculated for each combination of implantation detector pixel and box detector pixel.

The decay energy is the sum of the energy deposited in the box detector, the energy deposited in the implantation detector, and the energy loss in the dead layers. The calculation of the energy loss is

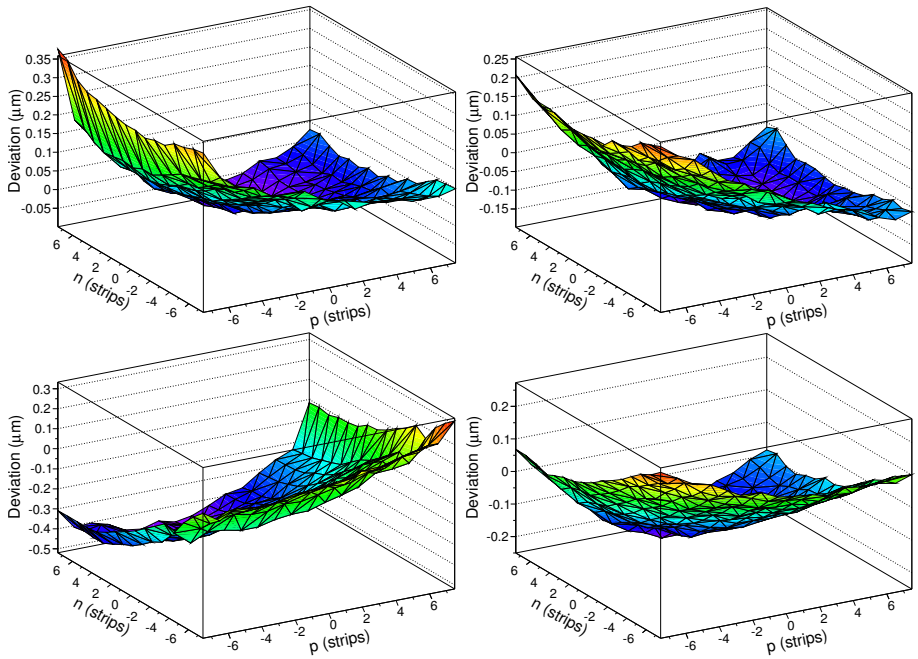

Figure 6.8: *Surfaces describing the difference between a constant dead layer and the dead layer which is implied by data for box detector 1 (upper left), 2 (upper right), 3 (lower left) and 4 (lower right). An initial constant dead layer of 2.3 µm was used for detectors 1, 3 and 4. For detector 2, a constant dead layer of 2.5 µm was used instead. The viewpoint is such that the detectors are seen from the point on the implantation detector which is closest to the p- and n-side strips that have the lowest numbers.*

started from the energy measured in the box detector. The total energy loss in the total traversed dead layers was calculated by approximating $\frac{dE}{dx}$ to be constant over $dx = 0.01$ μm.

Only the events that are likely to originate from α particles were reconstructed. The reconstructed events were assigned to their respective pixel in the implantation detector. The resolution of the reconstructed events is lowered by imperfections in the dead layer determination, and by the fact that the geometrical factor depends on the exact positions within the implantation and box detector pixels. The reconstruction of the energies and the dead layer determination is discussed in Paper III [57].

6.5 Additional treatment of DSSSD data

In some events, particles deposit their energies in more than one strip. Such events were more carefully investigated. If the energy depositions were coincident in time and from neighbouring strips, the energies were added and assigned to the strip containing the largest energy ("add-back"). If the energy depositions were not coincident, only the data from the strip with the largest measured energy was kept. Furthermore, for all events, the energy measured in the n-side and p-side strip was compared, and the event was discarded if the discrepancies were too large. Also, energies measured by the box detectors were kept only if the signal was coincident in time with a selected signal in the implantation detector.

After the add-back and data selection, each event contained one energy and one time from a well-defined pixel in the implantation detector and possibly one energy from one well-defined pixel in a box detector. Figure 6.9 shows beam-off spectra from the implantation detector for the entire experiment. The spectrum from events contained within the implantation detector, as well as the spectrum containing also reconstructed events, are shown. The reconstruction routine adds counts in the peaks from transfer products such as ^{212}Po. The energy resolution of

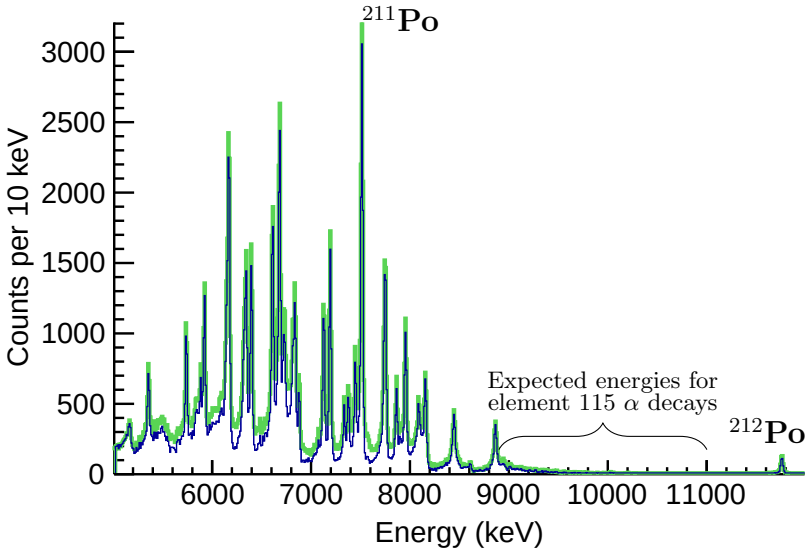

Figure 6.9: *Beam-off energy spectrum from the implantation detector. The histogram in blue is from before the reconstruction routine, while the spectrum including reconstructed events is shown in green.* ^{211}*Po has* $E_\alpha =$ 7.45 *MeV while* ^{212}*Po has* $E_\alpha = 11.66$ *MeV. The peaks are shifted to higher energies due to summation with the recorded recoil energy (see Sec. 6.2). The binning is 10 keV per channel.*

the reconstructed events is degraded by unavoidable imperfections in the routine. The region 9-11 MeV is particularly interesting for the element 115 analysis, as the α particles in the chains are expected in this region. The relatively low number of events observed in this region makes it easier to firmly establish correlated chains.

6.6 Correlation analysis

At this stage, the events consist of one energy signal in one implantation detector pixel at one certain time. Searches for correlations in the data can then begin. Different kinds of correlations, such as α-

α-α, implantation-α-fission, implantation-α-α and α-α-fission, can be searched for. Implantations are characterised by typical energies and beam-on status. α particles are characterised by energies that are, in general, lower than the implantation energies, and can have either beam on or off status. Fissions are characterised by very high energies. The different energy intervals and the time periods during which correlations are searched for constitute the search parameters.

For the element 115 data, several different correlation searches were done. A total of thirty correlated chains were found in implantation-α-fission, implantation-α-α, and implantation-SF searches using the conditions

- $11.5 < E_{\mathrm{rec}} < 18.0$ MeV, beam on;
- $9.0 < E_{\alpha 1} < 12.0$ MeV, $\Delta t_{\mathrm{rec}-\alpha 1} = 5$ s, beam off, or
  $10.0 < E_{\alpha 1} < 12.0$ MeV, $\Delta t_{\mathrm{rec}-\alpha 1} = 1$ s, beam on;
- $9.0 < E_{\alpha 2} < 11.0$ MeV, $\Delta t_{\alpha 1-\alpha 2} = 20$ s, beam off, or
  $9.5 < E_{\alpha 2} < 11.0$ MeV, $\Delta t_{\alpha 1-\alpha 2} = 5$ s, beam on;
- $E_{\mathrm{SF}} > 120$ MeV, $\Delta t_{\alpha 1-\mathrm{SF}} = 30$ s or $\Delta t_{\mathrm{rec}-\mathrm{SF}} = 30$ s, beam off.

Data in the vicinity – in time and in space – of the correlated events was searched more thoroughly. Data that followed an implantation event that was part of an identified correlation was printed and sifted for more possible members of the correlated chain. During such detailed search, also particles escaping full detection could be found. For the correlations found only in the implantation-α-α search, the data in the pixel is scanned for the expected fission end member.

6.7 Germanium detectors

The 25 Ge crystals from the five composite detectors were read out by digital electronics. The flat-top energy and baseline position was extracted and recorded for each trace. The high count rate of the germanium detectors (well above 10^4/s for beam-on periods) causes instabilities in the

baseline, but knowledge of the baseline and top positions can be used to correct this [59]. Also a pile-up flag is set if the event contains more than one energy deposition. Pile-up events were discarded in any further analysis.

The Ge detectors were calibrated using γ lines from ^{133}Ba and ^{152}Eu sources. The X ray and γ ray transitions from the barium source cover mainly lower energies up to about 400 keV, while the ^{152}Eu source provides intense γ transitions up to 1.4 MeV. This is sufficient for our purposes, as our main interest lies in events below 500 keV. Linear recalibrations were done for sub-sets of the data using the 511 keV line from β^+ decays and a line at 139.7 keV from neutron-induced reactions in ^{74}Ge.

No add-back was made for events where multiple detector crystals recorded simultaneous energy depositions. We are mainly interested in low-energy events where the Compton scattering between neighbouring detector crystals is less pronounced, and we do not want to miss any potential coincidences between K-X rays and subsequent L-X rays. More details on the treatment of data from the germanium detectors is described in Ref. [59].

7

Statistical analysis

By searching for correlations in the data, thirty correlated α-decay chains ending with spontaneous fission were found. Before the chains can be considered to stem from element 115, the number of randomly correlated chains in the full data set needs to be estimated. In this chapter I start with describing the use of a well-established method to determine the number of expected randomly correlated chains. Once the non-randomness of the chains is established, the chain characteristics can be scrutinised. Are they similar to chains from previously known isotopes? Do they stem from the same isotope, or do they have different origins? Depending on the overall knowledge about nuclei in the relevant region, different questions may be asked and, possibly, answered. If there is abundant data from a certain isotope, it might be most relevant to ask whether a new chain has decay characteristics that fit with such a reference data set. If no reference data set is available, it might be more relevant to ask whether a group of new chains all have a common origin or if they should rather be split in sub-groups. These two questions are not the same, but naturally intertwined. In this chapter I describe how I generalised a previously suggested method aimed at investigating if a set of lifetimes are likely to have a common origin, and developed it in order

to investigate sets of chains rather than sets of individual lifetimes. Furthermore, I describe two versions of yet another method that I suggest to investigate the congruence within a set of chains, and its similarities with other sets of chains. The methods presented here focus on decay times and correlations, while decay energies are only used as supportive arguments.

7.1 Random correlations in the background

There are several sources of events in our detector that are not related to the implantation and decay of element 115. Even though, for example, target-like products can be of interest in themselves, they will in this chapter be referred to as unwanted "background". Some of these events have similar characteristics as the implantation signals, α-particle signals and fissions that we are looking for. In the case of true element 115 events there are certain time correlations between the different events in the chains, whereas for other particles there should be no such correlations. However, there is a chance that background events happen to show up in time intervals that mimic the real element 115 chains. To assess this potential problem, the number of chains of certain types that are expected from the background can be calculated using statistical methods.

As an example, let us consider a real chain consisting of four decays: The implantation of an element 115 ion, followed within 2 s by an α decay, followed within 10 s by an α decay, followed within 50 s by a fission. Each event is characterised by a certain energy. The expected number of times during an experiment that background events occur in a sequence that mimics the real chain can be estimated: Every time an implantation-like event occurs, a theoretical time gate is opened and the probability that an α-like background event occurs within this period is calculated. If such an event occurs, a new gate is opened and the

probability for a second α background event is calculated. If also this event occurs, a last gate is opened and the probability for a fission to occur within is calculated. The total number of random chains can then be estimated to be the number of implanted events times these three probabilities.

The expected number of events within each time gate is given by the product of rate and time. Assuming that the events are Poisson distributed, the probability P for observing ν events when μ is the number of expected events within the pre-defined time interval, is [105]

$$P(\nu, \mu) = \frac{e^{-\mu}\mu^{\nu}}{\nu!} \tag{7.1}$$

The probability for observing one or more events, $P(\geq 1, \mu) = 1 - P(0, \mu) = 1 - e^{-\mu}$, is used for calculating the probability that at least one random background event occurs within the time gate. The time gates should be chosen so that they cover the entire time spans in which correlations would be accepted. As a rule of thumb, time gates of no less than three half lives should be used.

The background rates in each of the energy intervals vary strongly between beam on and beam off periods, between different parts of the detector, with varying beam intensities, and with beam-shutoff status. The first aspect has been taken care of by considering beam off and beam on periods separately. For example, if the first α particle is seen when the beam is on, we consider the rate of events during beam-on periods. The time gate used in the equations should also be modified to cover only the beam-on part of the initial time gate, since we do not even consider data that was taken during beam-off periods. The variation over the detector is handled by considering the pixels in the implantation detector separately. The number of events in the energy intervals were determined for each pixel. The number of implantations were calculated from the plain beam-on spectra for each pixel in the implantation detector. The

α-like and escape-like events were calculated from reconstructed spectra, where any coincident signal from the silicon box detectors was added to the implantation detector energy signal together with an amount of energy that compensates for the dead layer. The number of beam-off fission-like events in a pixel was either zero, one, or, in one case, two. By far, the most common number of fission events was zero. In principle, this would mean that almost all pixels have zero expected randomly correlated chains. To overestimate rather than underestimate the expected random chains, the number of fission events in a pixel was set to the actual number if it was one or two, and otherwise to the average value over the entire detector. The number of expected random chains was calculated for each individual pixel, and then these contributions were added. The variations in rates with beam intensity were not considered, and neither was the beam shut-off status.

In Paper V [66], the number of expected random chains are given for those types of short chains that were observed. The events were of the types given in Table 7.1 together with their notation, characteristic energy intervals, and beam status. The seven chains were of the types r-$\boldsymbol{\alpha}$-**SF**, r-**e**-**SF**, r-α-$\boldsymbol{\alpha}$-**SF**, r-$\boldsymbol{\alpha}$-$\boldsymbol{\alpha}$-**SF**, and r-**e**-e-**SF**. The time gates that were used were 2, 10, and 50 s, respectively, for the each of the decay steps. The number of expected randomly correlated chains during the experiment range from about 10^{-9} for the type of chain which has two beam-off full-energy or reconstructed α detections, to about 0.1 when two α particles are escaping from the detector. Hence, the observed chains are most likely truly correlated.

7.2 Generalised Schmidt-test

Around the turn of the millennium, the question of congruence within sets of decay chains was investigated by K.-H. Schmidt. In Ref. [106], he elaborates on the distribution of times drawn from an exponential prob-

Table 7.1: *Characteristics of different types of events that occur in chains. The energy intervals refer to those used in the calculations of random correlations.*

notation	type	beam status	ΔE (MeV)
r	implantation	on	11.5-18.0
α	α, full energy or reconstructed	on	9.0-11.0
$\boldsymbol{\alpha}$	α, full energy or reconstructed	off	9.0-11.0
e	α, escape	on	< 4.0
e	α, escape	off	< 4.0
SF	fission	off	> 120

ability density function. He uses the fact that the shape of a distribution of logarithmic lifetimes $\theta = \ln(t)$ associated with a radioactive decay does not depend on the half-life, and proposes a "new test" for congruence of measured lifetimes. The test is designed to investigate if it is likely that all elements in an ensemble of decays are coming from the same decay. The standard deviation σ_θ of a set of n measured logarithmic lifetimes should always – regardless of the half life – be within a certain interval, and is defined as

$$\sigma_\theta = \sqrt{\frac{\sum_{i=1}^{n}(\theta_i - \bar{\theta})^2}{n}}, \quad \bar{\theta} = \frac{\sum_{i=1}^{n}\theta_i}{n}. \tag{7.2}$$

If the number of available lifetimes is above about one hundred, the expectation value of σ_θ becomes 1.28, and the region $1.28 \pm 2.15/\sqrt{n}$ constitutes a 90% confidence interval. For smaller data sets, these limits depend on the number of data points in a more complicated way (for tabulated intervals, see Ref. [106]). For example, a data set with fourteen lifetimes results in σ_θ values in the region [0.73,1.77] with a 90% probability. σ_θ below the confidence interval indicates that the experiment has not been sensitive to all lifetimes (e.g., long lifetimes might be

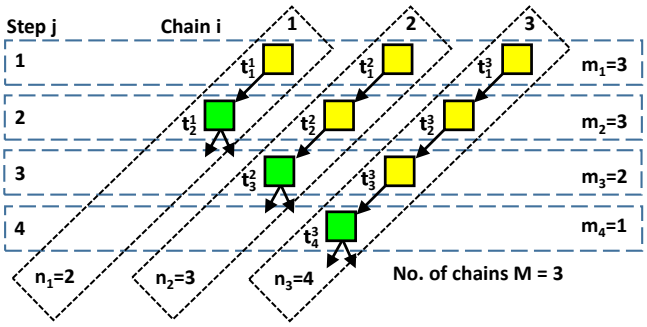

Figure 7.1: *Three examples of decay chains of different lengths, together with the notations used in this chapter. Yellow squares denote α decay, while green squares denote spontaneous fission.*

discriminated if the measurement time is too short), that the data set is unjustly pruned, or that the data does not originate from a radioactive decay. σ_θ above the confidence interval can indicate the presence of more than one radioactive species.

When applying the Schmidt test to chains of correlated decays, each decay step is considered separately. However, the lifetimes within one chain hold more information if they are considered simultaneously. For example, a data set of several chains might contain in each separate decay step one lifetime that is remarkably long, while still having σ_θ values within the 90% confidence interval. Nonetheless, if the remarkably long half lives all come from a certain chain, there is reason to question the assignment of this chain to the same origin as the other chains.

A generalisation of the Schmidt test can be made in order to quantify these correlations. Assume that M chains have been observed and that each chain i contains n_i decay steps. Let m_j be the available lifetimes in step j. Let further t_j^i be the lifetime associated with step j in chain i, and $\theta_j^i = \ln(t_j^i)$. Figure 7.1 exemplifies the notation. The measure

$$\xi_{M,\{n_i\}} = \sqrt[2]{\frac{\sum_{i=1}^{M} \sqrt[n_i]{\Pi_{j=1}^{n_i}(\theta_j^i - \bar{\theta}_j)^2}}{M}} \ , \ \bar{\theta}_j = \frac{\sum_{i=1}^{m_j} \theta_j^i}{m_j} \tag{7.3}$$

can be constructed for any data set. It characterises the congruence within the *entire* data set, by taking into account differences between lifetimes observed in *chains* rather than in single decay steps. By multiplying the separate deviations $(\theta_j^i - \bar{\theta}_j)^2$ with each other, i.e. calculating the geometric average, all lifetime data from one chain are considered jointly. Such cohesion would not occur if the arithmetic mean would be considered instead. Introducing the n_ith root allows for a further generalisation to sets of chains of unequal length. The suggested measure reduces to the original Schmidt test if only one decay step is considered. To clarify the procedure, ξ for the fictive data set in Fig. 7.1 is written out explicitly:

$$\begin{aligned}\xi^2 =& \frac{\sqrt[2]{(\theta_1^1-\bar{\theta}_1)^2(\theta_2^1-\bar{\theta}_2)^2}}{3} + \frac{\sqrt[3]{(\theta_1^2-\bar{\theta}_1)^2(\theta_2^2-\bar{\theta}_2)^2(\theta_3^2-\bar{\theta}_3)^2}}{3} + \\ &+ \frac{\sqrt[4]{(\theta_1^3-\theta_1)^2(\theta_2^3-\bar{\theta}_2)^2(\theta_3^3-\bar{\theta}_3)^2(\theta_4^3-\bar{\theta}_4)^2}}{3}\end{aligned} \tag{7.4}$$

The distribution for the measure ξ was investigated by applying it to simulated data from exponential distributions for data sets of fourteen decay chains containing three decay steps. The distributions of the measure are shown in Fig. 7.2(a). If only the first decay step is used (the original Schmidt test) the distribution is wide. The distributions get more narrow if more decay steps are used. As in the original test, the new measure is independent of the half lives, as also shown in Fig. 7.2(a).

In Fig. 7.2(b), the distribution of ξ for chains with three steps are shown for different number of chains M. For a large number of chains, the

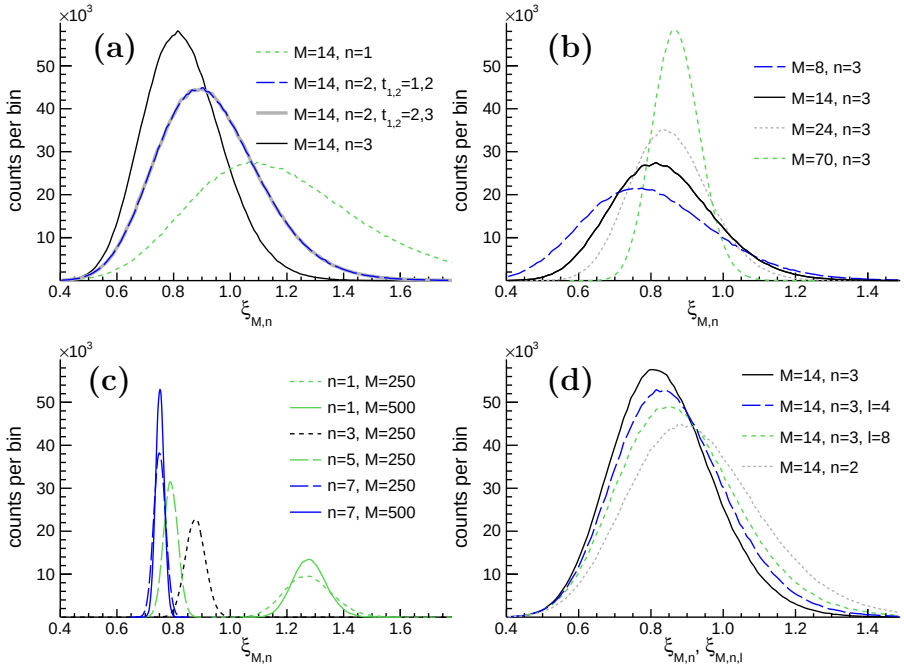

Figure 7.2: *Distributions of ξ when applying the test to simulated sets of decay chains. In this figure, n denotes the maximum number of decay steps considered. (a) ξ for fourteen decay chains with $n = 1, 2, 3$. The widest distribution (green) corresponds to when only one decay step is considered. The two identical curves are from considering two decay steps, for two different sets of lifetimes. The most narrow distribution corresponds to fourteen three-step chains. (b) ξ for different numbers of decay chains, each with three decay steps. A large data set gives a narrow distribution. (c) ξ for very large sets of chains with varying lengths. The averages stabilise around different values depending on the chain lengths. Large data sets lead to more narrow distributions. (d) ξ for data sets where some chains consist of two steps and some of three steps. Here, l specifies the number of chains that terminate after two steps.*

expectation value of ξ is shifted and the distribution gets more narrow. Figure 7.2(c) shows the effect of considering longer chains and very large data sets. The expectation value of ξ depends on the chain length, while the distribution width decreases with M. Simulations of how the measure behaves for data sets where some number l of chains terminate after only two decay steps are shown in Fig. 7.2(d). Increasing l from zero to M, the distribution gradually changes from the respective distributions from $\xi_{M,\{n_i\}=3}$ to $\xi_{M,\{n_i\}=2}$.

The simulated confidence limits for $\xi_{M,\{n_i\}}$ can be used for evaluating experimental values of ξ, to test the congruence within sets of chains. This test has been applied to the short decay chains of element 115 and the results thereof have been communicated in Paper IV [63].

7.3 Figure-of-Merit, FoM

Another method to investigate the congruence within sets of chains, and in addition quantify similarities between different sets of chains, is to define a Figure-of-Merit (FoM). A FoM should give a quantitative value which measures the congruence between a measured time t and a reference distribution characterised by the parameter τ. Here, we suggest the following form of an FoM:

$$FoM = \frac{et}{\tau} e^{-\frac{t}{\tau}}. \tag{7.5}$$

where e is Euler's number. This particular form of the FoM ranges from zero to one, and is motivated below from three different, but similar, perspectives.

7.3.1 Likelihood function

For radioactive decay processes, the lifetime T is a stochastic variable which can take on any positive value t, with the probability density

function

$$f_T(t) = \frac{1}{\tau} e^{-\frac{t}{\tau}}, \quad t \geq 0, \tag{7.6}$$

where τ is the average lifetime.

A lifetime t is one observation of the stochastic variable T. The probability of observing a time t in a time interval Δ_t around t is found by

$$P_{\Delta_t} = \int_{\Delta_t} \frac{1}{\tau} e^{-\frac{t}{\tau}} dt. \tag{7.7}$$

The integral over all possible times ($0 \leq t < \infty$) is unity.

It could be tempting to use the value of $f_T(t)$ as a measure of congruence between a lifetime t and a reference lifetime τ. However, this is not a suitable measure, since a shorter time t will always give higher values than longer times. As an alternative, let us consider the likelihood function $L(\tau)$. It describes the likelihood for different values of τ given a measured time t. $L(\tau)$ is the same expression as $f_T(t)$, but with τ as the variable and t as a parameter:

$$L(\tau) = \frac{1}{\tau} e^{-\frac{t}{\tau}}. \tag{7.8}$$

Figure 7.3 shows $L(\tau)$ for three different parameters t. The integral of $L(\tau)$ from 0 to ∞ is not convergent, which means that $L(\tau)$ is not a probability density function. This is, however, not a problem, as we are only interested in the function itself. The maximum of $L(\tau)$ occurs when $t = \tau$, with a value of

$$L(\tau = t) = \frac{1}{et} \tag{7.9}$$

and the range $0 \geq L(\tau = t) \geq \infty$. If we want to use the likelihood function as an FoM, $L(\tau)$ should be normalised such that the range is [0,1]. Division by the maximum value $L(\tau = t)$ gives the normalised

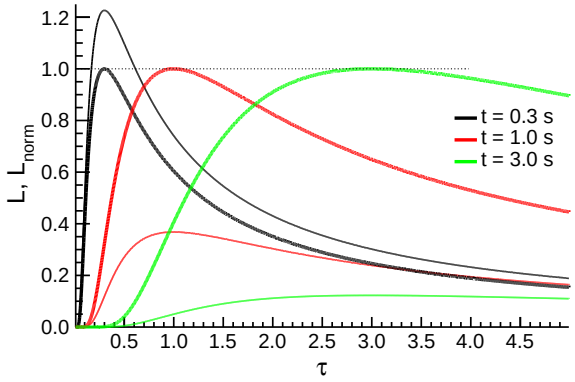

Figure 7.3: *Likelihood functions $L(\tau)$ for three parameters t as functions of τ (thin lines) and normalised likelihood functions $L_{norm}(\tau)$ where the maximum value is one (thick lines).*

likelihood function

$$L_{norm}(\tau) = \frac{et}{\tau} e^{-\frac{t}{\tau}} \tag{7.10}$$

which is plotted in Fig. 7.3.

$L_{norm}(\tau_{ref}) \approx 1$ if the reference τ_{ref} is close to a given t, and will be smaller otherwise. This is what we would expect from a sound measure on the congruence between a data point t and the reference value τ_{ref}, and therefore it is a suitable FoM.

7.3.2 Distribution of logarithms of times

Here, we start our quest for a FoM by studying another stochastic variable $Y = \ln(T)$, the natural logarithm of the observed lifetime. The probability density function of the logarithms of lifetimes $f_{\ln(t)}(\ln(t))$ from an exponential distribution $f_T(t)$ can be found via the cumulative distribution function $F_T(t) = \int_0^t f_T(t')dt' = P(T \leq t)$. The cumulative

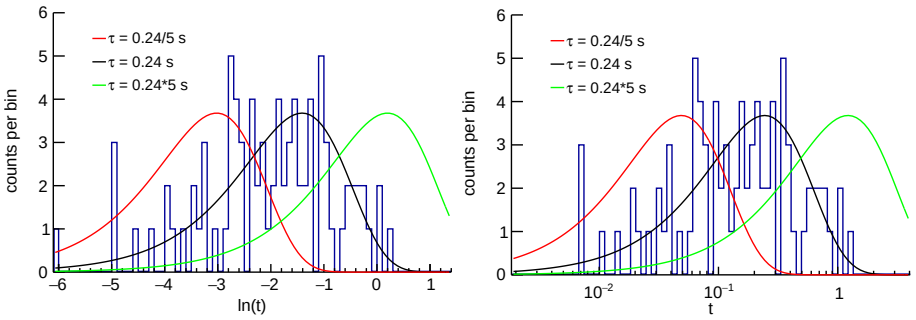

Figure 7.4: *Data from the first decay step in chains assigned to the isotope* $^{288}115$*. (Left) Logarithms of lifetimes,* $y = \ln(t)$*, together with Eq. 7.13 renormalised to fit the data for three parameters* τ *corresponding to the average lifetime* $\tau = \bar{t} =$ *0.24 s,* $\tau = 5\bar{t}$*, and* $\tau = \bar{t}/5$*, respectively. As can be seen, different values of* τ *merely shift the curve without changing the shape. (Right) Lifetimes in logarithmic-sized bins on a logarithmic scale, together with Eq. 7.15 for the average lifetime* $\tau = \bar{t}$*,* $\tau = 5\bar{t}$*, and* $\tau = \bar{t}/5$*, respectively.*

distribution function for Y is given by

$$F_Y(y) = P(Y \leq y) = P(\ln(T) \leq y) = \tag{7.11}$$

$$= P(e^{\ln(T)} \leq e^y) = P(T \leq e^y) = F_T(e^y) \tag{7.12}$$

The probability density function for Y, $f_Y(y)$, is found by taking the derivative of $F_Y(y)$ with respect to y:

$$f_Y(y) = \frac{d}{dy} F_T(e^y) = f_T(e^y) \cdot e^y = \frac{1}{\tau} e^{-e^y/\tau} \cdot e^y \tag{7.13}$$

$f_Y(y)$ has unit integral over the real axis, and is thus a probability density function. The maximum value is e^{-1} (independent of τ) and occurs when $y = \ln(\tau)$, i.e. $t = \tau$. Figure 7.4(a) shows the logarithms of the measured lifetimes from the first step in the decay chains assigned to $^{288}115$, together with $f_Y(y)$ (renormalised to match the data) with $\tau = \bar{t}$, the average lifetime. $f_Y(y)$ goes to zero for very small and very

large times, and can thus be used to measure the level of congruence between a lifetime t and a reference lifetime τ. By multiplying with e, the range becomes $[0, 1]$. Evaluating $ef_Y(y)$ for $y = \ln(t)$, we obtain the previously derived FoM

$$FoM = e\frac{1}{\tau}e^{-\frac{e^{\ln(t)}}{\tau}}e^{\ln(t)} = \frac{et}{\tau}e^{-\frac{t}{\tau}}. \tag{7.14}$$

7.3.3 Logarithmic-sized bins

Yet another way of deriving the same FoM is done in Ref. [106], where the authors choose to plot lifetime data in logarithmic-sized bins. They show that the distribution of times from an exponential distribution is

$$\frac{dn}{d(\ln(t))} \propto e^{\ln(t)+\ln(\frac{1}{\tau})} \cdot e^{-e^{\ln(t)+\ln(\frac{1}{\tau})}}. \tag{7.15}$$

This function can be seen as a probability density function. It is bell-shaped and slightly asymmetric. As emphasised by the form of Eq. 7.15 when viewed as a function of $\ln(t)$, τ enters as an additive term and thus only shifts the function. Figure 7.4(b) shows the measured lifetimes from the first step in decay chains assigned to $^{288}115$ plotted in logarithmic bins, together with Eq. 7.15 with three different half-lives. The function tends to zero for small and large times, and the height is independent of τ. To obtain an FoM with range $[0, 1]$, we take the constant of proportionality to be e. The expression simplifies into

$$FoM = \frac{et}{\tau}e^{-\frac{t}{\tau}} \tag{7.16}$$

7.4 FoM taking uncertainties into account

We have until now overlooked an issue in constructing a useful FoM: The reference lifetimes τ are averages $\bar{t}$ of n measured lifetimes, and can have rather large statistical uncertainties. We have calculated the experimen-

tal reference lifetimes and estimated the (asymmetric) 1σ upper (τ_u) and lower (τ_l) limits. The uncertainty can be propagated to the FoM. However, to propagate asymmetric uncertainties is not straightforward. A different way to incorporate uncertainties in τ, which we will make more use of, is to consider a smeared exponential reference distribution that depends on the number of reference lifetimes. The smearing was done analytically and via Monte Carlo simulations.

The first step is to consider the uncertainty in τ itself. Usually, the uncertainty is compressed into upper (τ_u) and lower (τ_l) confidence limits. For 1σ, these limits can be calculated according to Eqs. 18 in Ref. [105]:

$$\tau_{l/u} = \frac{\bar{t}}{1 \pm \frac{1}{\sqrt{n}}} \tag{7.17}$$

The limits are useful, but do not contain all available information. Instead, it is of interest to consider the underlying relative likelihood for all values of τ. To construct such distributions by Monte Carlo simulations, values for $\tau > 0$ were randomly (uniformly) picked. An exponential distribution with this τ was constructed and n lifetimes were simulated, where n is the number of experimentally measured lifetimes. Then, the average of these n lifetimes, $\bar{t}$, is calculated. If $\bar{t}$ agrees within $\pm$ 1% of the experimentally measured average lifetime, the τ is filled into a histogram. In case the average does not agree with the experiment, the corresponding τ is not kept. This procedure, starting from the selection of a random τ, is repeated until a smooth histogram emerges. Figure 7.5(a) shows one such histogram, where the integral has been normalised to one. The shape of the histogram is determined by the number of measured lifetimes n and the measured average lifetime, $\bar{t}$. In Ref. [105], this is done analytically: "For a given life time τ, the probability density of the random variable $\bar{\tau}$ is given by the product of the probability densities of the individual time values t_i, integrated over all combinations which

conserve the mean value $\bar{t}$" [105]. The resulting Eq. 16 in Ref. [105] is

$$p_n(\bar{t}|\tau) = \frac{n^{n+1}}{n!}\frac{\bar{t}^{n-1}}{\tau^n}e^{-\frac{n\bar{t}}{\tau}} \equiv p_{n,\bar{t}}(\tau). \tag{7.18}$$

$p_n(\bar{t}|\tau)$ should be read as "the probability of obtaining $\bar{t}$ if τ is given". This is somewhat difficult to grasp as the measured, and hence static, quantity is $\bar{t}$. However, there is actually nothing preventing τ from being a variable and $\bar{t}$ from being a parameter. To emphasise this, it will from now on be written as $p_{n,\bar{t}}(\tau)$. The integral over the positive real axis is solved by a change of variables ($\frac{n\bar{t}}{\tau} = y$) and a number of partial integrations and has the value

$$\int_0^\infty p_{n,\bar{t}}(\tau)d\tau = \frac{n}{n-1}. \tag{7.19}$$

Normalising to one, we get the function

$$p_{n,\bar{t},norm}(\tau) = \frac{p_{n,\bar{t}}(\tau)}{\frac{n}{n-1}} = \frac{n^{n-1}}{(n-2)!}\frac{\bar{t}^{n-1}}{\tau^n}e^{-\frac{n\bar{t}}{\tau}} \tag{7.20}$$

which is a probability density function for τ. This function is plotted in Fig. 7.5(a), and agrees well with the Monte-Carlo based histogram.

Now, the idea is to combine the probability density function for an exponential distribution with the knowledge of the likelihood function for different values of τ into a probability density function that takes into account the uncertainty in τ. The new smeared probability density function was constructed by repeating the following procedure: A τ was selected according to a probability governed by $p_{n,\bar{t},norm}(\tau)$, and then a time t was selected from the exponential distribution corresponding to the selected τ. Figure 7.6 shows the resulting histogram. Analytically, the described procedure is equivalent to weighting the probability density function for t with the likelihood for different values of τ:

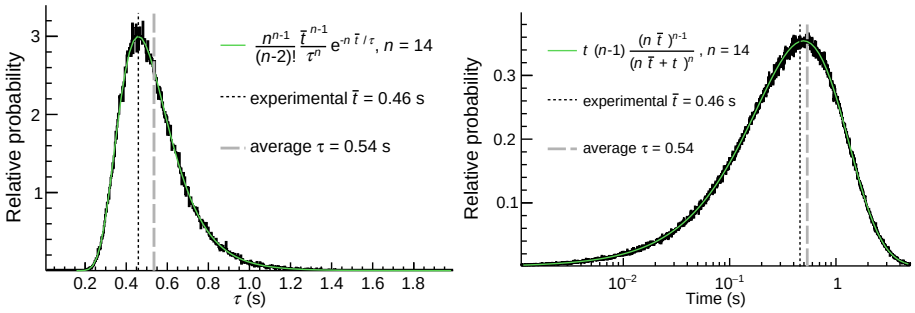

Figure 7.5: *(Left) Relative likelihood for different values of τ, in case fourteen measurements of the lifetime have been performed and the resulting average lifetime is 0.46 s. The histogram is based on 10^5 simulated sets of fourteen chains. The resulting average τ is 0.54 s. The green line is the corresponding analytical expression $p_{n,\bar{t},norm}(\tau)$. The vertical lines mark the average lifetime and the calculated average τ. (Right) Probability density function for times from an exponential function where the τ is determined as the average lifetime of n chains. The green line is $p_{n,\bar{t}}(t)$.*

$$p_{n,\bar{t}}(t) = \frac{\int_0^\infty p_\tau(t) p_{n,\bar{t},norm}(\tau) d\tau}{\int_0^\infty p_{n,\bar{t},norm}(\tau) d\tau} \tag{7.21}$$

The integral in the denominator is one. The integral in the numerator is solved by using the change of variables $\frac{n\bar{t}+t}{\tau} = y$ and a number of partial integrations, giving

$$p_{n,\bar{t}}(t) = t(n-1)\frac{(n\bar{t})^{n-1}}{(n\bar{t}+t)^n}. \tag{7.22}$$

Figure 7.5(b) shows this function, together with a Monte-Carlo based histogram of the corresponding situation.

Figure 7.6 shows the original FoM (non-smeared distribution), Eq. 7.5, on a log scale, while the other three curves are $p_{n,\bar{t}}(t)$, Eq. 7.22, for $n = 5, 10, 30$ reference chains. For a low number of reference chains

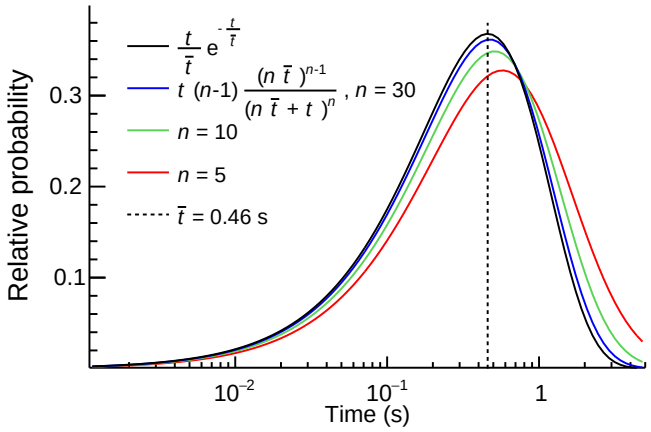

Figure 7.6: *Probability density functions for a plain exponential distribution characterised by a fixed τ (black) and for exponential distributions where the value of τ is associated with uncertainty originating from the determination of τ from 30, 10, and 5 data points, respectively.*

n, the distributions are rather broad, while they approach the original FoM "fixed-τ" distribution for larger values. Already at $n = 30$, the distributions agree almost completely, due to a strongly peaked τ likelihood function $p_{n,\bar{t},norm}(\tau)$, Eq. 7.20. The distributions are, for all n, wider than the "fixed-τ" distribution, but also shifted to the right. The maximum occurs at

$$t = \frac{\bar{t}}{1 - \frac{1}{n}} \tag{7.23}$$

which is always larger than $\bar{t}$, and approaches this value as the number of chains $n \to \infty$.

Equation 7.22, constructed for a reference data set, is a probability density function that can now be used as a smeared FoM, suitable for measuring the congruence between one lifetime t in a given data set and a reference distribution determined by the reference τ and the number of available reference lifetimes n. Figure 7.1 explains the notation.

A $\mathrm{FoM}_j^{(n)}$ is defined for each separate lifetime $t_j^{(n)}$ in the given data set, where $j = 1, \ldots, n_j$ is the step in chain n. More information can be obtained by considering all decay steps in a given chain. For this chain n the geometric mean of $\mathrm{FoM}_j^{(n)}$ over all available steps n_j defines $\mathrm{FoM}_{geom}^{(n)}$ for that chain. The arithmetic mean of $\mathrm{FoM}_{geom}^{(n)}$ over all M chains defines a new FoM valid for the entire data set, taking uncertainties in the reference data set and correlations within chains into account.

The reference data set can be the same as the one to examine. In this case the task of the test is to provide a measure of the internal congruence of the data set; each chain is evaluated with respect to the averages from the entire data set. If the individual chains all deviate strongly from the average data, the FoM value will be low. If the chains are all too similar to their average behaviour, the FoM will be high. Such test is similar to the one proposed by Schmidt in Ref. [106]. Note, however, that a low σ_θ corresponds to a large FoM and vice versa.

The reference data can also be an external set of chains. In this case the test gives an indication of how well the different data sets overlap. If the chains that are tested against an external reference have either much longer or much shorter half-lives compared to the reference, the FoM will be low.

To examine the devised FoM properly, large numbers of sets of chains were randomly generated. It is not obvious how to generate random sets of chains in a way that the essential features of the experimental data is kept. The question we want to answer is how the FoM behaves if the data set actually comes from an exponential distribution with a certain τ. When this is known, it is possible to check whether the experimental data differs from this behaviour or not. Each simulated set should originate from one exponential distribution – but should all simulated sets be simulated from the same exponential distribution? Should the sets be simulated using different values of τ, maybe according to the τ likelihood

function? Or should τ be allowed to vary freely, as long as the average time in each set is equal to the experimental average time?

To investigate different possibilities, random data sets were simulated in three different ways. To exemplify, the fourteen experimentally measured short chains are used. Ten of these comprise three lifetimes, and four comprise two lifetimes. In the first decay step there are $n_1 = 14$ lifetimes with an average lifetime $\bar{t}_{exp,1}$, in the second step $n_2 = 14$ with $\bar{t}_{exp,2}$, and in the third step $n_3 = 10$ with $\bar{t}_{exp,3}$. To simulate *one* set of chains using each of the three different methods, the following steps were taken:

1. Method 1, fixed τ

   - Fourteen lifetimes were generated from an exponential distribution characterised by $\tau = \bar{t}_{exp,1}$.
   - Fourteen lifetimes were generated from an exponential distribution characterised by $\tau = \bar{t}_{exp,2}$.
   - Ten lifetimes were generated from an exponential distribution characterised by $\tau = \bar{t}_{exp,3}$.

2. Method 2, values of τ randomly generated from likelihood function (Fig. 7.5)

   - A τ was selected from the distribution $\frac{n^{n-1}}{(n-2)!}\frac{\bar{t}^{n-1}}{\tau^n}e^{-n\bar{t}/\tau}$ with $n = 14$ and $\bar{t} = \bar{t}_{exp,1}$, and then fourteen lifetimes were generated by an exponential distribution characterised by the selected τ.
   - A τ was selected from the distribution $\frac{n^{n-1}}{(n-2)!}\frac{\bar{t}^{n-1}}{\tau^n}e^{-n\bar{t}/\tau}$ with $n = 14$ and $\bar{t} = \bar{t}_{exp,2}$, and then fourteen lifetimes were generated by an exponential distribution characterised by the selected τ.

- A τ was selected from the distribution $\frac{n^{n-1}}{(n-2)!}\frac{\bar{t}^{n-1}}{\tau^n}e^{-n\bar{t}/\tau}$ with $n = 10$ and $\bar{t} = \bar{t}_{exp,3}$, and then ten lifetimes were generated by an exponential distribution characterised by the selected τ.

3. Method 3, fixed $\bar{t}$ for each set

   - A τ is selected from a uniform distribution on the interval $[0{,}6{\cdot}\bar{t}_{exp,1}]$, and fourteen lifetimes are generated from an exponential distribution characterised by the selected τ. If the average value of the fourteen generated lifetimes is within the interval $\bar{t}_{exp,1} \cdot [0.99, 1.01]$, the generated lifetimes are kept.
   - A τ is selected from a uniform distribution on the interval $[0{,}6{\cdot}\bar{t}_{exp,2}]$, and fourteen lifetimes are generated from an exponential distribution characterised by the selected τ. If the average value of the fourteen generated lifetimes is within the interval $\bar{t}_{exp,2} \cdot [0.99, 1.01]$, the generated lifetimes are kept.
   - A τ is selected from a uniform distribution on the interval $[0{,}6{\cdot}\bar{t}_{exp,3}]$, and ten lifetimes are generated from an exponential distribution characterised by the selected τ. If the average value of the ten generated lifetimes is within the interval $\bar{t}_{exp,3} \cdot [0.99, 1.01]$, the generated lifetimes are kept.

Following each of the three methods, 10^5 sets of chains were generated. Then, the FoM for each generated data set was calculated using the reference probability density function given by the experimental chains. This means that the parameters in Eq. 7.22 are fixed to the values $n_1 = 14$, $n_2 = 14$, and $n_3 = 10$, and the respective average lifetimes $\bar{t}_{exp,1} = 0.459$ s, $\bar{t}_{exp,2} = 2.43$ s and $\bar{t}_{exp,3} = 9.85$ s.
The resulting FoM are distributed rather similarly. The resulting distribution of FoM from the second method is shown in Fig. 7.7. The distributions from the other two methods are slightly shifted to the right.

Table 7.2: *Simulated average FoM together with lower (↓) and upper (↑) limits for 90% and 98% confidence intervals, when different methods to generate sets of random chains are used. The case with fourteen chain, of which ten have three associated lifetimes and four have only two, is considered. The upper part of the table refers to simulations of a smeared FoM according to Eq. 7.22, and the lower part refers to simulations of a non-smeared FoM, i.e. a plain exponential function (Eq. 7.5). The experimental FoM values for the fourteen chains are 0.162 (smeared) and 0.171 (non-smeared), respectively. The combination in the fifth row (in italics) is deemed inappropriate (see main text).*

Method	1% ↓	5% ↓	Average	5% ↑	1% ↑
1	0.172	0.187	0.223	0.259	0.272
2	0.164	0.181	0.218	0.255	0.269
3	0.179	0.194	0.230	0.265	0.277
1	0.174	0.190	0.227	0.265	0.280
2	*0.158*	*0.177*	*0.219*	*0.259*	*0.274*
3	0.180	0.196	0.234	0.272	0.285

Obviously, sets of chains that do originate from exponential distributions can have very different FoM values. To characterise this, 90% and 98% confidence intervals were constructed. Intervals were chosen such that the probability for a value to appear within the respective interval is 90% (98%) with 5% (1%) probability of being outside the interval on either side. The limits for the intervals are presented in the upper part of Table 7.2, together with the average FoM values, for random chains generated using each of the three methods 1, 2, and 3.

There are two more aspects of the FoM method that are of importance. First of all, the selection of $\bar{t}$ in the FoM function Eq. 7.22 will be discussed. When calculating FoM for an experimental data set it seems natural to use the value $\bar{t} = \bar{t}_{exp}$, but how should it be selected when random chains are considered? Should they be compared with the same interval as the experimental data set, or should each set be compared with the average lifetime for the simulated set itself? Though not obvi-

ous, the effect of this decision is visible in the upper part of Table 7.2. For the chains generated according to method 3, where the average lifetime in each decay step is enforced to coincide with the experimental average lifetimes, the result is the same regardless of how the $\bar{t}$ in Eq. 7.22 is selected. Actually, the resulting FoM distributions are the same for all generation methods if the value of $\bar{t}$ for each simulated set is selected, and therefore they are the same as the results from method 3.

After this investigation, it is still not obvious which method should be used for random chain generation, and whether the average time should be re-calculated for each set or not. In Paper V [66], it was decided to use method 2 for chain generation and to use $\bar{t}$ in Eq. 7.22. As can be seen in Table 7.2, the resulting confidence interval is the most "generous" in the sense that the FoM for the experimental short chains, 0.162, is closer to fit within this interval than any of the other.

The second aspect which can be addressed is the question of whether it makes any difference if the smeared exponential distribution is used or if a plain exponential distribution is used. To test this, simulated intervals are tabulated in the lower part of Table 7.2 for which FoM calculations are instead made from a plain exponential function (Eq. 7.5). The confidence interval limits are slightly changed. The experimental FoM is 0.171. For method 2, the confidence intervals are broadened such that the experimental FoM is within the 98% confidence interval (but not the 90% interval). However, the combination presented in this row – a data set in which uncertainties in τ are taken into account, evaluated against a probability function where the uncertainties are ignored – is inadequate and thus disregarded. For the other two methods, the intervals are changed only slightly. This means that in the case of fourteen chains, the smearing does not make any practical difference. However, it is certainly more correct to take the uncertainties in τ into account when the probability density function is constructed.

Table 7.3: *Same as in Table 7.2, but for only four chains, each of which have three associated lifetimes. For the four short chains from JINR the experimental FoM are 0.114 (smeared) and 0.107 (non-smeared).*

Method	1% ↓	5% ↓	Average	5% ↑	1% ↑
1	0.115	0.141	0.201	0.257	0.175
2	0.110	0.136	0.197	0.272	0.254
3	0.141	0.165	0.223	0.269	0.283
1	0.128	0.157	0.225	0.291	0.312
2	*0.054*	*0.092*	*0.186*	*0.271*	*0.298*
3	0.150	0.181	0.250	0.314	0.333

For very small data sets, the smearing does make a difference. In Table 7.3, we repeat the same simulations as in Table 7.2, but when sets of only four chains are considered. The difference between the simulation methods, as well as the selected method for FoM calculation, is more pronounced in this case. While it is still difficult to decide on which method is the most appropriate, we further detail the smeared FoM based on a fixed value $\bar{t}$ using method 2.

Figures 7.7 and Fig. 7.8 show some aspects of the FoM measure. In Fig. 7.7 we show distributions for FoM, FoM_{geom} and FoM_1^1, generated to mimic the fourteen short chains. The FoM_1^1, which contain information about the lifetime in step 1 in chain 1, is strongly skewed. When the geometrical average FoM_{geom} over two and three decay steps are considered, the distribution becomes less skewed. When the arithmetical average over 14 chains is considered, the distribution becomes almost normal.

In Fig. 7.8 we investigate how the FoM curve changes shape when some members in the last step of the chains are missing. We consider fourteen chains, where the third decay step is missing in 0, 4, 8, and 14 chains. The last scenario corresponds to fourteen chains with two decay steps only. There is a gradual transition between the two extreme cases, reflecting the missing information.

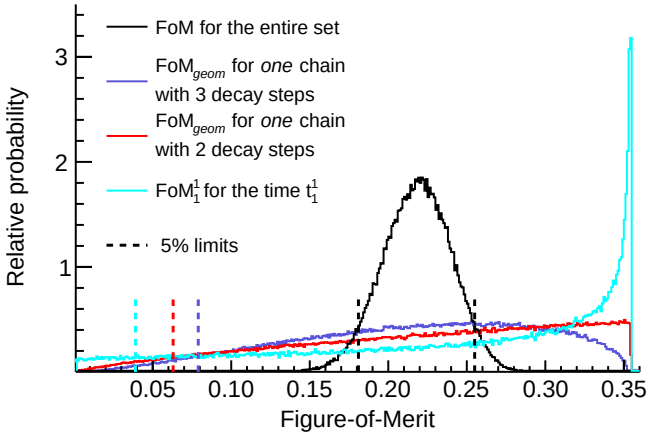

Figure 7.7: *Distributions for FoM, FoM_{geom} and FoM_1^1 (a single event) for data that has been generated to mimic the fourteen short chains.*

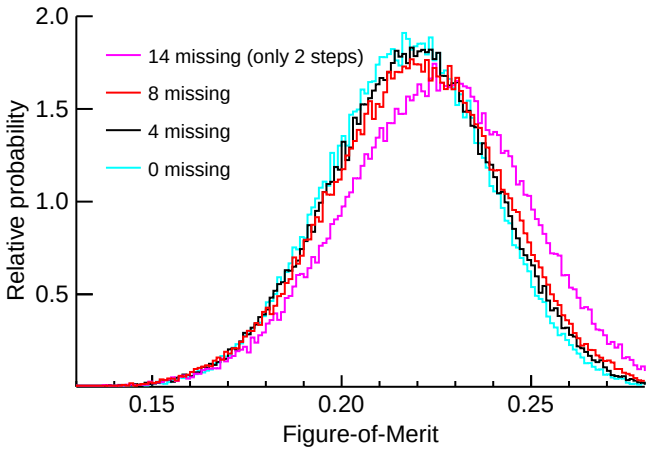

Figure 7.8: *Distributions of FoM for data that has been generated to mimic the fourteen short chains, but with 0, 4, 8 and 14 missing members in the last step. The last case is the same as if only two steps are considered. The distribution changes gradually as more members are missing.*

Finally, we investigate the sensitivity of the FoM test in two cases. As a starting point, we use 10^5 sets, generated according to method 2, of fourteen short chains. In the first case, we investigate the effect of having one odd chain, coming from another distribution than the other thirteen. In each of the 10^5 sets one chain with three members is replaced by a new chain generated according to method 1 (plain exponential distribution) with a $\tau_j = f \cdot \bar{t}_{exp,j}$ for $j = 1, 2, 3$. For selected values of f, the FoM distributions were calculated. The 90% FoM confidence interval for $f = 1$ was calculated. For $f \neq 1$, the probability for FoM to be outside this interval is calculated and tabulated in Table 7.4. Ideally, the probability to be outside the interval should be 100% when the chains do not have the same origin. When the odd chain has longer average lifetimes in all steps, it is considerably easier to tell that the data set is not congruent, than if the odd lifetime is associated with shorter average lifetimes.

In the second case, we investigate if the FoM measure can determine if two data sets are likely to have the same origin, or not. We start by evaluating the 90 % confidence interval for the fourteen short chains. Then, new sets of fourteen chains are generated using method 2 with scaled lifetimes $F \cdot \bar{t}_{exp,j}$ for each member j. The FoM distribution is calculated for selected values of F, and the probability for FoM to be outside the 90% confidence interval for $F = 1$ is tabulated in Table 7.4. For $F = 4$ *and* $F = 1/4$, the probability to be outside the interval is almost 100%. Thus, the FoM test can successfully distinguish the origin of two different data sets if they differ by a factor 4 in their average lifetimes.

The generalised FoM measure described in this section can be used to evaluate congruence within and between sets of chains. It takes into account the uncertainty in the reference data set. While details can be further discussed, the measure will be useful in many cases. It has been successfully applied to the short chains in Paper V [66].

Table 7.4: *Sensitivity of the FoM test. (Left) The factor f relates to the average lifetimes used when generating the odd chain, compared with the average lifetimes for the other chains. The second column shows the probability that the FoM is outside the 90% confidence interval for sets of chains where $f = 1$. The probability to find an FoM outside the confidence interval for $f = 1$ is 9% (not 10%, since the FoM bin size was 0.01). (Right) Fourteen chains generated according to method 2 with modified average lifetimes $F \cdot \bar{t}_{exp,j}$. The second column shows the probability that the FoM is outside the 90% confidence interval for sets of chains where $F = 1$.*

f	%
1/100	13.5
1/50	13.1
1/10	10.9
1/5	9.67
1	8.72
5	19.8
10	44.9
50	95.4
100	99.1

F	%
1/4	97
1/3	82
1/2	35
1	9
2	42
3	87
4	98

8

Results

Our element 115 experiment led to the observation of thirty correlated α decay chains. Twenty-three of the individual chains are presented in Table 1 in the supplemental material of Paper II [55] and constitute our "long" chains. The other seven "short" chains are presented in Table 1 in Paper V [66]. The long chains have decay characteristics that are to a large extent consistent with the previously [49] and subsequently [31] published long chains assigned to $^{287,288}115$. The short chains have characteristics that do not agree equally well with all four of the previously published short chains [49], but agree rather well with the three subsequently published chains [31]. This discrepancy is discussed in Paper V, where two different interpretations of the isotopic origin of these chains are presented.

In Figs. 8.1 and 8.2 average decay characteristics of the TASISpec chains are shown. Figure 8.1 corresponds to scenario 1 in Paper V. Here, the single long chain with overall shorter half-lives and higher α energies is attributed to $^{287}115$, i.e. the $4n$ production channel. The other long chains are assigned to $^{288}115$ ($3n$). All short chains are assigned to $^{289}115$ ($2n$). For $^{287}115$ the given times are the half-lives, $T_{1/2}$, for the single chain, and for $^{288,289}115$ the half-lives are obtained by averaging

all available data points from our experiment in the respective decay step. The energy intervals cover the respective region where almost all α energies in the given decay step were found. The intervals only give a first simplified picture of the α energies – for details, the tables or histograms in the articles should be consulted. In parentheses, energies where several α particles were detected are highlighted. Figure 8.2 follows the same notation but corresponds to scenario 2 in Paper V. Here, all our short chains are attributed to $^{288}115$, and none to $^{289}115$. The half-lives are slightly modified by the addition of the short chains to $^{288}115$. Fission branches of 7% and 19% have been added to $^{284}113$ and ^{280}Rg, respectively. In reality, some of the short chains could be from $^{288}115$ and some from $^{289}115$. However, it is difficult to make an assignment on a chain-by-chain basis.

Let us return to Fig. 3.1, which shows all – not only TASISpec – data on element 115 according to the interpretation that all short directly produced element 115 chains are from $^{289}115$ (our scenario 1) and that all "short" element 117 chains are from $^{293}117$. Considering TASISpec data only, the half-lives for the first three steps are $0.3(^{2}_{1})$ s, $0.6(^{3}_{2})$ s, and $4(^{3}_{1})$ s, respectively. The respective half-life data from the JINR on sixteen chains assigned to $^{293}117$ are $0.3(^{1}_{1})$ s, $3(^{1}_{1})$ s, and $18(^{7}_{4})$ s, respectively (compiled from Refs. [46, 53, 54]). The decay times in the second and third step are not necessarily consistent. If our scenario 2 – in which all observed short element 115 chains come from $^{288}115$ – would be the correct interpretation, Fig. 3.1 changes considerably. As there would be no directly observed $^{289}115$, the link to the element 117 data would be absent. In reality the picture is complicated by the fact that one of the short element 115 decay chains from JINR seems to be different from all other short chains, and that it is likely that neither scenario 1 nor scenario 2 contain the full truth. Still, the link between element 115 and element 117 decay chains is not as obvious as was first thought [49, 50, 51, 52, 53, 54].

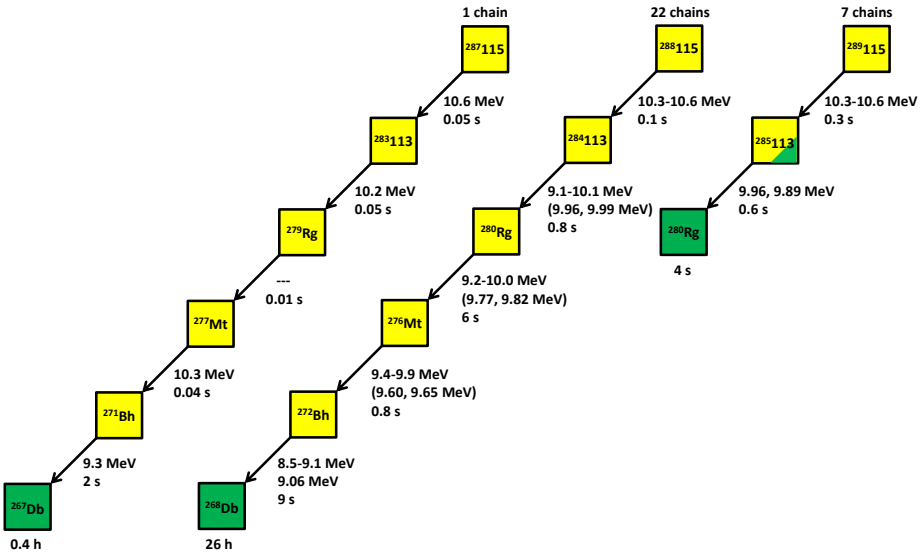

Figure 8.1: *The thirty decay chains measured by TASISpec interpreted according to scenario 1. Times relate to half-lives, energy intervals to regions that cover most of the observed data, and energies in parentheses to peaks in the energy spectra.*

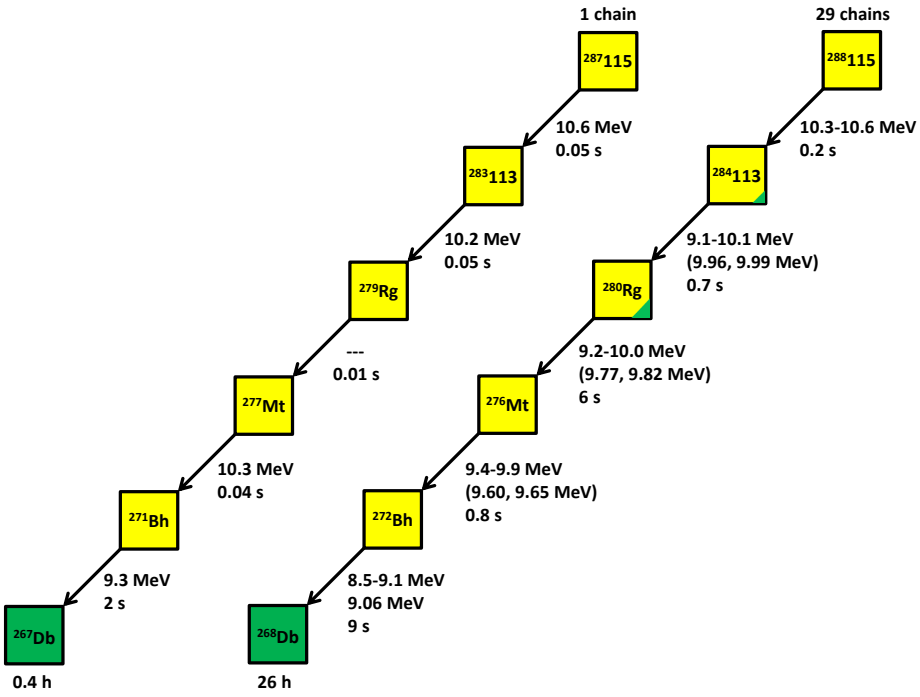

Figure 8.2: *The thirty decay chains measured by TASISpec interpreted according to scenario 2. Times relate to half-lives, energy intervals to regions that cover most of the observed data, and energies in parentheses to peaks in the energy spectra.*

Regarding the fission branches added to the decays of element 113 and Rg, one important note must be made. None of the detector setups used for studies for element 115 decay chains have been sensitive to electron capture (EC) decay, since the setup would have to be sensitive to radiation from atomic processes. The observed fissions can as well be attributed to EC decays followed by very fast spontaneous fission from the resulting even-even nucleus. Actually, EC decay is expected in this region of the nuclear chart [107]. The finite probabilities for EC in these nuclei open up an entirely new question regarding decay chains from superheavy elements: Maybe the observed decay chains consist of both α decays and (undetectable) EC decays. This would make it impossible to relate the members in the chains to each other in terms of proton numbers. However, decay characteristics from surrounding nuclei, the fact that α decays from even-even nuclei – in contrast to odd-even or odd-odd nuclei – tend to have well-defined energies as they often proceed from ground state to ground state, and the larger probabilities for spontaneous fission in the even-even nuclei, reinforces the interpretation that the element 115 decay chains consist of α decays with no intermediate EC decays.

The cross sections for production of the different isotopes of element 115 measured with TASISpec are shown in Fig. 8.3, for scenario 1 (a,c) and scenario 2 (b,d). The top figures (a,b) show only the TASISpec data points and theoretical curves from Refs. [16, 18]. In scenario 1, where all short chains are assigned to the $2n$ channel, the ratio between the maximal cross sections for the $2n$ and $3n$ channels seems unexpectedly large compared with both theoretical models shown in the figure. On the other hand, assigning all short chains to the $3n$ production channel in scenario 2, this ratio is lower than expected. The low number of events observed in our measurement, together with the overlapping energy intervals resulting from the thick targets, makes the interpretation

of our suggested excitation functions difficult. In Fig. 8.3(c,d) also the data points from measurements at JINR are shown for comparison. Either interpretation of the TASISpec data is in agreement with data and interpretations from JINR.

Energy spectra from the silicon detectors have been constructed for those events that are part of a decay chain. The expected energy from the recoiling daughter nucleus has been subtracted. The spectra are shown in Figs. 8.4(c,e,g,i,k). Figures 8.4(d,f,h,j,l) show energy depositions in the germanium detectors. Only events in prompt coincidence with decays that are part of the correlated chains are shown. In Fig. 8.4(a), the correlation time between germanium and silicon signals as a function of the germanium detector energy is shown. The data is from beam-off periods. The white line defines the selection for prompt coincidences. Figure 8.4(b) shows the total germanium energy spectrum in prompt coincidence with any event in the silicon detector, beam-off. The peak at 511 keV is primarily due to e^+e^- annihilation following β^+ decays of implanted unwanted nuclei.

There are only very few events in the germanium detectors; from $^{288}115$ and $^{284}113$ there is only one observed photon each, and in ^{268}Db there is none. A measured photon could be an X ray or a γ ray resulting from de-excitation of an excited nuclear state. The probability that it is randomly correlated to the observed decay in the silicon detector is small [59]. Additionally, there is a probability that Compton scattering occurred in the detector and that not all the energy was deposited. However, simulations using `Geant4` [58] have shown that the probability for measuring two photons within the same 1 keV bin is virtually zero unless there is a transition in the level scheme with that energy. This means that two photons in the same energy channel are likely to constitute a peak.

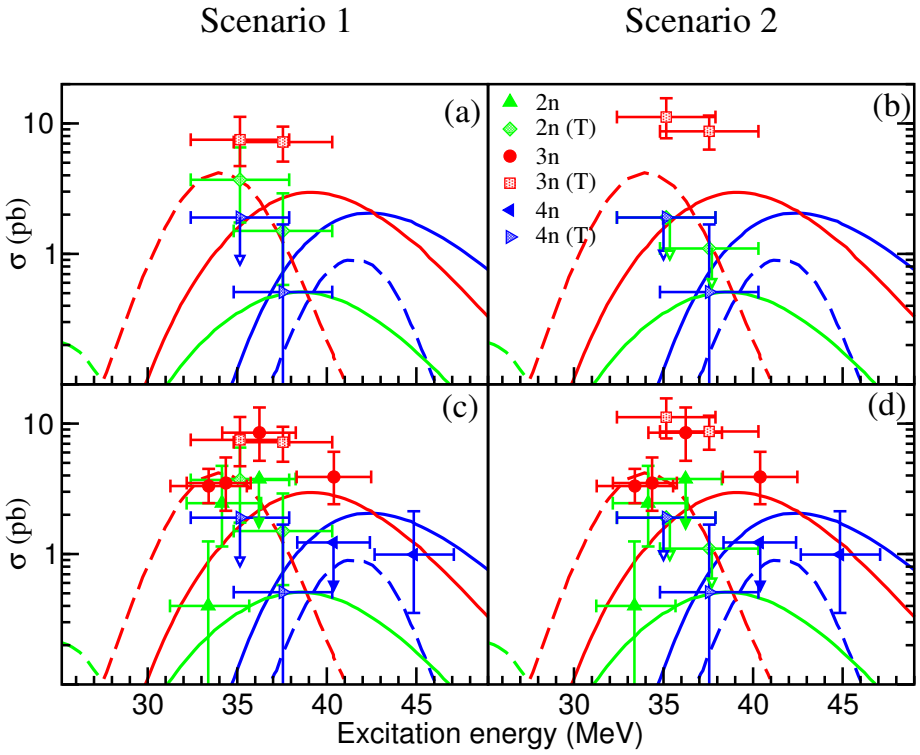

Figure 8.3: *Cross sections for production of element 115 isotopes. The data points labelled with (T) are from TASISpec. The other data points and curves are digitised from Fig. 4 in Ref. [23]. The data points relate to the collected element 115 data from JINR, and the theoretical curves are, according to the caption in Fig. 4 in Ref. [23], from calculations by V. Zagrebaev (solid) [16] and by K. Siwek-Wilczyńska [18] (dashed). (a,b) Data points from the TASISpec measurement only. (c,d) Data points from the TASISpec measurement and data points from JINR. The mass table used to transform between beam energies and excitation energies for TASISpec measurements is from Ref. [99]. (a,c) TASISpec data interpreted according to scenario 1. (b,d) TASISpec data interpreted according to scenario 2.*

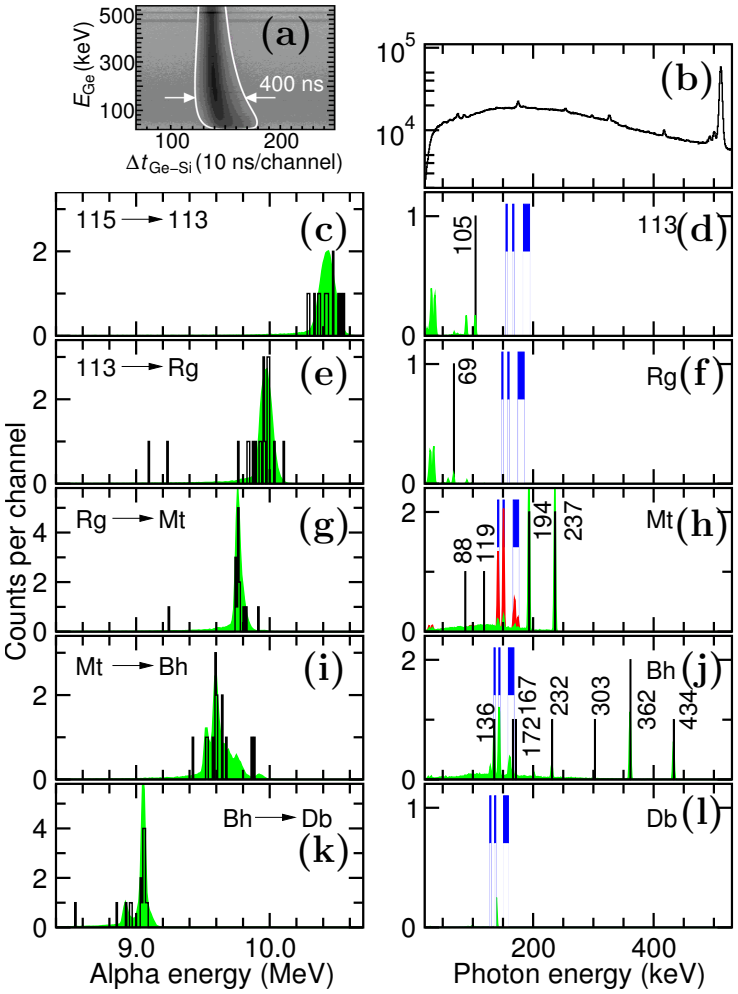

Figure 8.4: *Data from our element 115 experiment. (a) Time correlations between silicon and germanium data as function of germanium energy. (b) Number of photons in coincidence with any particle in the silicon detectors. (c,e,g,i,k) Measured α energies for decay chain members (black) and simulated energy spectra (green). (d,f,h,j,l) Energy spectra for photons observed in prompt coincidence with a decay chain member (black) and simulated spectra (green and red). The blue bars indicate the expected position of $K_{\alpha I,II}$-X rays and K_{β}-X rays. See text for more details. Figure from Ref. [55] (reprinted with permission).*

A few initial conclusions can be drawn. For $^{288}115$ and $^{284}113$, the energy spreads of the α particles and the almost complete lack of photons calls for interpretations where the α decays proceed to excited states which then decay by highly converted transitions, which however do not have energies large enough for K conversion. The partial summing of α particles and conversion and Auger electrons would explain the observed broad spectrum. In ^{276}Mt and ^{272}Bh we observed six and eight photons, respectively. In ^{276}Mt the narrow α-decay peak points to a level scheme where the α decay preferably proceeds to one excited state, while the structure in the ^{272}Bh spectrum suggests a more complex α-decay scheme. In the ^{268}Db silicon spectrum, there are seemingly two α decay energies.

To investigate the decay data in more detail, `Geant4` simulations were performed Ref. [55, 58, 59, 60, 61, 62]. The nuclear energy level schemes that are used as input in the simulations were varied until best possible self-consistency was achieved. The best agreement for the 22 TASISpec chains was achieved by using the level schemes presented in Fig. 8.5. Simulated spectra using 10^5 decays of $^{288}115$ and the obtained level schemes are shown in Fig. 8.4 (Paper II, [55]).

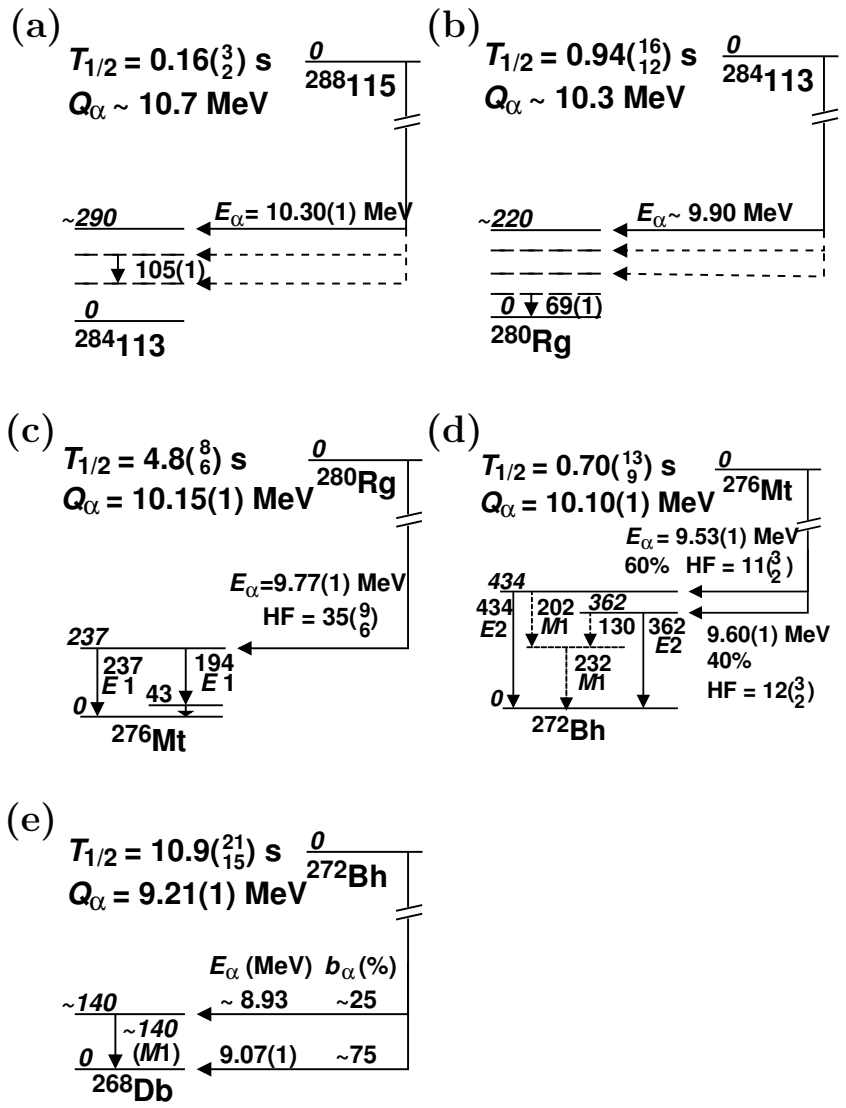

Figure 8.5: *Suggested nuclear energy level schemes based on the data from TASISpec for (a) $^{288}115$ (b) $^{284}113$ (c) ^{280}Rg (d) ^{276}Mt (e) ^{272}Bh. The half lives have been obtained using both TASISpec and JINR data. Figures (c,d) from Ref. [55] (reprinted with permission).*

The suggested level scheme for ^{272}Bh contains many interesting features. The α decays to two different excited states that can decay to the ground state via ∼400 keV E2 transitions open up for the possibility of also having ∼200 keV M1 transitions to and from intermediate excited states. The γ decays from these states would be highly K converted, and possibly explain the observation of the two potential X rays observed *in coincidence* in this decay step. The potential X rays had 136 keV (expected K_{α_2} from ^{272}Bh) and 167 keV (expected K_{β_2} from ^{272}Bh). An energy deposition of 303 keV, which could be due to summing of 136 keV and 167 keV, was also measured in this decay step. Yet another observation of a 136-keV photon occurred, but the α decay could not be securely positioned within the correlated α decay chains due to one missing α in that chain.

These first observations of potential X rays are very exciting, as they give the first indication on the proton numbers in superheavy elements. For a given photon, it is difficult to deduce if it originates from an atomic transition or from a γ transition with the same energy. Therefore, it is required to observe photons at the right X-ray energies *and* with the expected ratios for K_{α_1}, K_{α_2} and K_β transitions. The photon at 167 keV unfortunately seems to originate from a nuclear de-excitation. This has been concluded from the fact that several photons of this energy were measured during the element 115 spectroscopy experiment at Lawrence Berkeley National Laboratory (LBNL). Since K_β X rays are more rare than K_α X rays, many more X rays at 136 keV (K_{α_2}) and 144 keV (K_{α_1}) should have been observed. Therefore, a γ transition of 167 keV has been established, and any photon measured at this energy is likely to be of nuclear origin. However, the photon that we observed at 136 keV remains a valid X ray candidate. In addition to our X-ray candidates, *a pair* of photons at 136 keV and 144 keV were observed in coincidence and assigned to decays in ^{272}Bh in the experiment at LBNL [31].

The proposed level scheme for ^{276}Mt contains one very interesting feature. In our experiment, two photons at 237 keV and two photons at 194 keV were observed. Our only plausible explanation for the peaks is that they are γ transitions with E1 character. Transitions of these energies with any other multipolarity would be much more strongly converted, and we would rather expect to observe X rays or, simply, not so many γ rays. In Ref. [60], simulations assuming E1, M1 and E2 characters show that E1 provides the best match. The measurements at LBNL independently confirmed the E1 character of the 237 keV transition. As a side remark, a perfect X-ray fingerprinting case would have occurred if the E1 transition had instead been of M1 character. A simulated photon spectrum where M1 character is assumed is also shown in Fig. 8.4(h).

The discovery of the presence of at least one E1 transition in the odd-odd nucleus ^{276}Mt is very interesting from the perspective of nuclear structure. In α decays, it is common that an odd nucleon remains in its energy level and does not participate in the decay. In the subsequent γ decay, the odd nucleon moves from its previous single-particle orbital to a lower-lying orbital. Surprisingly, there are very few pairs of single-particle levels which can be connected by E1 transitions since they require a change in parity. Figure 8.6 shows the Nilsson diagrams for single-particle levels for neutrons and protons [108]. The anticipated deformation for the nuclei in the ^{288}115 decay chain evolves from slightly deformed for 115 to almost spherical for 113 and then more and more deformed along the chains. The deformation and the anticipated energy level occupied by the last unpaired nucleon in each nucleus is indicated in the figure.

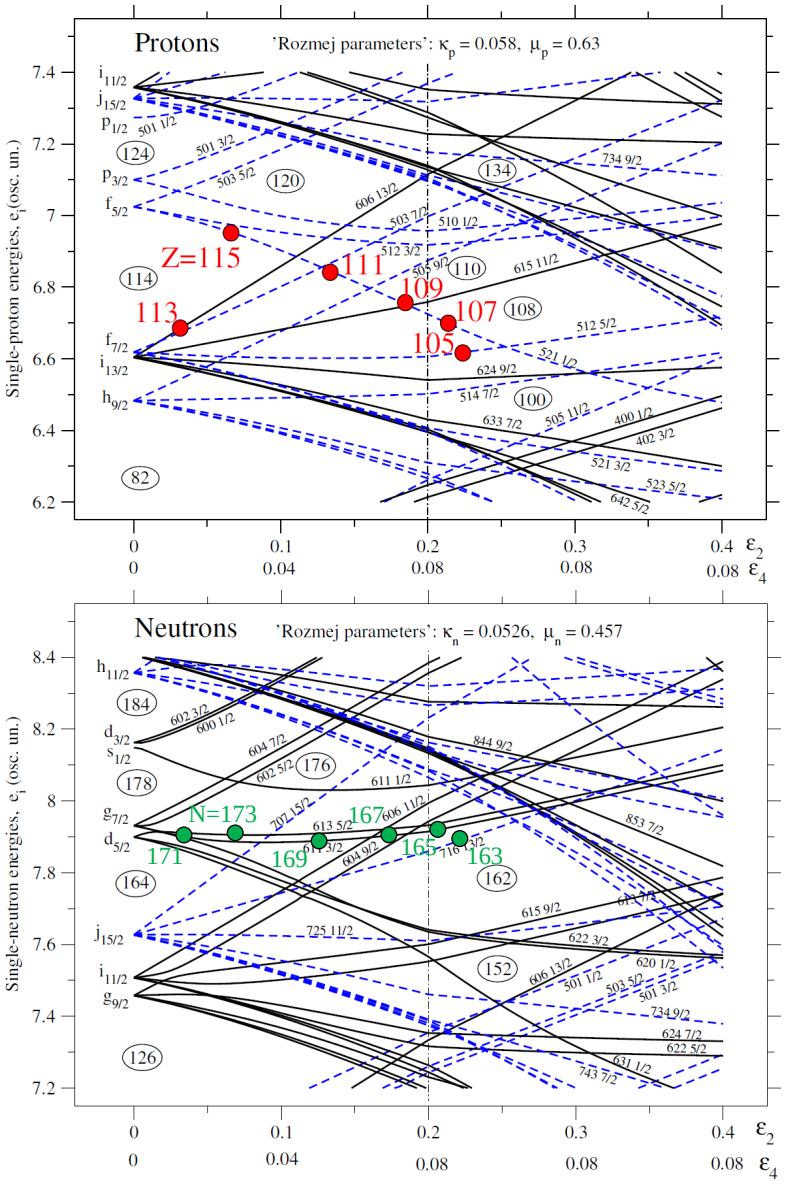

Figure 8.6: *Nilsson levels for protons (top) and neutrons (bottom). Solid (dashed) curves describe orbitals with positive (negative) parity. See text for more details. Figure from Ref. [108].*

In the proton Nilsson diagram the only positive-parity orbital in the region around the Fermi level at the deformations expected for the nucleus with 109 protons is the orbital [615]11/2. There are plenty of negative-parity orbitals, but it is only the orbital [505]9/2 that can connect the [615]11/2 orbital via an E1 transition. This indicates that if the odd proton is responsible for the E1 transition, it must change from one of these two orbitals to the other. On the neutron side, there is also only one such pair: The negative parity orbital [716]13/2 and the positive-parity orbital [606]11/2. Hence, there are only two explanations for the presence of an E1 transition, and this provides strong restrictions for nuclear structure theories. In a more elaborate model, the coupling between the odd proton, the odd neutron, and the collective rotation should also be considered. Detailed theoretical nuclear structure models have addressed the E1 transition in Ref. [109].

In the level schemes in Fig. 8.5 the respective α decay hindrance factors are given for some of the α decays. The hindrance factors have been estimated [110] by comparing the experimental half lives to the half lives from the model in Ref. [111]. A small hindrance factor indicates that there are no large differences between the initial and final nuclear structure. The hindrance factor for the 9.77-MeV α decay from ^{280}Rg to ^{276}Mt is about 35, and the ones for the 9.53-MeV and 9.60-MeV α decays from ^{276}Mt to ^{272}Bh are around ten. A comprehensive compilation of experimental α-decay data of near-spherical odd-A nuclei has been made in Ref. [112]. Here, it is found that hindrance factors for transitions in which the odd nucleon remains in the same orbital before and after the α decay tend to be very low, $\sim$1-5, while transitions in which an orbital change takes place but parity and spin projection is unchanged tend to be 10-100. Decays where larger structural changes are needed tend to have hindrance factors above 100. Hence, the hindrance factors can give some insight into the nuclear structure. In Ref. [62] the world data set

on elements 115 decay chains has been used to detail the level schemes further, with corresponding hindrance factors.

The Q-values that are assumed in the various level schemes are also indicated in Fig. 8.5. To carefully derive the Q-values, detailed simulations of various possible decay schemes have been made in Ref. [61], where data from TASISpec *and* JINR are considered. The resulting Q-values are shown in Fig. 8.7. For the decays from $^{288}115$ and $^{284}113$ the uncertainties are larger due to the wide α decay distributions that open up for different interpretations containing either one or more α decays (see Ref. [61]). It should be noted that there is a possibility that the chains start from an isomeric state in $^{288}115$, and that also subsequent α decays occur from isomeric states. Presence of isomeric states might affect the values presented in Fig. 8.7.

Interestingly, none of the theoretical models presented in Fig. 8.7 fit with the experimental Q-values along the entire $^{288}115$ decay chain. The Q-values in this region are sensitive to the anticipated shell gap around element 114, and our experimental data can be used to shed light on this exciting topic.

There are some remaining aspects of the element 115 experiment analysis that have not yet been made. We plan to investigate the long element 115 chains using statistical methods to resolve a few ambiguities regarding missing members in the α decay chains, provide more plots and compilations that are needed to fully describe the experiment and our data such that it can easily be compared with other experiments, and to further study the decay chain characteristics in comparison with existing theoretical models. We plan to refine all level schemes along the $^{288}115$ chains using the world data set, as was done for some of the decay steps [62]. These are the topics of a forthcoming publication.

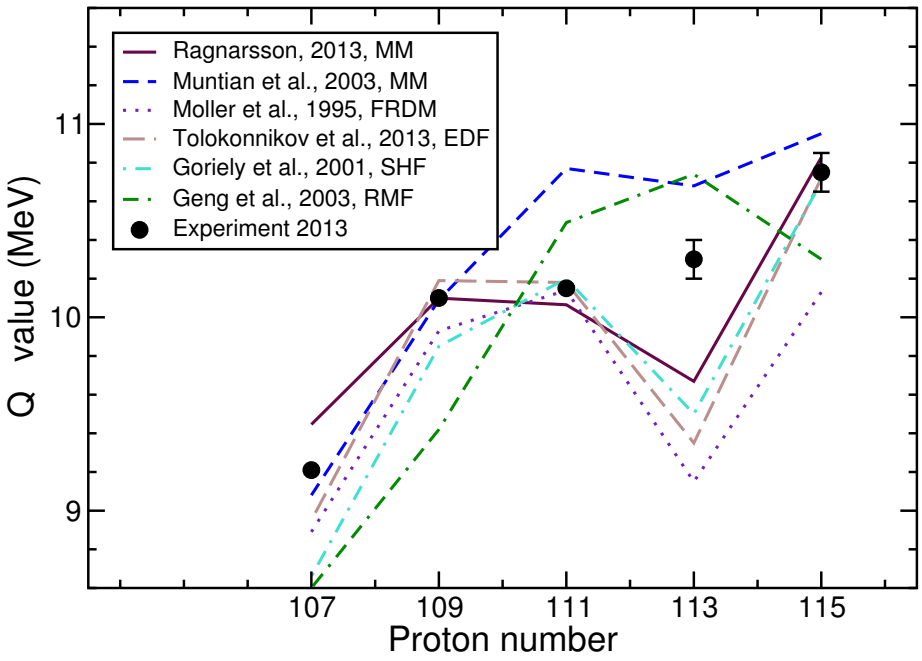

Figure 8.7: *Measured Q-values along* $^{288}115$ *decay chains (black dots) compared with predictions from various nuclear structure models. Figure from Ref. [61] (reprinted with permission).*

9

Conclusions

In this work, γ rays and potential X rays from superheavy element decay chains starting from $^{288}115$ have been observed. Together with the high-resolution α-decay data, the first nuclear energy level schemes for the isotopes along the chain have been suggested. The potential X rays give the first indication on the proton number in superheavy elements expected to have proton numbers $Z > 113$, although not sufficiently many were provided by Nature to allow for an unambiguous determination. The level schemes give the first insights into the nuclear structure of these elements. Of particular interest is the observation of the E1 transition in ^{276}Mt. The existence of such a transition constitutes one of the first stringent tests of nuclear structure theories in this part of the chart of nuclides. Any proposed model must explain its presence and its position in decay chains of $^{288}115$.

One important conclusion is that it is indeed technically – and within acceptable beam-time periods – feasible to measure the proton number in superheavy elements with $Z > 113$ by X-ray fingerprinting. The high efficiency of the experimental setup, the high transmission through TASCA, the low background that allows for establishment of true correlations in the data, the use of digital electronics, and the detailed `Geant4`

cross-checks etc. made the experiment very successful.

Overall, our experiment confirmed the previously measured decay characteristics of the long element 115 decay chains. For the short chains, the situation is different. Our observations of both implantation-α-α-fission and implantation-α-fission chains show the existence of a previously unknown branch of spontaneous fission (or EC) in either ^{284}113 or ^{285}113. Our statistical assessments of the congruence within the world data set of fourteen short chains show with <1% error probability that these chains do not all have the same origin. Under the assumption that all short chains stem from the $2n$ evaporation channel product ^{289}115, a likely interpretation is that one short chain from JINR, which has deviating decay characteristics, forms a distinct separate decay sequence. This re-interpretation has implications for the connection between the element 115 and element 117 decay chains. Our conclusion is that such a connection might well exist, but not in the form that the IUPAC/IUPAP Joint Working Party built their approval on for elements 115 and 117 [9].

10

Outlook

It is likely that all elements up to $Z = 118$ have indeed been created and observed, and that all experimental data are correct. However, it is easy to get carried away by the excitement around the discovery of new elements. The sound scepticism that is one of the main pillars of science should not be overlooked. Even after our element 115 experiment and the similar experiment performed at LBNL, proton numbers in superheavy elements with $Z > 113$ have not been firmly established.

Our experiment proves that it is indeed possible to perform X-ray fingerprinting on these elements, but we need to aim for another starting isotope than $^{288}115$. One suggestion, which we have already proposed to the GSI Program Advisory Committee, aims at searching for α-X-ray coincidences in the odd-even isotope ^{289}Fl ($Z = 114$). Further into the future we foresee investigations along element 117 odd-odd and odd-even decay chains. The equipment and techniques needed for proton number measurements of superheavy elements are in place, and any delays in answering the question of their identity stems from prioritisations at the accelerator laboratories involved.

Personally, I am surprised that the IUPAC/IUPAP Joint Working Party approved the odd-Z elements 113, 115 and 117 [9] with-

out any supporting X-ray spectrum. I am also surprised that elements 115 and 117 were approved solely on the claimed cross bombardments [49, 50, 51, 52, 53, 54] conducted at JINR, with the isotope $^{289}115$ constituting the link. In the IUPAC report [9] only the four short chains from measurements at JINR, postulated to originate from $^{289}115$, were considered. One of them is the chain that we show is highly unlikely to have the same origin as the other thirteen short chains from the world data set. A thorough investigation of the interpretations of the currently published element 117 chains and their connection to the observed element 115 chains is one of our next quests. Most likely, further experiments are needed to verify *any* interpretation.

The level schemes that have been suggested based on careful comparisons between experimental data and `Geant4` simulations have, for the first time, revealed some of the low-energy nuclear structure of the heaviest nuclei created on Earth. To explain the observations, nuclear structure theory at one of its extremes has to be applied. Theoretical nuclear structure calculations aiming at describing our data in general and the E1 transition in particular have been made in Ref. [109]. This assessment calls for further experiments where E1 transitions in neighbouring nuclei are searched for. Hindrance factors of odd-A near-spherical nuclei have been investigated using microscopic calculations in Ref. [112]. The interplay between detailed theoretical studies, such as in Refs. [109, 112], and further spectroscopy experiments in the region of superheavy elements is of major importance for understanding nuclei in general.

The experimental setup used for our element 115 investigation proved very successful. Yet, improvements can be made. In future experiments, we aim to use exclusively digital electronics for the read-out of all TASISpec silicon detector channels. During spring 2015, a fully digitised read-out using twelve FEBEX modules [92] was used during an experiment on proton emission from ^{53}Co at the JYFL Accelerator Laboratory in

Jyväskylä. This experiment also illustrates the versatility of TASISpec.

A completely new version of TASISpec dubbed "Lundium" is also under way thanks to a generous grant from the Knut and Alice Wallenberg Foundation. The main upgrade concerns novel encapsulated germanium detectors that can be positioned directly behind the silicon detectors inside TASCA without any additional surrounding cryostat end cap. The reduction of material will increase the efficiency for low-energy photons (∼30 keV) substantially and increase the probability for coincident observation of K-X rays and subsequent L-X rays. Other changes include re-configuring of the TASCA focal plane chamber such that the TASISpec implantation detector can be positioned in the focal plane. This would enable positioning of additional passive shielding of the germanium detectors as well as active Compton suppression shields.

One issue which remains even in the foreseen upgraded detector setup is the detection of electron capture decays, which emit radiation from atomic processes, i.e. X rays and Auger electrons. These can, in principle, be detected in TASISpec, but high background rates make it difficult to trigger the read-out system on X-ray detection in the germanium detectors, and typical noise levels prevent triggering on Auger electrons detected in the silicon detectors. If the electron capture occurs within a short time before or after a charged-particle decay that triggers the system, the detection of Auger and X rays could be detected in digitised traces, if these cover sufficiently long times before and after the trigger.

On the accelerator side, a new superconducting continuous-wave LINAC is currently under development at GSI [113, 114]. This accelerator will be primarily dedicated to the study of superheavy elements. The maximum possible beam current is expected to be at least one order of magnitude larger than what UNILAC can deliver. The accelerator is scheduled to deliver beams shortly after 2020.

Besides α-photon spectroscopy using the detector setup Lundium, the new accelerator will also power chemistry experiments, atomic spectroscopy experiments, and the hunt for even heavier elements. Continuing on the current path with actinide targets and beams heavier than ^{48}Ca, the cross sections are expected to decrease. However, several new elements could be discovered during the next decade using upgraded versions of the experimental setups and techniques of today.

New elements have a certain charm, but also long-lived isotopes tickle the imagination of both scientists and non-scientists. However, there are currently no viable options for producing superheavy nuclei with more neutrons, which would bring us closer to the anticipated island of stability. Fusion-evaporation reactions leading to superheavy nuclei in the vicinity of the anticipated island of stability using beams of radioactive neutron-rich ions have been suggested, but require high beam intensities that are not currently foreseen [115]. As of now, it seems like the most promising way is to produce, e.g., element 122 that might decay via a series of electron capture decays into more neutron-rich element 114 nuclei. If Nature provides us with such an electron-capture path, we may reach the elusive island of stability within the next decade(s).

Appendix A

Reaction kinematics

The compound nucleus is created when the incoming ion (^{48}Ca in the present cases) impinges on a target atom. Since the projectile energy is very small compared to the masses of the particles, classical mechanics described the situation sufficiently well. Conservation of momentum leads to the equation

$$E_{kinetic,\,CN} = E_{kinetic,\,beam} \cdot \frac{m_{beam}}{m_{CN}}. \tag{A.1}$$

The excitation energy of the compound nucleus, E^*, is the sum of the kinetic energy of the incoming particle and the released binding energy, Q, (either positive or negative), minus the kinetic energy of the compound nucleus.

Using the previous results, the excitation energy is given as

$$\begin{aligned} E^* &= E_{kinetic,\,beam} - E_{kinetic,\,beam} \cdot \frac{m_{beam}}{m_{CN}} + Q = \\ &= E_{kinetic,\,beam}(1 - \frac{m_{beam}}{m_{CN}}) + Q. \end{aligned} \tag{A.2}$$

Q is calculated either using the masses of the involved nuclei, using

$$Q = (m_{initial} - m_{final})c^2 = (m_{beam} + m_{target} - m_{CN})c^2, \tag{A.3}$$

or using the mass excess ($ME_x = m_x c^2 - m_A c^2$), since many mass tables give this number instead of the mass itself:

$$\begin{aligned} Q &= (m_{beam} + m_{target} - m_{CN})c^2 = \\ &= ME_{beam} + M_{A,\,beam} + ME_{target} + M_{A,\,target} - (ME_{beam} + M_{A,CN}) = \\ &= ME_{beam} + ME_{target} - ME_{CN}. \end{aligned} \tag{A.4}$$

Appendix B

Optimal quadrupole currents for different $B\rho$

For TASCA in HTM and a pressure of 0.8 mbar He, the magnet settings $I_D = 603$ A, $I_{Q_1,opt} = 525$ A and $I_{Q_2,opt} = 510$ A proved most successful for focusing ^{254}No into TASISpec. This knowledge can be used for deriving the best settings also for particles with different magnetic rigidities.

The magnetic field in an electromagnet does not depend linearly on the current through the magnet. For the TASCA dipole, the relation between the $B\rho$ (given in Tm) and the current I_D (given in A) is [116]

$$B\rho = 2.1 \cdot 10^{-3} + 3.39 \cdot 10^{-3} \cdot I_D + 4.10687 \cdot 10^{-6} \cdot I_D^2 - 9.23116 \cdot 10^{-9} \cdot I_D^3 + 4.41778 \cdot 10^{-12} \cdot {I_D}^4. \quad \text{(B.1)}$$

For the TASCA quadrupoles, the current dependence is considered together with the presumed optimal relation between the quadrupoles and dipole. Therefore, different expressions are used for HTM and SIM. In HTM, the relation between the current in the quadrupoles and the

selected $B\rho$ is

$$I_{Q_{1,2},std} = 0.26348 + 158.93462 \cdot B\rho + 48.35024 \cdot (B\rho)^2. \tag{B.2}$$

In SIM, the currents in the two quadrupoles as functions of the selected $B\rho$ are

$$\begin{aligned} I_{Q_1,std} &= \left[-0.25644 + 46.51499 \cdot B\rho + 91.4858 \cdot (B\rho)^2\right] \cdot 0.99 \\ I_{Q_2,std} &= \left[-0.06942 + 109.05003 \cdot B\rho + 72.22877 \cdot (B\rho)^2\right] \cdot 1.03 \end{aligned} \tag{B.3}$$

The experimentally found optimal settings define a new focusing scheme. Therefore, the expressions for the quadrupoles have to be rescaled. For a selected dipole current I_D corresponding to the selected $B\rho$, the optimal quadrupole settings in HTM are

$$I_{Q_{1,2}}(I_D) = I_{Q_{1,2},opt}(603A)\frac{I_{Q_{1,2},std}(I_D)}{I_{Q_{1,2},std}(603A)}. \tag{B.4}$$

Appendix C

Transforming scaling factors to magnet settings

The available TASCA field maps are constructed for the currents $I_D =$ 700 A, $I_{Q_1} = 585$ A, and $I_{Q_2} = 585$ A for HTM and for the currents $I_D =$ 700 A, $I_{Q_1} = 560$ A, and $I_{Q_2} = 560$ A for SIM. According to Ref. [116], the scaling factors f_{Q_1} and f_{Q_2} for the TASCA quadrupoles used in the simulation code `TSIM` relate to $B\rho$ and currents in the quadrupole magnets $I_{Q_{1,2}}$, using Eqs. (B.1), (B.2), (B.3)

$$f_{Q_{1,2}} = \frac{I_{Q_{1,2},std}(700A)}{I_{Q_{1,2},map}} \cdot \frac{I_{Q_{1,2}}}{I_{Q_{1,2},std}(B\rho)} \tag{C.1}$$

where

- $I_{Q_{1,2},std}(700A)$ is the current in the respective quadrupole according to Eqs. (B.2), (B.3), for the dipole current that the field map was created for;
- $I_{Q_{1,2},map}$ are the quadrupole currents for which the field map was created (see Table C.1);
- $I_{Q_{1,2},std}(B\rho)$ is the current in the respective quadrupole according to Eqs. (B.2), (B.3) for $B\rho$.

Table C.1: *The first factor in Eq. C.1, which connects the quadrupole scaling factors with the currents through the magnets.*

Mode	Quadrupole	Factor $\left(\frac{I_{Q_{1,2},std}(700A)}{I_{Q_{1,2},map}}\right)$
HTM	Q_1 and Q_2	$\frac{615}{585} = 1.05$
SIM	Q_1	$\frac{576}{560} = 1.03$
SIM	Q_2	$\frac{644}{560} = 1.15$

The first factor in Eq. C.1, $\frac{I_{Q_{1,2},std}(700A)}{I_{Q_{1,2},map}}$, is, for each quadrupole and each mode, a fixed fraction as long as the same field map is used. The factors are given in Table C.1.

As an example, the current to be used in Q_1 to get optimal transmission to TASISpec in HTM is $I_{Q_1} = 525$ A when the current through the dipole was $I_D = 603$ A. By using Eq. B.1 and Eq. B.2, $I_{Q_1,std}(B\rho) = 547$ A. The scaling factor f_{Q_1} is calculated as

$$f_{Q_1} = \frac{I_{Q_1,std}(700A)}{I_{Q_1,map}} \cdot \frac{I_{Q_1}}{I_{Q_1,std}(B\rho)} = 1.05 \cdot \frac{525}{547} = 1.01 \qquad \text{(C.2)}$$

References

[1] **en.wikipedia.org/wiki/Bob_Lazar** (February 19, 2016).

[2] **callofduty.wikia.com/wiki/Element_115** (February 19 2016).

[3] Yu. Ts. Oganessian *et al.*, Phys. Rev. C **69**, 021601 (2004).

[4] William D. Nesse, *Introduction to Mineralogy*, Oxford University Press (2000).

[5] R.B. Firestone, *Table of Isotopes, Eighth Edition*, John Wiley & Sons, Inc. (1996).

[6] J. Lachner *et al.*, Phys. Rev. C **85**, 015801 (2012).

[7] S.G. Nilsson *et al.*, Nucl. Phys. A **131**, 1 (1969).

[8] R.C. Barber *et al.*, Pure Appl. Chem. **83**, 1485 (2011).

[9] P.J. Karol *et al.*, Pure Appl. Chem. **88**, 139 (2016).

[10] P.J. Karol *et al.*, Pure Appl. Chem. **88**, 155 (2016).

[11] S. G. Nilsson and I. Ragnarsson, *Shapes and Shells in Nuclear Structure*, Cambridge University Press (1995).

[12] **www.nndc.bnl.gov/chart/reColor.jsp?newColor=dm** (February 20, 2015).

[13] G. Korschinek *et al.*, Nucl. Phys. A **944**, 190 (2015).

[14] G.M. Ter-Akopian *et al.*, Nucl. Phys. A **944**, 177 (2015).

[15] K. S. Krane, *Introductory Nuclear Physics*, John Wiley & Sons, Inc. (1988).

[16] V. I. Zagrebaev, Nucl. Phys. A **734**, 164 (2004).

[17] V.I. Zagrebaev and W. Greiner, Nucl. Phys. A **944**, 257 (2015).

[18] K. Siwek-Wilczyńska *et al.*, Phys. Rev. C **86**, 014611 (2012).

[19] F. P. Hessberger, ChemPhysChem **14**, 483 (2013).

[20] Yu. Ts. Oganessian *et al.*, Nucl. Phys. A **239**, 157 (1975).

[21] G. Münzenberg and K. Morita, Nucl. Phys. A **944**, 3 (2015).

[22] K. Morita *et al.*, J. Phys. Soc. Jpn. **81**, 103201 (2012).

[23] Yu. Ts. Oganessian and V.K. Utyonkov, Nucl. Phys. A **944**, 62 (2015).

[24] V. Zagrebaev and W. Greiner, Phys. Rev. C **78**, 034610 (2008).

[25] G. Münzenberg *et al.*, Nucl. Instrum. Methods **161**, 65 (1979).

[26] Yu. Ts. Oganessian *et al.*, Phys. Rev. C **79**, 024608 (2009).

[27] A.V. Yeremin *et al.*, Phys. Part. Nucl. Lett. **12**, 35 (2015).

[28] M. Leino, Nucl. Instr. Methods B **203**, 129 (2003).

[29] K. Morita *et al.*, Eur. Phys J. A **21**, 257 (2004).

[30] D. Kaji *et al.*, Nucl. Instr. Methods **B317**, 311 (2013).

[31] J.M. Gates *et al.*, Phys Rev. C **92**, 021301(R) (2015).

[32] J. Sarén *et al.*, Nucl. Instrum. Methods A **654**, 508 (2011).

[33] R.-D. Herzberg *et al.*, Nature **442**, 896 (2006).

[34] J. Khuyagbaatar *et al.*, Phys. Rev. Lett. **112**, 172501 (2014).

[35] L.-L. Andersson *et al.*, Nucl. Instr. Methods A **622**, 164 (2010).

[36] K. Hauschild *et al.*, Nucl. Instr. Methods A **560**, 388 (2006).

[37] R. D. Page *et al.*, Nucl. Instr. Methods **B204**, 634 (2003).

[38] W. Reisdorf and M. Schädel, Z. Phys. A **343**, 47 (1992).

[39] A.H. Wapstra *et al.*, Pure & Appl. Chem. **63**, 879 (1991).

[40] C. E. Bemis *et al.*, Phys. Rev. Lett. **31**, 647 (1973).

[41] Yu. Ts. Oganessian *et al.*, Phys. Rev. C **72**, 034611 (2005).

[42] D. Schumann *et al.*, Radiochim. Acta **93**, 727 (2005).

[43] S.N. Dmitriev *et al.*, Mendeleev Commun. **15**, 1 (2005).

[44] M. Stoyer *et al.*, Nucl. Phys. A **787**, 388 (2007).

[45] Yu. Ts. Oganessian *et al.*, Phys. Rev. Lett. **104**, 142502 (2010).

[46] Yu. Ts. Oganessian *et al.*, Phys. Rev. C **83**, 054315 (2011).

[47] Yu. Ts. Oganessian *et al.*, EPJ Web of Conferences **17**, 02001 (2011).

[48] Yu. Ts. Oganessian *et al.*, Phys. Rev. Lett. **108**, 022502 (2012).

[49] Yu. Ts. Oganessian *et al.*, Phys. Rev. C **87**, 014302 (2013).

[50] Yu. Oganessian, JINR Internal Report **E7-2012-58** (May 2012).

[51] J.H. Hamilton, J. Phys.: Conf. Series **420**, 012011 (2013).

[52] J.H. Hamilton, J. Phys.: Conf. Series **403**, 012035 (2012).

[53] Yu. Ts. Oganessian *et al.*, Phys. Rev. Lett. **109**, 162501 (2012).

[54] Yu. Ts. Oganessian *et al.*, Phys. Rev. C **87**, 054621 (2013).

[55] D. Rudolph *et al.*, Phys. Rev. Lett. **111**, 112502 (2013).

[56] U. Forsberg *et al.*, Acta Phys. Pol. B **43**, 305 (2012).

[57] U. Forsberg *et al.*, EPJ Web of Conferences **66**, 02036 (2014).

[58] L.G. Sarmiento *et al.*, PoS (X LASNPA) 057 (2014).

[59] D. Rudolph *et al.*, Acta Phys. Pol. B **45**, 263 (2014).

[60] D. Rudolph, JPS Conf. Proc. **6**, 010026 (2015).

[61] D. Rudolph *et al.*, J. Radioanal. Nucl. Chem. **303**, 1185 (2015).

[62] D. Rudolph *et al.*, AIP Conf. Proc. **1681**, 030015 (2015).

[63] D. Rudolph *et al.*, EPJ Web of Conferences, in press.

[64] D. Rudolph *et al.*, GSI Scientific Report 2013 page 126 (2014).

[65] D. Rudolph *et al.*, GSI Scientific Report 2014 page 180 (2015).

[66] U. Forsberg *et al.*, Nucl. Phys. A, in press.

[67] Yu. Ts. Oganessian, J. Phys. **G34**, 165 (2007).

[68] Yu. Oganessian, J. Phys. Conf. Series **312**, 082003 (2011).

[69] Yu. Ts. Oganessian and V.K. Utyonkov, Rep. Prog. Phys. **78**, 036301 (2015).

[70] J. F. Ziegler *et al.*, Nucl. Instrum. Methods B **219**, 1027 (2004).

[71] S. Agostinelli *et al.*, Nucl. Instrum. Methods A **506**, 250 (2003).

[72] J. Allison *et al.*, IEEE Transactions on Nuclear Science **53**, 270 (2006).

[73] E. Jäger *et al.*, J. Radioanal. Nucl. Chem. **299**, 1073 (2014).

[74] B. Kindler *et al.*, Nucl. Instrum. Methods A **561**, 107 (2006).

[75] K. Eberhardt *et al.*, Nucl. Instrum. Methods A **590**, 134 (2008).

[76] J. Runke *et al.*, J. Radioanal. Nucl. Chem. **299**, 1081 (2014).

[77] M. Schädel GSI, private communication (February 2012).

[78] A. Semchenkov *et al.*, Nucl. Instr. Methods **B266**, 4153 (2008).

[79] M. Schädel *et al.*, GSI Annual Report 2005 **262** (2006).

[80] N. Bohr, Phys. Rev. **58**, 654 (1940).

[81] H.-D. Betz, Rev. Mod. Phys. **44**, 465 (1972).

[82] A. Ghiorso *et al.*, Nucl. Instrum. Methods A **269**, 192 (1988).

[83] Yu. Ts. Oganessian *et al.*, Phys. Rev. C **64**, 064309 (2001).

[84] J. Khuyagbaatar *et al.*, Nucl. Instrum. Methods **689**, 40 (2012).

[85] K. E. Gregorich *et al.*, Phys. Rev. C **72**, 014605 (2005).

[86] J. M. Gates *et al.*, Phys. Rev. C **83**, 054618 (2011).

[87] M. Schädel, The European Physical Journal D **45**, 67 (2007).

[88] J. Eberth *et al.*, Nucl. Instr. Methods A **369**, 135–140 (1995).

[89] G. Duchêne *et al.*, Nucl. Instr. Methods A **432**, 90 (1999).

[90] L. G. Sarmiento *et al.*, Nucl. Instr. Methods A **667**, 26 (2012).

[91] P. Golubev *et al.*, Nucl. Instrum. Methods A **723**, 55 (2013).

[92] J. Hoffmann *et al.*, GSI Scientific Report 2011 page 253 (2012).

[93] W. Loveland *et al.*, Phys. Rev. C **66**, 044617 (2002).

[94] K. E. Gregorich *et al.*, Eur. Phys. J. A **18**, 633 (2003).

[95] K. E. Gregorich *et al.*, GSI Scientific Report 2006 page 144 (2007).

[96] A. Belov *et al.*, GSI Scientific Report 2006 page 143 (2007).

[97] L.G. Sarmiento, private communication (March 2016).

[98] G. Audi *et al.*, Nucl. Phys. A **729**, 337 (2003).

[99] W. Myers and W. Swiatecki, Nucl. Phys. A **601**, 141 (1996).

[100] J. M. Gates *et al.*, GSI Scientific Report 2011 (2012).

[101] J. Adamczewski *et al.*, IEEE Trans. Nucl. Sci. **51**, 565 (2004).

[102] R. Brun and F. Rademakers, Proceedings AIHENP'96 Workshop, Lausanne, Sep. 1996, Nucl. Inst. & Meth. in Phys. Res. A **389** 81 (1997). See also http://root.cern.ch/.

[103] V. T. Jordanov and G. F. Knoll, Nucl. Instr. Methods A **345**, 337 (1994).

[104] U. Forsberg, *Pulse Shape Analysis for Heavy Element Spectroscopy*, Master's thesis Lund University (2010).

[105] K.-H. Schmidt *et al.*, Z. Phys. A **316**, 19 (1984).

[106] K.-H. Schmidt, Eur. Phys. J. A **8**, 141 (2000).

[107] A.V. Karpov *et al.*, Int. J. Mod. Phys. E **21**, 1250013 (2012).

[108] I. Ragnarsson, private communication.

[109] Y. Shi *et al.*, Phys. Rev. C **90**, 014308 (2014).

[110] D.E. Ward, private communication (2016).

[111] C. Qi *et al.*, Phys. Rev. C **80**, 044326 (2009).

[112] D.E. Ward, B.G. Carlsson, and S. Åberg, Phys. Rev. C **92**, 014314 (2015).

[113] W. Barth, S. Jacke, and S. Mickat, Proceedings of IPAC2012, New Orleans, Louisiana, USA, THPPP032 (2012).

[114] W. Barth *et al.*, Proceedings of IPAC2013, Shanghai, China, THPWO007 (2013).

[115] W. Loveland, Phys. Rev. C **76**, 014612 (2007).

[116] J. Khuyagbaatar GSI, private communication (2011).